Multiphysics Modelling of Energy Storage Devices Using Pore Scale Approaches

by

Zohaib Atiq Khan

A thesis

presented to the University of Waterloo

in fulfilment of the

thesis requirement for the degree of

Doctor of Philosophy

in

Chemical Engineering

Waterloo, Ontario, Canada, 2020

Examining Committee Membership

The following served on the Examining Committee Membership for this thesis. The decision of the Examining Committee is by majority vote.

External Examiner	Prof. Majid Bahrami School of Mechatronic Systems Engineering, Simon Fraser University
Internal-External Member	Prof. Eihab Abdel-Rahman Department of System Design Engineering, University of Waterloo
Internal Member	Prof. Marios Ioannidis Department of Chemical Engineering, University of Waterloo
Internal Member	Prof. Michael Pope Department of Chemical Engineering, University of Waterloo
Supervisor	Prof. Jeff T. Gostick Department of Chemical Engineering, University of Waterloo
Supervisor	Prof. Ali Elkamel Department of Chemical Engineering, University of Waterloo

Author's Declaration

This thesis consists of material all of which I authored or co-authored: see Statement of Contributions included in the thesis. This is a true copy of the thesis, including any required final revisions, as accepted by my examiners.

I understand that my thesis may be made electronically available to the public.

Statement of Contributions

Zohaib Atiq Khan was the main author for Chapters 1, 2, and 7 which were written under the supervision of Prof Jeff Gostick and Prof Ali Elkamel and are not used for publication.

The thesis is based on manuscripts and most of the chapters are adapted from the following publications or manuscript.

Chapter 3 is based on the following publications.

Authors: Khan ZA, Tranter TG, Agnaou M, Elkamel A, Gostick JT

Title: Dual network extraction algorithm to investigate multiple transport processes in porous materials: Image-based modeling of pore and grain-scale processes.

Journal: Computers and Chemical Engineering. 123(6), 64-77 (2019)

Contributions

Khan ZA: Conceptualization, Data curation, Formal analysis, Investigation, Methodology, Validation, Visualization, Writing original draft, Writing review and editing.

Tranter TG: Software, Validation, Visualization

Agnaou M : Sofware, Validation, Meshing

Elkamel A: Funding acquisition, Project administration, Resources, Supervision, Writing original draft , Writing review and editing.

Gostick JT: Conceptualization, Project administration, Resources, Software, Supervision, Writing original draft, Writing review and editing

<u>Chapter 4</u> is based on the following publication

Authors:	Khan ZA, García-Salaberri PA, Heenan T, Jervis R, Shearing P, Brett D, Elkamel A, Gostick JT
Title:	Probing the structure-performance relationship of lithium-ion battery cathodes using pore-networks extracted from three-phase tomograms.
Journal:	Journal of the Electrochemical Society. 167(4), 040528 (2020)

<u>Contributions</u>

Khan ZA: Conceptualization, Data curation, Formal analysis, Investigation, Methodology, Validation, Visualization, Writing original draft, Writing review and editing.

García-Salaberri PA: ANSYS Simulation, Validation, Meshing, Writing original draft

Heenan T, Jervis R, Shearing P, Brett D: Three-phase image acquisition, Writing original draft, Visualization

Elkamel A: Funding acquisition, Project administration, Resources, Supervision, Writing original draft , Writing review and editing.

Gostick JT: Conceptualization, Project administration, Resources, Software, Supervision, Writing original draft, Writing review and editing

<u>Chapter 5</u> is based on the following publication

Authors: Khan, ZA, Elkamel A, Gostick JT

Title: Efficient extraction of pore networks from massive tomograms via geometric domain decomposition.

Journal: Advances in Water Resources. 145(Nov), 103734 (2020).

Contributions

Khan ZA: Conceptualization, Data curation, Formal analysis, Investigation, Methodology, Validation, Visualization, Writing original draft, Writing review and editing.

Elkamel A: Funding acquisition, Project administration, Resources, Supervision, Writing original draft , Writing review and editing.

Gostick JT: Conceptualization, Funding acquisition, Project administration, Resources, Software, Supervision, Writing original draft, Writing review and editing

<u>Chapter 6</u> is based on the following manuscript in preparation

Authors: Khan, ZA, Sadeghi MA, Agnaou M, Elkamel A, Gostick JT

Title: Pore network modelling of galvanostatic discharge behaviour of lithium-ion battery cathodes

Contributions

Khan ZA: Conceptualization, Data curation, Formal analysis, Investigation, Methodology, Validation, Visualization, Writing original draft

Sadeghi MA: Software management, General analysis, Methodology

Agnaou M: Software development, General analysis, Methodology

Elkamel A: Funding acquisition, Project administration, Resources, Supervision, Writing original draft

Gostick JT: Conceptualization, Funding acquisition, Project administration, Resources, Software, Supervision, Writing original draft

Abstract

The advancement in high-resolution X-ray tomography image acquisition techniques has enabled imaged-based modelling of pore-scale transport processes to better understand structural performance relationship in porous media. The porous components in electrochemical energy storage devices such as lithium-ion batteries, fuel cell and redox flow batteries are subject to intense research to maximize performance and hence reduce the cost of energy storage systems. The image-based pore-scale modelling approaches such as direct numerical simulation (DNS) are, however, very computationally expensive and it gets infeasible to simulate a representative element volume of porous structure on a standard workstation or laptop machine. Pore network modelling (PNM) approach has been previously used to simulate large size porous domains of fuel cell and redox flow batteries at substantially lower computational cost, however, its application in lithium-ion batteries has not been attempted due to the multiphysics and transient nature of transport mechanism involved during charging and discharging process. Lithium-ion batteries are considered as the top candidate for electrochemical energy storage, so modelling their structure-performance relationship at less computational cost will enable development of efficient numerical pore network modelling framework. Therefore, this thesis aims towards developing pore network modelling framework for lithium-ion batteries to study the impact of microstructure on multiphysics transport processes occurring inside battery electrodes.

The development of lithium-ion battery pore network model requires enhancements in the current implementation of pore network modelling algorithms. For example, current pore network extraction algorithms only extract a single phase from a tomography image (usually the pores). On the other hand, lithium-ion battery electrodes contain three phases, namely active material (e.g.

NMC), carbon binder, and electrolyte filled void phase. To resolve this issue, multiphase pore network extraction algorithms were developed that connect any two phases via interconnections. This allowed investigating inter- and intra-phase transport processes between phases which are common in lithium-ion battery. The extraction algorithms were tested on random sphere packings and three-phase lithium-ion battery cathode and found to agree well with experimental data and DNS model. Computational performance of PNM model was also compared with other modelling approaches and found to give appreciable performance gain on large size porous domains, while yielding similar or equivalent results.

Although modelling of transport process using the PNM approach is computationally efficient, extracting pore networks from tomography images is a computationally expensive task. Also, image resolution plays a vital role to determine the relative accuracy of extracted geometrical properties and hence simulation accuracy. To remove these bottlenecks, an efficient, parallelized network extraction technique was developed that enabled pore network extraction from massive size images. A geometric domain decomposition technique was adopted to reduce the computational cost of extraction. The network extraction was observed 7 times faster and consumed 50% less RAM when used in parallel and serial mode respectively. Finally, a case study was performed to reduce the effect of resolution during pore network extraction. This enabled more reliable extracted pore networks for pore network modelling studies.

Finally, pore network modelling of lithium-ion batteries cathodes was performed to study galvanostatic discharge behaviour of half-cells. A massive reduction in computational cost was observed when compared with DNS approach. The structural features of two electrodes were investigated to understand the performance-structural relationship. Also, particle-to-particle and pore-to-pore analysis was performed to analyze the state of lithiation, solid-phase potential

distribution and lithium-ion concentration distribution, electrolyte phase potential distribution in solid and electrolyte phase respectively. The study enabled modelling of large size lithium-ion electrodes to analyze the impact of internal microstructure on the overall performance of the cell.

The presented work in this thesis is focused on developing, validating, and applying a pore network modelling framework for lithium-ion battery discharge. It has enabled the study of structural performance relationship of battery electrodes on a particle to particle basis without estimating effective transport properties using empirical or experimental data. The excellent computational performance of PNMs has allowed multiphysics modelling on standard workstation or laptop with minimal computational resources. Although developed for lithium-ion battery cathodes the developed framework can be used for any anode structure or study thermal performance-structure relationship as well.

Acknowledgements

I would like to thank Prof Jeff Gostick for his unequivocal support during my PhD studies. He helped me in shaping up my research skills and made me an expert in pore network modelling field. He always supported my research ideas during my PhD studies and introduced new platform to enhance my programming skills. I will always be grateful and indebted for whatever he did for me during my studies especially his financial support during the last year of my PhD studies.

I want to thank Prof Ali Elkamel for choosing me as his PhD student in University of Waterloo and also supporting my research work. He reviewed and gave innovative ideas at many stages and also supported me financially in the last year of my PhD program.

I cannot thank enough to University of Engineering and Technology Lahore Pakistan for sponsoring me to study in University of Waterloo and letting me grow in whatever research I wanted to do. I will try my best to return this support by adding new quality values to enhance the education and research standards of the University. Also, I would like to thank Natural Science and Engineering Research Council (NSERC), Canada for it financial support and University of Waterloo, Canada for awarding me Doctoral Thesis Award 2020 during PhD studies.

I would also like to thank some great Post Docs in PMEAL research group who share their experience of pore network modelling to solve some complex issues I faced during my research. Tom Tranter helped me validating transport properties in dual network extraction paper. Mehrez Agnaou performed direct numerical simulations on random sphere packings and Amin Sadeghi helped to remove different bugs in OpenPNM and also share his previous experience in pore network modelling to simulate lithium-ion battery pore network model. Moreover, I would like to

thank Pablo A. García-Salaberri, Thomas Heenan, Rhodri Jervis, Paul Shearing and Dan Brett who collaborated with PMEAL group to make Chapter 4 work possible.

I would also like to thank my wife Hadia who supported me during my PhD studies by bearing many family responsibilities during the last three years of PhD. She looked after my daughter during her stay in Canada so that I can focus on my PhD and helped to enhance my personality by sharing good things in Canadian culture.

Lastly, thanks to my family specially my mother and father for remembering me in their prayers and keeping me away from any unforeseen troubles that could reduce my efficiency during PhD studies. Also, thanks to my brother and sister for looking after issues in Pakistan that I was facing time to time while studying in Canada.

Waterloo, December 16, 2020

Dedication

To my wife Hadia and daughter Husna. Their smiles give me a reason to work hard

Table of Contents

List of Figures

List of Tables

Chapter 1 Introduction

1.1. Background

Due to potential environment change, fossil fuel limitations and ever-increasing energy demand, the need for electrochemical energy storage devices that can work with renewable energy sources like wind and solar is increasing at a rapid rate. Electrochemical devices like lithium-ion batteries, fuel cells, redox flow batteries and supercapacitors are being extensively used as alternative power sources in various applications like electronic devices, electric vehicles and energy storage systems [1]. This rapid increase in demand requires more detailed modelling of such systems for better prediction of performance, durability, and efficiency. The deeper understanding offered by such modeling will help in developing next-generation energy storage systems for longer cycling life, safe operation, lower cost and higher capacity.

Rechargeable batteries store and transform energy through diffusion and ionic migration in porous negative and positive electrodes separated by an enabling porous separator that restrict electron conduction while allowing ion transfer across the membrane. The porous electrodes and separator are immersed in an electrolyte solution where ionic transport processes take place to carry out the electrochemical reaction. Transport and reaction processes strongly depend on pore and solid structure of the porous electrodes and contribute significantly to the overall efficiency of power supply or energy storage in a particular device [2]. Two materials which have the same porosity can have drastically different transport and reaction rates because of the difference in pore size, shape, and connectivity, etc [3,4]. Moreover, structural features of the solid phase also impact the overall performance due to different electron and heat transport pathways of electrochemical materials. Designing optimized porous materials with enhanced performance, therefore, requires a detailed study on performance-structure relationship in electrochemical energy storage devices.

Image-based modelling of porous media is gaining importance due to the development of advance high-resolution imaging techniques like X-ray microtomography and FIB-SEM. Most lab-scale X-ray tomographic scanners can give 3D images of porous media of resolution close to 1 μm while some advanced recent generation scanners can give high-resolution images up to 10 to 20 nm voxels [5]. It is now possible to image and segment multiphase porous materials to understand key structural information like size and shapes of pores and particles in different phases [6,7]. Beside structural information the advancement in imaging technologies has led to increasing interest of studying the performance of 3D microstructures at various operating conditions for massive size domains, although excessive computational resource requirements remain a challenge [8].

In recent years, the computational power and memory of common workstations or laptops have increased rapidly while the cost of hardware has decreased significantly. This has greatly enabled researchers to investigate transport and reaction processes of porous media by making a computational mesh of 3D images and performing simulation on it. The numerical approach of this type is known as direct numerical simulation (DNS). This approach is limited to small size porous domains due to a large number of mesh nodes required to solve transport on the image and requires an exponential increase in computational cost as the size and complexity of simulation increases. To avoid this high computational cost, approximate approaches like pore network modelling are used that reduces million of mesh nodes into thousands of network nodes by making simplifications and assumptions about porous structure in 3D images. These approximations allow simulating substantially bigger size domains at very low computational cost and enable better understanding of local transport and reaction effects on overall performance of porous material in electrochemical devices [9].

Lithium-Ion batteries are currently a top candidate for many applications amongst all electrochemical energy storage devices due to their high energy densities, low self-discharge capacity, high open-circuit voltage and long life span. The high energy densities lithium-ion batteries are currently used in most of the electric vehicles in automobile industries and research to find more efficient materials is still very active. With regards to modelling of lithium-ion batteries there has been significant contributions in the last decades but modelling a 3D microstructure of porous electrode remains a challenge. One dimensional macroscopic mathematical models to represent porous heterogeneous electrodes are difficult to define properly as they represent reality only in an average sense. The porous electrodes consist of multiple phases that include a network of interconnected voids and throats in the electrolyte solution. Similarly, solid phase consists of a network of active material particles that are interconnected with carbon binder domain. These active particles are subjected to lithium intercalation, while solid conducting materials enhance the electronic mobility by providing a conductive path for a current collector to the surface of active materials particles. The transport of Li-Ions takes place inside electrolyte solution. The lithium intercalation is affected by porous structure and material properties of the composite electrode, as it is sensitive to the effective interfacial area per unit volume between active particles and an electrolyte solution. These properties greatly influence the concentration changes and potential drop in both void and solid phases [10,11]. Capturing all of these various phenomena with a macroscopic model requires many assumptions and correlations about the structure.

The macroscopic modelling of lithium-ion battery porous electrodes stems from porous electrode theory established by Newman et al [12,13]. The model uses approximate macroscopic quantities averaged over a region of porous electrodes and does not locally address microstructural geometry and processes. To describe the electrochemical process, the electrolytic solution and solid material are approximated as superimposed continua, ensuring perfect connection at all points while the battery separator is considered homogenous containing only electrolytic solution. Different non-linear partial differential equations are used to describe the transport and reaction process in the electrolyte and solid phase in an average phenomenological way and effective transport properties like effective diffusivity and conductivity are based on experimental data or empirical relations. The Pseudo 2D model developed by Doyle et al in 1993 is still used as a reference mathematical model for lithium-ion battery. Although accurate for a certain range of conditions the model has certain limitations[14–16]. For example, because of the assumption of macroscopically averaged geometrical properties, it requires many structural and transport parameters to be found using experimental techniques. Moreover, it does not describe processes in detail at the microscopic scale so cannot provide insights into the role of microstructure on performance. A detailed investigation of macroscopic homogenous models to describe Li-Ion battery can be found in Jones et al [16], where at high C-rates and high temperature, the poor predictive capacity of the model is highlighted.

To enhance the performance of lithium-ion batteries, multiphysics modelling incorporating geometrical heterogeneity of porous electrodes is a powerful tool. This will not only provide a better understanding of charging and discharging dynamics at different mode of operation but also help in developing next-generation electrode materials. Therefore, this thesis aims at developing Multiphysics models for lithium-Ion batteries to relate the microstructural heterogeneities of porous electrodes with a cell's performance. Given the advantages of pore network modelling over direct numerical simulation (DNS) and availability of visualization techniques to capture details of porous material, a modelling framework of lithium-Ion battery electrode was developed. This pore network model of Li-ion battery was used to study structural-performance characteristics to help remove bottlenecks in 3D mictrostructure and predict next-generation battery electrodes that perform optimally at a given set of conditions.

1.2. Motivation and Organization

This thesis is centered on understanding the transport and reaction processes in porous components of electrochemical energy storage devices, and specifically lithium-ion batteries. Most of the modelling studies in this regard are based on macroscopic models that neglect the microscopic geometrical heterogeneities of the porous material. Study of such heterogeneities will allow understanding of local effects in microstructure and hence allow increasing the performance of the battery by tailoring structural information of the electrode. Recently, there have been some studies on pore-scale modelling of transport processes in fuel cell and redox flow batteries [17–19] but lithium-ion batteries modelling studies including internal structure information are very few [3,20]. This is due to the transient, non-linear and multiphysics nature of transport and reaction processes that are computationally expensive to simulate on a large size porous domain. This gap in the literature can be filled by adopting less computationally expensive modelling approaches like pore network modelling which is well established in geoscience but to date has not been used to simulate lithium-ion batteries.

Therefore, the motivation behind this thesis is to develop a modelling framework which incorporates pore network modelling of lithium-ion batteries to understand multiphysics transport phenomena occurring inside porous electrodes based only on tomographic images of microscale structure. Given the advantages of pore network modelling (PNM) over direct numerical simulation (DNS), the framework will integrate structural features of porous electrodes to study the effect of material heterogeneities on charging and discharging cycle of the batteries. For this purpose, many advances in PNMs were required before modelling batteries at pore-scale level. For example, solid-phase structural properties are overlooked in current pore network models and only void phase structure is considered. However, in battery modelling, solid structure is equally important as it provides surface area for Li-intercalation, volume for Li storage, and transport pathway of electrons. Moreover, in order to simulate a truly large domain of porous electrodes, efficient algorithms for extracting void and solid networks are required which incorporates accurate geometrical features of the porous structure in large size domains. The solution of these challenges will not only enable the investigation of charging and discharging dynamics of porous electrodes in Li-Ion batteries but also it will open a new avenue in understanding many different transport processes like reaction-diffusion in catalyst beds and conductive and convective heat transfer in porous media.

The thesis is organized into six chapters. Chapter 1 describes the general background and motivation behind current work. Chapter 2 provides a literature survey on the subjects of multiphysics modelling of lithium-ion battery, pore network modelling approach, its benefits, and application of pore network modelling in lithium-ion batteries. Chapter 3 describes a dual network extraction algorithm developed as part of this work that extracts networks of void and solid microstructures from 3D images along with interconnections between void and solid phase. This study was performed to investigate multiple transport processes in both solid and void phase which are common in lithium-ion batteries. Chapter 4 extends the dual network algorithm to an arbitrary number of phases and applies it to a 3-phase image of a Li-ion cathode material to extract active material, carbon binder and electrolyte phase networks. The interconnected network was then used to simulate a reaction-diffusion and reaction-conduction transport process in the void and solid-phase respectively to validate interphase transport and reaction kinetics. Chapter 5 describes an efficient methodology utilizing parallelization to extract networks from massive size tomograms in less computational time. Chapter 6 combines the work of the previous chapters to implement a transient Multiphysics pore network model of lithium-ion cathodes to study discharge dynamics at various C-rates. This model allowed us to analyze the effects of microstructural heterogeneities on the performance of lithium-ion battery. Lastly, Chapter 7 summarizes important findings and conclusions from all studies mentioned above. Some key ideas are suggested for future work.

Chapter 2 Literature Review

This chapter provides general information and background on the main parts of the thesis. Section 2.1 describes the standard, continuum-based multiphysics models of lithium-ion battery and highlights the key issues faced to model such systems on a porous domain. Section 2.2 describes pore network modelling approach along with its benefits and limitations in comparison to other modelling approaches. Section 2.3 is dedicated to network extraction algorithms used to obtain pore networks from tomography images. Section 2.4 explains mathematical formulation of pore network modelling on real geometries. Section 2.5 is dedicated to highlighting current efforts to model lithium-ion batteries using pore network modelling and importance of present studies in the context of lithium-ion battery modelling.

2.1. Transport Process in lithium-Ion Batteries

The basic components of lithium-ion battery are the same as other electrochemical energy storage devices with two porous electrodes separated by a porous membrane and current collectors connected with each electrode as shown in Figure 2.1. The porous cathode consists of electrochemically active material like lithium nickel manganese cobalt oxide ($LiNi_{0.33}Mn_{0.33}Co_{0.33}O_2$), lithium cobalt oxide ($LiCoO_2$), lithium iron phosphate ($LiFePO_4$) surrounded by carbon and binder material that enhance the electronic conductivity of solid phase. The solid phase (active material + carbon and binder) is surrounded by electrolyte solution in porous phase that contains lithium-ion during charging and discharging process. The anode is made up of carbon or lithium metal that provides electrons and lithium-ion during battery operation. The porous membrane is used as a separator between the electrodes and contains pores that are approximately 1/10th the size of pores in the electrodes. The current collectors are made up of metals such as copper and aluminum to collect or receive electrons during battery operations.

During the discharge process, lithium-ion and electrons are generated at anode side and travel towards the cathode through the porous membrane and external circuit, respectively. The electrochemical reaction takes place at the electrolyte-active material interface where lithium-ion gain an electron and convert into lithium that accumulates or intercalates into the active material. This process of lithium-Ion travelling from anode to cathode and back to anode greatly depends on the transport pathways and reactions kinetics in porous electrodes. The reversible reaction of lithium-ion battery with lithium metal as anode and $LiNi_{0.5}Mn_{0.3}Co_{0.2}O_2$ as cathode material is shown in following equation.

Anode: $Li \rightleftharpoons Li^+ + e^-$

Cathode: $Li^+ + e^- + Ni_{0.5}Mn_{0.3}Co_{0.2}O_2 \rightleftharpoons LiNi_{0.5}Mn_{0.3}Co_{0.2}O_2$

Overall: $Li + Ni_{0.5}Mn_{0.3}Co_{0.2}O_2 \rightleftharpoons LiNi_{0.5}Mn_{0.3}Co_{0.2}O_2$ (2.1)

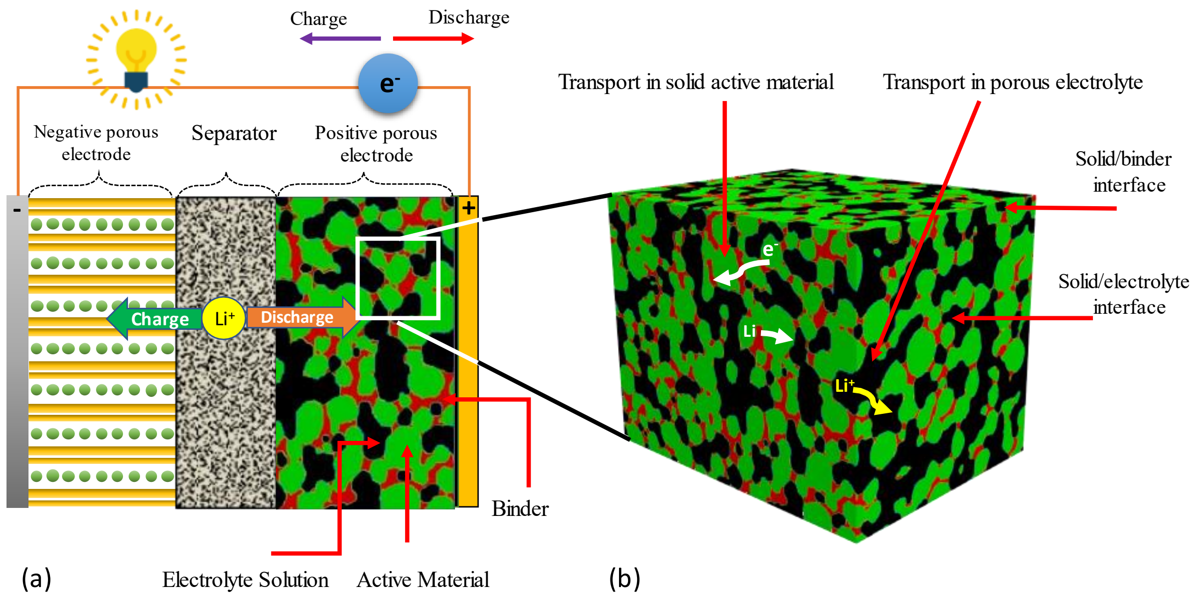

Figure 2.1 a) Lithium Ion battery full cell schematic, b) Porous cathode structure

In the past, many approaches had been used to model lithium-ion batteries. These models can be classified as either empirical or physics-based models. The empirical models rely on experimental discharge data and not directly concerned with the microstructure variations in battery electrode and separator and therefore, will not be discussed in detail in this thesis.

On the other hand, physics-based models are based on electrochemical transport and kinetic equations of ions and electrons and follows porous electrode theory of Newman et al. In this regard Pseudo two dimensional (P2D) models are most widely used. Other physics-based models include single particle and multi-particle models and are simplifications of the P2D approach that attempt to reduce the computational cost. This thesis focus on eliminating many structural simplifications of P2D model on lithium ion electrodes using pore network modelling framework so this model is briefly discussed later in this section.

2.1.1. **Pseudo-two-dimensional models**

Starting in 1975, Newman and his coworkers established porous electrode theory for battery applications [12]. They applied the continuum approximation which assumes that the porous structure is a continuous domain with effective properties, both predicted and measured. This model does not incorporate microstructural features of Li-Ion electrodes which is essential to find the interfacial area between the solid and void phase, and hence effects the overall electrochemical dynamics. This model is by far the most widely used approach to predict the performance of Li-Ion batteries and is validated and thoroughly tested by Doyle et al. with experimental and mathematical data [21].

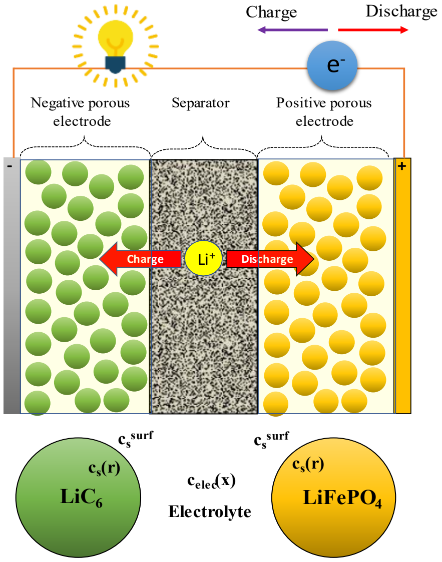

Figure 2.2 Schematic of Pseudo Two Dimensional (P2D) Model

As shown in Figure 2.2 in the P2D model considers the porous structure of electrodes as spherical particles surrounded by an electrolyte solution. However, the spheres are not explicitly resolved but are assumed to impact transport through the continuum using effective medium approximations (i.e. Bruggeman expression), the reliability of which is still controversial for non-spherical particles [22]. The transport of Li-Ions through intercalation and deintercalation occurs at the interfacial area of the spherical particles which is also predicted via correlations. Moreover, ion transport is considered to be unidirectional so 1-D mathematical equations can be applied in the model. The main governing equations of the P2D model are as follows.

Table 2.1 Nomenclature

Definition	**Symbol**
Concentration of Li-Ion in solid phase	c_s
Diffusivty of active material phase	D_{AM}
Radius of particle	r
Effective diffusivty in void phase	$D_{eff}^{Li^+}$
Interfacial area of porous electrode	a_k
Transference number	t_+
Pore-wall flux density averaged over interfacial area	J_k
Concetration of Li-ion in electrolyte and separator	c_{elec}
Effective conductivty of active material phase	σ_{eff}^{AM}
Effective conductivty of carbon binder phase	σ_{eff}^{CBD}
Solid phase potential	φ_s
Faradays constant	F
Effective conductivity of solution phase	k_{eff}
Electric potential of electrolyte phase	φ_{elec}
Current	I
Concentration of Li-ion at surface of particle	c_s^{surf}
Concentration of Li-ion at center of particle	c_s^{max}
Surface overpotential	u_s
Open circuit voltage	U_k
State of charge	soc

The solid phase transport of Li-Ion inside spherical particles is described using Fick's second law of diffusion.:

$$\frac{\partial c_s}{\partial t} = \frac{D_{AM}}{r^2}\frac{\partial}{\partial r}\left(r^2\frac{\partial c_s}{\partial r}\right) \tag{2.2}$$

The definition of terms is shown in Table 2.1. The transport of Li-Ion inside electrolyte phase of cathode/anode and separator is described using conservation equation ((2.3) and Fickian diffusion equation ((2.4) respectively:

$$\frac{\partial c_{elec}}{\partial t} = \frac{\partial}{\partial x}\left(D_{eff}^{Li^+}\frac{\partial c_{elec}}{\partial x}\right) + \frac{D_{eff}^{Li^+}zF}{RT}\frac{\partial}{\partial x}\left(c_{Li^+}\frac{\partial \varphi_{elec}}{\partial x}\right) \tag{2.3}$$

$$\frac{\partial c_{sep}}{\partial t} = \frac{\partial}{\partial x}\left(D_{eff}^{Li^+}\frac{\partial c_{sep}}{\partial x}\right) \tag{2.4}$$

The electric potential of the active material phase is calculated using Ohm's Law. The charge balance in active material particle is represented by equation (2.5) as follows:

$$\frac{\partial}{\partial x}\left(\sigma_{eff}^{AM}\frac{\partial \varphi_s}{\partial x}\right) = a_k.F.J_k \tag{2.5}$$

The electric potential of the carbon binder domain phase is calculated using Ohm's Law:

$$\frac{\partial}{\partial x}\left(\sigma_{eff}^{CBD}\frac{\partial \varphi_s}{\partial x}\right) = 0 \tag{2.6}$$

The electric potential in the liquid phase ((2.7) and in the separator ((2.8) is calculated using ohms and Kirchoff's law:

$$-\sigma_{eff}\frac{\partial\varphi_s}{\partial x}-k_{eff}\frac{\partial\varphi_{elec}}{\partial x}+\frac{2k_{eff}RT}{F}(1-t_+)\frac{\partial ln\, c_{elec}}{\partial x}= \ I \tag{2.7}$$

$$-k_{eff}\frac{\partial\varphi_{elec}}{\partial x}+\frac{2k_{eff}RT}{F}(1-t_+)\frac{\partial ln\, c_{elec}}{\partial x}= \ I \tag{2.8}$$

The flux of Li-Ion the solid-void interface is calculated using Butler-Volmer kinetics equation:

$$J_k = K_k\left(c_s^{max}-c_s^{surf}\right)^{0.5}\left(c_s^{surf}\right)^{0.5}(c_{elec})^{0.5}\left[exp\left(\frac{0.5Fu_s}{RT}\right) - \ exp\left(-\frac{0.5Fu_s}{RT}\right)\right] \tag{2.9}$$

$$u_s = \ \varphi_s - \ \varphi_{elec} - OCV \tag{2.10}$$

$$V_{cell} = \ \varphi_{s|x=0} - \ \varphi_{s|x=L} \tag{2.11}$$

The open-circuit potential (OCV) depends on the type of material and battery operating temperature. In battery modelling, SOC-OCV models are used to fit with experimental data. This fitting can either is based polynomial, logarithmic, exponential or hybrid in nature[23]. For example, a general form of hybrid SOC-OCV model is as follows:

$$OCV(soc) = \mathrm{p_0soc^n} + \ \mathrm{p_1soc^{n-1}} \dots\dots \ \mathrm{p_{n-1}soc^1} + \mathrm{p_n} + q.e^{r.\ soc^s} \tag{2.12}$$

Based on equation (2.12) , SOC-OCV for $LiNi_{0.5}Mn_{0.3}Co_{0.2}O_2$ cathode material is as follows[10]:

$$
\begin{aligned}
OCV = & -3640\,soc^{14} + 13176\,soc^{13} - 14557\,soc^{12} - 1571\,soc^{11} + 12656\,soc^{10} - 2058 \\
& soc^{9} - 10744\,soc^{8} + 8698\,soc^{7} - 829.8\,soc^{6} - 2074\,soc^{5} + 1190\,soc^{4} - 272.5 \\
& soc^{3} + 27.23\,soc^{2} - 4.158\,soc + 5.3147 - 5.5732e^{-4} \exp(6.56\,soc^{41.48})
\end{aligned} \tag{2.13}
$$

For the simultaneous solution of these equation numerical approaches like finite element method, finite volume method and finite difference methods are used as currently there are no complete analytical solutions to this model available. The commercial software like COMSOL Multiphysics and Battery Design Studio (BDS) use FDM and FEM approaches to solve P2D model efficiently.

2.2. Pore Network Modelling

Pore Network Modelling (PNM) is a well-established pore-scale modelling approach most widely used in geosciences. It's typically used to find effective properties and percolation mechanism in partially water saturated porous rock samples, which are difficult to obtain experimentally. This approach treats a porous domain as a network of interconnected pores where two pores bodies are connected via throat. This assembly of two pores and throat is called conduit and a simple representation is shown in Figure 2.3. The conductance of each conduit takes place from the centre of one pore to other pore center via series resistor theory expressed as:

$$G^{tr}_{conduit_{i,j}} = \left(\frac{1}{g^{tr}_{pore_i}} + \frac{1}{g^{tr}_{throat_{i,j}}} + \frac{1}{g^{tr}_{pore_j}}\right)^{-1} \tag{2.14}$$

where the superscript tr indicates the type of transport process like diffusion, advection etc. g is the conductance values of individual pore or throat and G is the overall conductance of conduit obtained via series resistor theory.

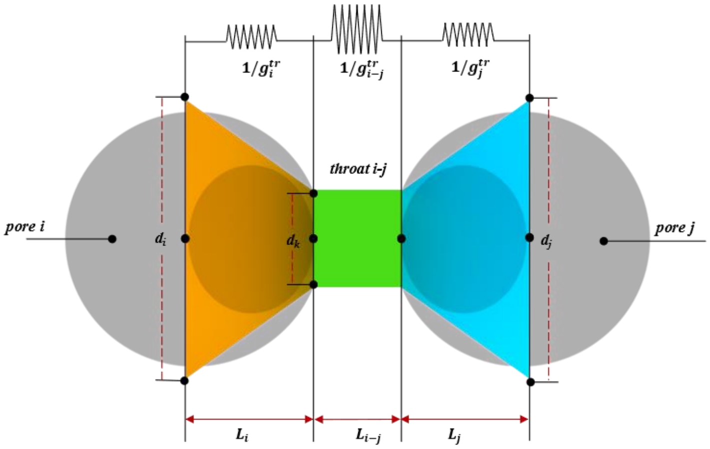

Figure 2.3 Simple pore-throat-pore conduit schematic in pore network modelling

The pore locations correspond to real positions of voids inside porous materials and interconnections between two pores is known as a throat that constricts the path between two pores. In typical pore-scale modelling approach like finite element method (FEM) and Lattice Boltzmann method (LBM) the individual pores are further subdivided into small mesh elements or lattice cells that fill the porous structure, but pore network modelling assumes one pore as one element without any further subdivision. The PNM approximation therefore greatly decreases the number of elements to be solved for a particular transport process and enables user to simulate relatively bigger size porous domain than FEM or LBM approach.

In pore network modelling the definition of a pore as one element leads to many simplifications in modelling transport processes without losing structural information of the porous material. For example, one-dimensional conservation laws, which generally have simple analytical solutions, can be used to model transport phenomena by simplifying the governing equations. This reduces the total number of unknown for three-dimensional problem and increases the computational efficiency of model solution. Lastly, since a pore represents a region in porous domains any local change in transport property can be monitored independently. This enables the investigation of structural effects by, for instance, removing certain choke points from the porous material to ascertain which how the performance may increase and it such measures should be considered experimentally. The connection between structure and performance is fully explicit.

To quantitatively compare the computational efficiency of pore network modelling with direct numerical simulation like FEM or LBM Figure 2.4 shows a two meshed surface using FEM method and extracted pore network of porous material. The total number of mesh elements in 2D porous domain has approximately 77815 respectively while the equivalent pore network has only 77 number of pores. It can be seen that solution of a transport process in pore network will be very fast as compared to FEM method because of the vastly smaller number of unknown elements. As a general rule, most of the mathematical solvers in programming languages can solve approximately 10^6 unknowns with ease on a standard workstation. On average, it takes 10^4 elements to mesh a single pore using FEM method. This allows only simulating about 100 pores in whole domain. On the other hand, pore network modelling can simulate one pore for each unknown, i.e. 1,000,000 pores, for a 10,000 x increase in comparable domain volumes. This computational benefit not only allows simulating bigger domains but also transient simulations and coupled multiphysics that require iterations can be performed without too much computational cost. This key feature of pore network modelling becomes very important for lithium-ion battery modelling where overall transport processes are transient, non-linear and multiphysics in nature.

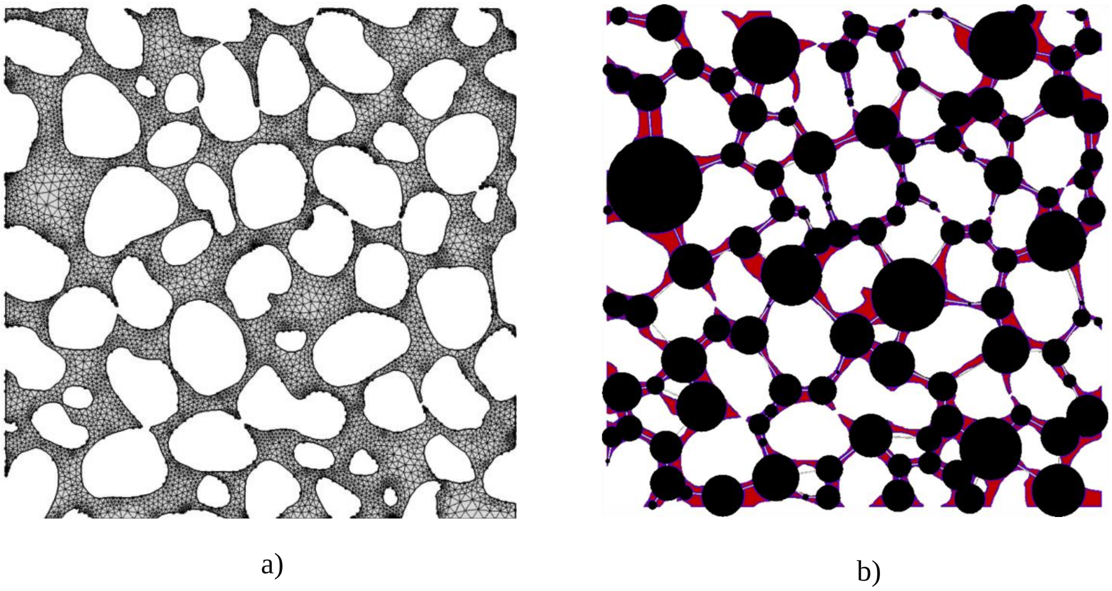

a) b)

Figure 2.4 a) Meshed domain of porous materials for direct numerical simulation, b) Extracted pore network of same porous material

2.3. Pore Network Extraction

Although pore network modelling is computationally more efficient than FEM or LBM method, this efficiency comes at a cost of losing geometrical details of individual pores or throats because of abstraction in porous material structural information. For example, pores are assumed as sphere or cubes and throats are considered cylinder or rectangular ducts in a 3D dimensional domain. This approximation results in a decrease in accuracy or modelling results and greatly depends on how these abstractions are extracted from the porous domain.

Pore networks can be classified into two categories: The generated network and extracted network as seen in Figure 2.5. Generated networks are used when acquiring 3D image of porous media is difficult, the domain size is very big, or it’s not readily available. Such networks represent porous media only in an idealized manner and geometrical properties are adjusted iteratively until a good agreement is achieved with actual porous media. On the other hand, extracted networks are based on direct mapping a network onto the porous structure. This approach involves extracting the pore network from actual tomographic image of porous material using image processing techniques and gives one to one spatial correspondence between extracted network and corresponding porous domain. This approach gives a more accurate representation of porous material since spatial locations, geometric information, as well as its connections with neighbour pores can be estimated directly. All of the studies performed in this thesis are based on extracted, therefore the literature related to this approach is reviewed below. There are three main models used to extract irregular networks from 3D images.

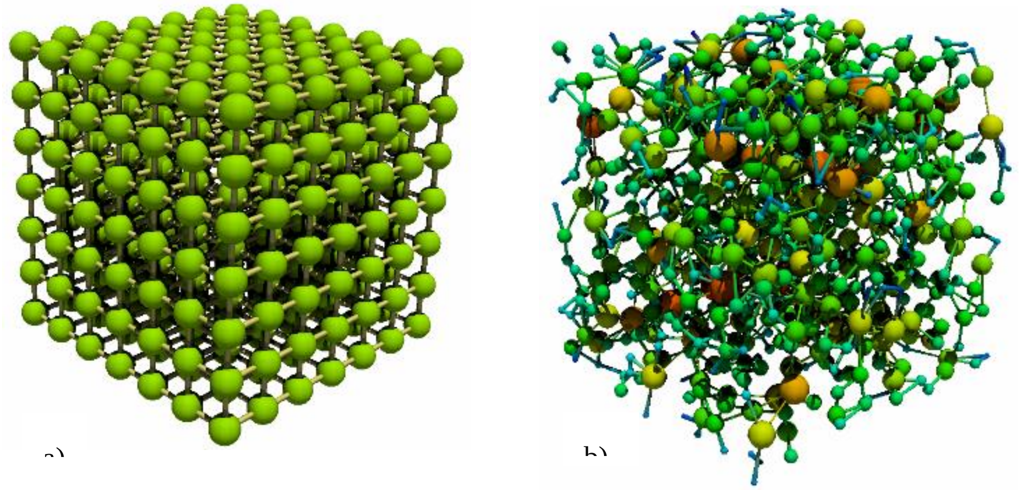

Figure 2.5 a) Generated Network, b) Extracted Network

2.3.1. Medial Axis Models

The medial axis approach transforms void space in 3D image into a topological skeleton that runs approximately in the centre of the void space. The method was first studied by Lindquist et al [24]. Since then different types of medial axis algorithms have been used, mainly differing based on the order of thining, the type of distance transform used and the steps adopted to retain the topology of the material. The medial axes can be obtained by the morphological thinning approach developed by Baldwin et al [25] or by voxel space burning algorithm developed by Lindquist et al [24]. The latter approach uses erosions technique to reduce void space from grain surface until the voxel burning reaches one voxel from different directions. The pore locations were determined at node points while pore throats were determined by dilating the medial axis to a point where it touches with grain surface.

Although medial axis preserves the void topology effectively, it is difficult to identify pores properly. Voids space sometimes covers multiple medial axis junctions and predicts higher coordination number. Therefore, it requires complex trimming rules to merge medial axis skeleton junctions into each other to avoid unrealistically high coordination numbers [26]. Moreover, it also requires a throat threshold factor which requires the examination of flow simulations for accurate prediction. In general, medial axis algorithm is good in defining the topology of void structure but they pose problems in identifying the voids.

2.3.2. Maximal Inscribed Ball Models

This algorithm was first developed by Silin et al [27] and later extended by Al-Kharusi and Blunt. The algorithm finds the largest inscribed spheres at each voxel inside the void space and trims off spheres that are engulfed by larger inscribed spheres. The remaining spheres are labelled as maximal balls which describe the void space, while small balls connecting two maximal balls are labelled as throats. To define voids and throats effectively Dong et al developed a clustering process in which all remaining balls were hierarchized by family trees based on their size and rank. In this clustering process, the ancestor or master balls were labelled as void location and common child balls were labelled as throats. The method, however, is computationally expensive and time-consuming and was limited to a small number of voids. It also predicted high coordination numbers, and throat sizes are underpredicted leading to erroneous capillary pressures [28].

2.3.3. Watershed Segmentation Models

Watershed segmentation is a well-known image partitioning technique, often used for separating cells on microscope slide image. It has great potential to extract void networks from tomographic images as it can represent voids space as catchment basin in the contour map. The earliest research for developing void network models can be traced back to the work of Thompson et. al [29] they used watershed segmentation to partition grain space. They then used Delaunay tessellation to determine the void centres by morphological analysis inside Delaunay tetrahedron. The algorithm was validated on low porosity sandstone image. The validity of this method for non- spherical grains and high porosity images poses issues due to image over-segmentation. In general, the algorithms computational cost was an order of magnitude lower than maximal ball algorithm.

The next advancement in network extraction using watershed segmentation came with the studies of A.P Sheppard et al [30] and Rabbani el al [31]. Sheppard et al extracted and analysed pore networks on several different rocks such as sandstones, carbonates, unconsolidated cores and sphere packings. Similarly, Rabbani et. al developed an algorithm to extract void network using distance transform and watershed segmentation. They extracted pore networks of Berea sandstone and carbonate rocks and found excellent agreement with maximal inscribed ball algorithm explained above. Their algorithm was demonstrated for low porosity samples but also suffered from over-segmentation of void space regions in high porosity regions.

Recently, Gostick [28] refined the watershed-based approach for high porosity material by extracting a sub-network of the over-segmented watershed (SNOW). This algorithm utilized a special version of the watershed transform that allows custom specification of the basin locations. This was leveraged by removing several types of spurious peaks in the distance transform that lead to over-segmentation in the watershed step, especially in high porosity images. Importantly, the SNOW algorithm was shown to generally work for both high and low porosity materials. The SNOW algorithm accepts a binary image with 0's as solid phase and 1's as void phase and performs distance transform on it. A maximum filter is applied to find peaks which will become the basins of the watershed transform, and then extraneous peaks are trimmed which is the key to avoiding over-segmentation. In the next step, watershed segmentation is performed on the remaining peaks to get void regions as catchment basins in the network. Lastly, the segmented image is scanned one region at a time to extract the network information such as pore size and neighbour throats. The algorithm is efficient in terms of computational performance in comparison with the maximal inscribed ball and predicts geometrical properties accurately in wide porosity range of materials. The results of these steps is shown in Figure 2.6.

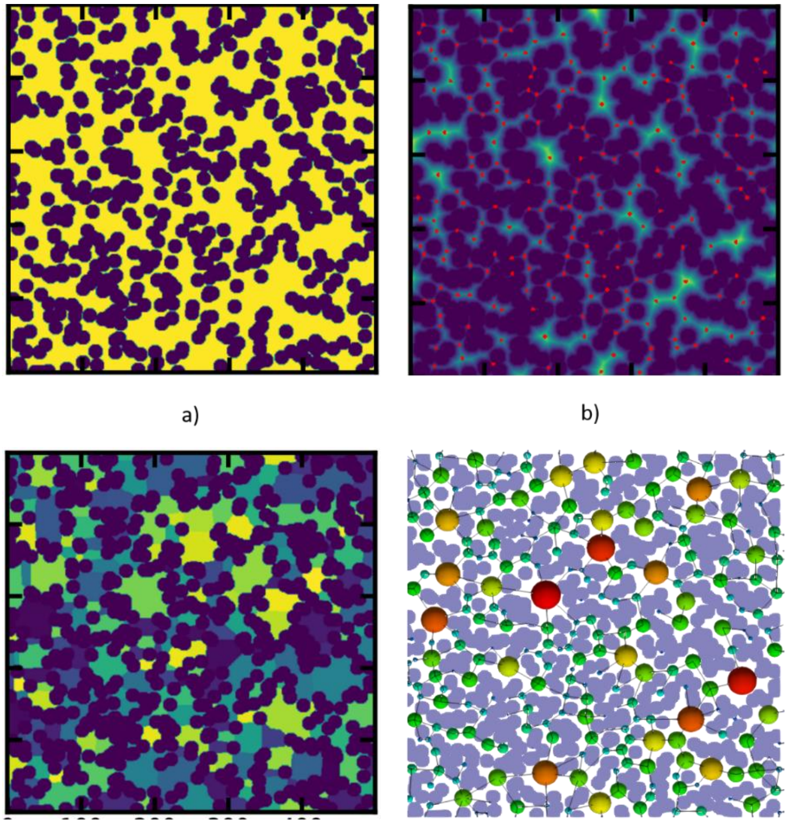

a)

b)

c)

d)

Figure 2.6 a) Binary image with yellow color is void phase, b) Peaks detected by SNOW algorithm to perform watershed segmentation overlayed on distance transformed image, c) Watershed segmentation calculated at specified marker, d) Pore network extracted from segmented image

2.4. Pore Network Modelling Mathematical Formulation

Although pore network modelling is extensively used to simulate steady state transport processes in porous rocks as well as in energy storage systems such as fuel cell and redox flow batteries but its usage in transient problems is not widely utilized. Therefore, in order to simulate transient nature of lithium ion batteries, pore network modelling algorithm capabilities needs to be extended for transient processes. This section explains the implementation and validation of the transient algorithm in open source python package OpenPNM [32].

2.4.1. Implementation of transient algorithm

As shown in Figure 2.7 the unsteady state material balance around void *i* surrounded by its neighboring void *j* without any source term can be written according to equation (2.15).

$$V^i \frac{dc^i}{dt} = \sum_j D_{bulk}^{i,j} A^{i,j} \frac{\left(c^i - c^j\right)}{\Delta x^{i,j}} \qquad \textbf{(2.15)}$$

also

$$r_{i,j} = \frac{\Delta t \, D_{bulk}^{i,j} A^{i,j}}{V^i \Delta x^{i,j}} \qquad (2.16)$$

where *V* is the volume of void *i*. *c* is the concentration inside voids. *D* is bulk diffusion coefficient of fluid. *A* is the cross-sectional area of throat connecting two voids and Δ*x* is void to void length which includes two half voids and complete interconnecting throat length.

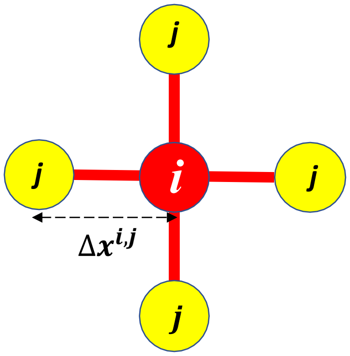

Figure 2.7 Connectivity of void i with all other neighboring void j

For steady state process the left hand side of equation (2.15) is zero and $r_{i,j}$ does not have V^i and Δt terms. The discretized equation (2.15) can be solved numerically using finite difference methods (FDM) for example explicit method, implicit method and Crank Nicolson technique. The generalized solution of all these methods can be written as follows:

Explicit Method:

$$\mathrm{C}^{\mathrm{t}+\Delta \mathrm{t}} = \mathbf{A}.\,\mathrm{C}^{\mathrm{t}} \tag{2.17}$$

Implicit Method:

$$\mathbf{B}.\,\mathrm{C}^{\mathrm{t}+\Delta \mathrm{t}} = \mathrm{C}^{\mathrm{t}} \tag{2.18}$$

Crank Nicolson Method:

$$\mathbf{D}.\,\mathrm{C}^{\mathrm{t}+\Delta \mathrm{t}} = \mathbf{E}.\,\mathrm{C}^{\mathrm{t}} \tag{2.19}$$

The explicit method is computationally faster but less stable. It requires small time interval to set for stability reasons and becomes infeasible for long time simulation. On the other hand, Crank Nicolson technique is more stable but relatively requires high computational cost then explicit and implicit scheme. The Implicit scheme is a good compromise between accuracy and computational time.

In the above-mentioned schemes, **A, B, D and E** represent $(N\ x\ N)$ matrices containing associated geometrical and transport properties terms in each void-throat-void conduit of N number of voids. $\mathrm{C}^{\mathrm{t}+\Delta \mathrm{t}}$ and C^{t} are column vectors of concentration in N number of voids. The structure of A, B, D and E is different in equation (2.17), (2.18), and (2.19) and is highly dependent on the coordination number of voids inside the pore network. As shown in Figure 2.8, for a 2D dimensional random network with 9 voids including one boundary void label 0, **A, B, D**, **E** and C^{t} can be represented as follows:

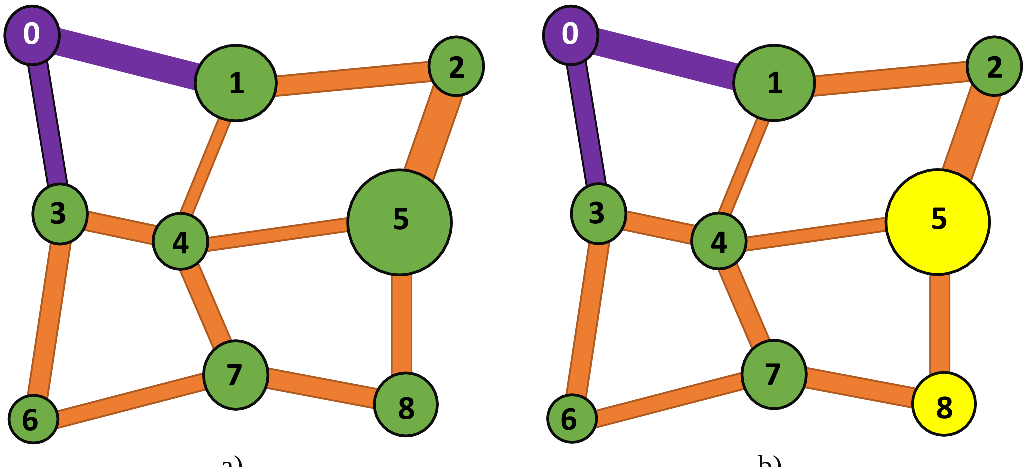

Figure 2.8 a) Random Pore network model without source term b) Pore network model with source term. Label 5 and 8 pores are going through reaction

$$\boldsymbol{A}=\begin{bmatrix}1 & 0 & 0 & 0 & 0 & 0 & 0 & 0 & 0\\ r_{10} & 1-r_{10}-r_{12}-r_{14} & r_{12} & 0 & r_{14} & 0 & 0 & 0 & 0\\ 0 & r_{12} & 1-r_{12}-r_{25} & 0 & 0 & r_{25} & 0 & 0 & 0\\ r_{30} & 0 & 0 & 1-r_{30}-r_{34}-r_{36} & r_{34} & 0 & r_{36} & 0 & 0\\ 0 & r_{41} & 0 & r_{43} & 1-r_{41}+r_{43}-r_{45}-r_{47} & r_{45} & 0 & r_{47} & 0\\ 0 & 0 & r_{52} & 0 & r_{54} & 1-r_{52}-r_{54}-r_{58} & 0 & 0 & r_{58}\\ 0 & 0 & 0 & r_{63} & 0 & 0 & 1-r_{63}-r_{67} & r_{67} & 0\\ 0 & 0 & 0 & 0 & r_{74} & 0 & r_{76} & 1-r_{74}-r_{76}-r_{78} & r_{78}\\ 0 & 0 & 0 & 0 & 0 & r_{85} & 0 & r_{87} & 1-r_{85}-r_{87}\end{bmatrix}$$

$$\boldsymbol{B}=\begin{bmatrix}1 & 0 & 0 & 0 & 0 & 0 & 0 & 0 & 0\\ -r_{10} & 1+r_{10}+r_{12}+r_{14} & -r_{12} & 0 & -r_{14} & 0 & 0 & 0 & 0\\ 0 & -r_{12} & 1+r_{12}+r_{25} & 0 & 0 & -r_{25} & 0 & 0 & 0\\ -r_{30} & 0 & 0 & 1+r_{30}+r_{34}+r_{36} & -r_{34} & 0 & -r_{36} & 0 & 0\\ 0 & -r_{41} & 0 & -r_{43} & 1+r_{41}+r_{43}+r_{45}+r_{47} & -r_{45} & 0 & -r_{47} & 0\\ 0 & 0 & -r_{52} & 0 & -r_{54} & 1+r_{52}+r_{54}+r_{58} & 0 & 0 & -r_{58}\\ 0 & 0 & 0 & -r_{63} & 0 & 0 & 1+r_{63}+r_{67} & -r_{67} & 0\\ 0 & 0 & 0 & 0 & -r_{74} & 0 & -r_{76} & 1+r_{74}+r_{76}+r_{78} & -r_{78}\\ 0 & 0 & 0 & 0 & 0 & -r_{85} & 0 & -r_{87} & 1+r_{85}+r_{87}\end{bmatrix}$$

$$\boldsymbol{D}=\begin{bmatrix}1 & 0 & 0 & 0 & 0 & 0 & 0 & 0 & 0\\ -r_{10} & 2+r_{10}+r_{12}+r_{14} & -r_{12} & 0 & -r_{14} & 0 & 0 & 0 & 0\\ 0 & -r_{12} & 2+r_{12}+r_{25} & 0 & 0 & -r_{25} & 0 & 0 & 0\\ -r_{30} & 0 & 0 & 2+r_{30}+r_{34}+r_{36} & -r_{34} & 0 & -r_{36} & 0 & 0\\ 0 & -r_{41} & 0 & -r_{43} & 2+r_{41}+r_{43}+r_{45}+r_{47} & -r_{45} & 0 & -r_{47} & 0\\ 0 & 0 & -r_{52} & 0 & -r_{54} & 2+r_{52}+r_{54}+r_{58} & 0 & 0 & -r_{58}\\ 0 & 0 & 0 & 0.-r_{63} & 0 & 0 & 2+r_{63}+r_{67} & -r_{67} & 0\\ 0 & 0 & 0 & 0 & -r_{74} & 0 & -r_{76} & 2+r_{74}+r_{76}+r_{78} & -r_{78}\\ 0 & 0 & 0 & 0 & 0 & -r_{85} & 0 & -r_{87} & 2+r_{85}+r_{87}\end{bmatrix}$$

$$\boldsymbol{E}=\begin{bmatrix}1 & 0 & 0 & 0 & 0 & 0 & 0 & 0 & 0\\ r_{10} & 2-r_{10}-r_{12}-r_{14} & r_{12} & 0 & r_{14} & 0 & 0 & 0 & 0\\ 0 & r_{12} & 2-r_{12}-r_{25} & 0 & 0 & r_{25} & 0 & 0 & 0\\ r_{30} & 0 & 0 & 2-r_{30}-r_{34}-r_{36} & r_{34} & 0 & r_{36} & 0 & 0\\ 0 & r_{41} & 0 & r_{43} & 2-r_{41}+r_{43}-r_{45}-r_{47} & r_{45} & 0 & r_{47} & 0\\ 0 & 0 & r_{52} & 0 & r_{54} & 2-r_{52}-r_{54}-r_{58} & 0 & 0 & r_{58}\\ 0 & 0 & 0 & r_{63} & 0 & 0 & 2-r_{63}-r_{67} & r_{67} & 0\\ 0 & 0 & 0 & 0 & r_{74} & 0 & r_{76} & 2-r_{74}-r_{76}-r_{78} & r_{78}\\ 0 & 0 & 0 & 0 & 0 & r_{85} & 0 & r_{87} & 2-r_{85}-r_{87}\end{bmatrix}$$

$$C^t = \begin{bmatrix} c_0 \\ c_1 \\ c_2 \\ c_3 \\ c_4 \\ c_5 \\ c_6 \\ c_7 \\ c_8 \end{bmatrix}^t$$

2.4.2. Validation

Validity of pore network modelling framework of transient Fickian diffusion algorithm was performed to check the accuracy of modeling technique on a real porous structure. For this purpose X-ray tomography images of SGL24AA and Toray120A gas diffusion layers of PEMFC were used for which experimental effective diffusion coefficients have been measured by Rashapov et al [33]. The geometrical properties for both GDLs are mentioned in Table 2.2.

Table 2.2 Geometrical Properties of gas diffusion layers

	SGL25AA	**Toray120A**
Dimension (voxels)	1500 x 1500 x 150	1500 x 1500 x 221
Resolution (µm/voxel)	1.33	1.33
Porosity (%)	81.2	65.3

Oxygen with bulk diffusivity D_b of 2.14 x 10^{-5} cm^2/s was diffused transiently from one boundary of GDL. The concentration of oxygen at the opposite side was measured with time. The results of extracted pore network from XCT images were compared by fitting analytical expression equation (2.20) on experimental data as shown in Figure 2.9.

$$C = C_0 \sum_{n=-\infty}^{\infty} \left\{ erf\frac{h + 2nl - x}{4\sqrt{Dt}} + erf\frac{h - 2nl + x}{4\sqrt{Dt}} \right\} \tag{2.20}$$

where n ranges from 0 to ∞. l is the total length of GDL. h is confinement region where diffusion needs to be calculated. x is a spatial interval where concentration is calculated. It can be seen in Figure 2.8 that transient mass diffusion fits well with experimental data for both SGL25A and Toray 120A. The comparison of effective diffusivity can be seen in Table 2.3 for both studies.

Table 2.3 Validation of pore network model with experimental data

Model	**SGL25A**	**Toray120A**
	D_{eff} (mm^2/s)	D_{eff} (mm^2/s)
Rashapov et al (2016)	14.54	12
Pore Network Model	12	9.8

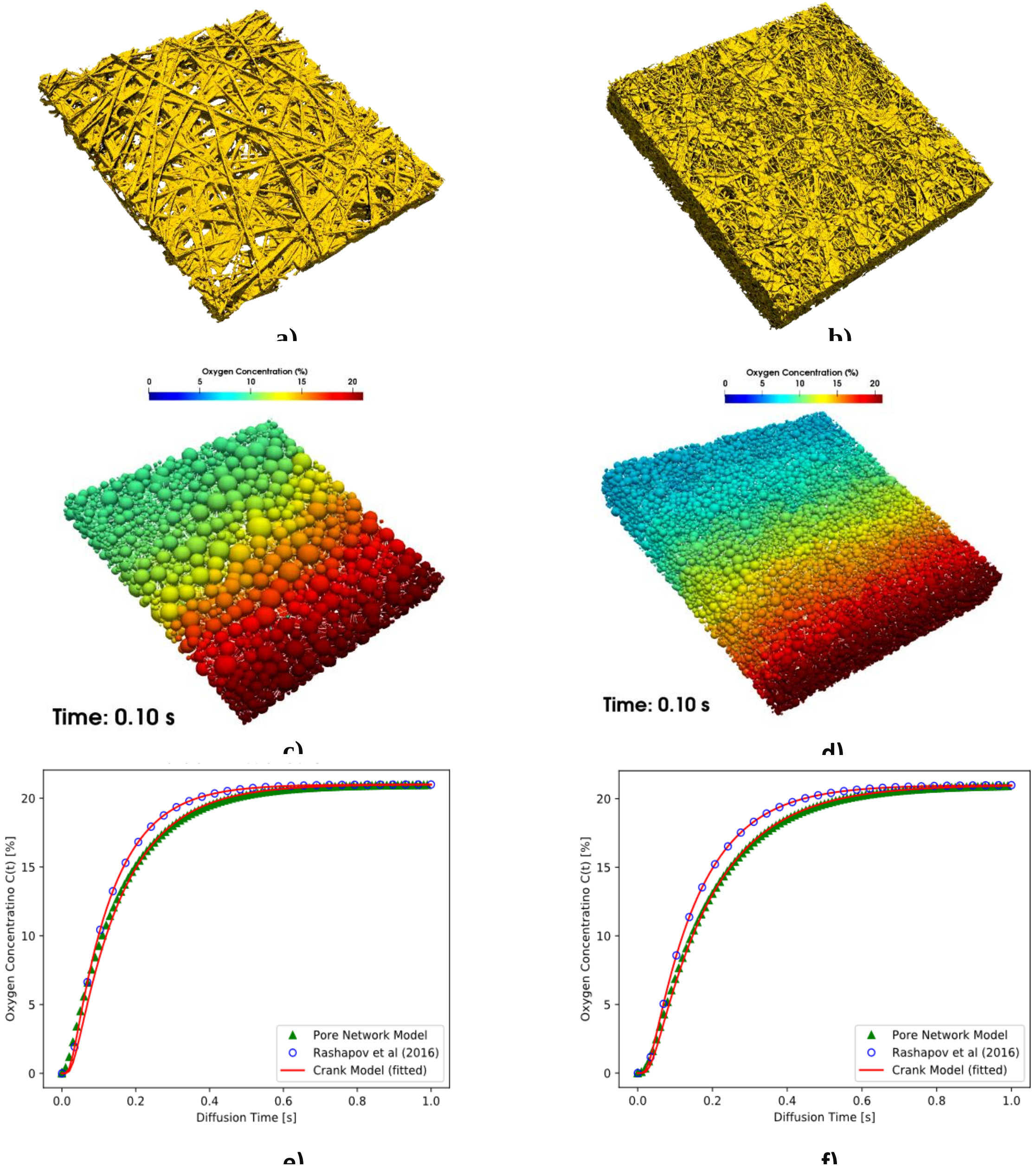

Figure 2.9 a) XCT image of SGL25A b) XCT image of Toray120A, c) and d) Extracted pore network transient Fickian simulation at 0.1s for SGL25A and Toray120A respectively, e) and f) Validation of pore network model with experimental data

2.4.3. Implementation of transient algorithm with source term

Along with unsteady transient transport process of species in lithium ion batteries, reactions play a significant role in overall performance of cell. So, implementation of source or sink terms is also needed in the mass and charge balance to simulate coupled transport and reaction kinetics processes. In order to add source terms in equation (2.17), (2.18), (2.19) the reaction terms need to be linearized. For power law kinetics mentioned in equation (2.21) the linearization of reaction equation gives two linear terms as shown in equation (2.22):

$$r = kc^{n} \tag{2.21}$$

$$r = S1 \times c + S2 \tag{2.22}$$

where

$$S1 = knc^{n-1} \tag{2.23}$$

$$S2 = k(1-n)c^{n} \tag{2.24}$$

The generalized solution for implicit finite difference scheme can be written by using equation (2.15) and (2.16)as follows:

$$\mathbf{B}.\mathrm{C}^{\mathrm{t+\Delta t}} = \mathrm{C}^{\mathrm{t}} + \Delta t\, r \tag{2.25}$$

Once the source terms are linearized, they are added in $\boldsymbol{B}$ and C^{t} matrix in equation (2.25). For example, if label 5 and 8 are reaction pores then $S1$ term is subtracted in diagonal of $\boldsymbol{B}$ matrix and $S2$ is added in C^{t} at 5th and 8th row of both matrices. The resulting $\boldsymbol{B}$ and C^{t} matrix can now be represented as follows whereas the validation of Fickian diffusion algorithm with source terms can be seen in Chapter 2 and Chapter 6.

$$\boldsymbol{B} = \begin{bmatrix} 1 & 0 & 0 & 0 & 0 & 0 & 0 & 0 & 0 \\ -r_{10} & 1+r_{10}+r_{12}+r_{14} & -r_{12} & 0 & -r_{14} & 0 & 0 & 0 & 0 \\ 0 & -r_{12} & 1+r_{12}+r_{25} & 0 & 0 & -r_{25} & 0 & 0 & 0 \\ -r_{30} & 0 & 0 & 1+r_{30}+r_{34}+r_{36} & -r_{34} & 0 & -r_{36} & 0 & 0 \\ 0 & -r_{41} & 0 & -r_{43} & 1+r_{41}+r_{43}+r_{45}+r_{47} & -r_{45} & 0 & -r_{47} & 0 \\ 0 & 0 & -r_{52} & 0 & -r_{54} & 1+r_{52}+r_{54}+r_{58} - \Delta\boldsymbol{t}(\boldsymbol{S1}) & 0 & 0 & -r_{58} \\ 0 & 0 & 0 & -r_{63} & 0 & 0 & 1+r_{63}+r_{67} & -r_{67} & 0 \\ 0 & 0 & 0 & 0 & -r_{74} & 0 & -r_{76} & 1+r_{74}+r_{76}+r_{78} & -r_{78} \\ 0 & 0 & 0 & 0 & 0 & -r_{85} & 0 & -r_{87} & 1+r_{85}+r_{87} - \Delta\boldsymbol{t}(\boldsymbol{S1}) \end{bmatrix}$$

$$C^t = \begin{bmatrix} c_0 \\ c_1 \\ c_2 \\ c_3 \\ c_4 \\ c_5 + \Delta \boldsymbol{t}(\boldsymbol{S2}) \\ c_6 \\ c_7 \\ c_8 + \Delta \boldsymbol{t}(\boldsymbol{S2}) \end{bmatrix}^t$$

2.5. Application of Pore Network Modelling in Energy Storage Devices

The application of pore network modelling in electrochemical energy storage devices has mostly focused on fuel cells [34,35] and redox flow batteries [36]. There are very few studies that discuss lithium-ion batteries because of complex Multiphysics involved during charging and discharging process [20]. In the following sections, some significant applications are highlighted for different energy storage devices.

2.5.1. Pore network modelling of Fuel Cells

Pore network modelling in fuel cells can be dived into two classes. The first class deals with only transport properties estimation while second analyses the structural performance relationship of fuel cells. For transport process modelling, Nam and Kaviany [37] in 2003 presented the first pore network model on gas diffusion layer of polymer electrolyte membrane fuel cell. They calculated effective diffusivity of partially saturated GDL and fed it into multiphase continuum model to analyze fuel cell performance. The fibrous GDL structure was created by making the analogy of porous structure with a stack of screens. The random sizes of screen opening were adjusted by changing the horizontal spacing while keeping vertical spacing fixed. Their GDL porous structure can be regarded as regular cubic network with random adjustment of horizontal spacing. The effect of porosity and saturation dependence were correlated and used as inputs in a continuum-based model to calculate fuel cell performance. Their network model does not include any pore size structural information like volume, diameter and length of throats etc.

Gostick et al [38] studied the PEMFC gas diffusion layer by considering its structure as regular cubic packing. The model was used to describe pore-scale distribution of water and gas inside GDL during drainage conditions by using invasion percolation algorithm. The transport properties like relative permeability and effective diffusivity of water and gas phase were calculated using series resistor theory. The developed pore network model was also used to estimate limiting current of PEMFC during operating conditions which requires only solving the diffusion equation, so no kinetics or coupled multiphysics was required.

The PEMFC pore network modelling based on irregular networks has also been performed by many authors. Luo et al [39] used the topologically equivalent network model to represent two types of GDL microstructures. Their structurally equivalent network provided a framework to design GDL with improved water management. The results showed the dependence of GDL morphology on water transport characteristics, which supported the need for developing GDL structure-performance relationships. Similarly, Gostick [40] also generated pore network of fibrous GDL in PEMFC using Delaunay and Voronoi tessellations. The voids were represented by Delaunay network while Voronoi tessellations were used to represent the fibre structure of GDL. The model gave useful insights for in-plane and through-plane relative effective diffusivity in partial water-saturated GDL.

Starting with the work of Aghighi et al [41] polarization behavior of fuel cells was included in pnms along with modelling usual transport processes. Aghighi et al developed pore network model of the full fuel cell electrode assembly, that included the multiphysics. This included transport of gas inside GDL and catalyst layer, transport of protons in catalyst layer and membrane and water percolation in MEA assembly of PEMFC, and Butler-Volmer kinetics to describe the reaction rates. This study shows the true potential of pore network modelling of an electrochemical system. It was found that presence of water inside GDL not only affect the concentration polarization but also changes ohmic polarization as protons generated at anode side will require to travel more distance to reach cathode active sites due to the presence of water inside GDL/CL. One limitation of this work was that simple cubic pore network model was used instead of topological equivalent networks which require many assumptions to represent void structure.

2.5.2. Pore network modelling of Redox Flow Batteries

Sadeghi et al [19] used PNMs to explore the impact electrode microstructure on the performance of hydrogen Bromine battery. The model's low computational cost enabled them to carry out a parametric sweep to search for optimum electrode structure. It was found that aligning the electrode fibres in the flow direction increases the performance to a certain extent after which diminishing results were obtained. The algorithm framework was kept general so that it can be applied on any sort of electrochemical species.

Lambarodo et al [17] implemented a transient Multiphysics pore network model in X-ray tomography image of porous carbon paper electrode. Transport phenomena and reaction kinetics of vanadium flow battery were analyzed at the microscale level. The developed algorithm was used to simulate convective and diffusive transport and showed restrictive flow in certain local portion of the electrode. Later, migration and reaction kinetics were coupled with connective/diffusive transport electrochemical transport phenomena was studied in porous structure. The developed algorithm only used a single core in workstation to perform simulation and highlights the computational benefit of pore network modelling while simulating complex transport phenomena.

2.5.3. Pore network modelling of lithium-Ion Batteries

Pore network modelling in lithium-ion batteries has not been attempted. There are a couple of PNM studies of other components such as the membrane, but none look at the intercalation reaction occurring at the cathode electrode.

Lagadec et al [42] focused on the transport through the membrane separator, which is porous. Their study investigated the drawback of using volume averaged approach to simulate Li-Ion battery separator and highlighted the influence of void space connectivity on Li-Ion transport through the separator. Their work investigated the concentration variation of Li ions in different structures of separators. It was found that the variation of concentration depends on pore space connectivity. This connectivity of void space was calculated based on topological and network analysis. Despite being about Li-ion batteries, this study included no electrochemical analysis of the electrode and was limited to basic diffusion through the porous separator. Nonetheless, it shows the importance that pore structure has in these devices.

Toreyev A. et al [3] used pore network model to study the electrochemical performance of lithium-oxygen battery. The model included the microstructural effects to study the discharge curves of four different domains of the porous domain of lithium-oxygen cathode. It was found that due to structural variation or different interconnectivity of pores that discharge capacity curve shows slight variations. The drawback of the model was that it was applied to the porous phase while solid phase properties were assumed constant. In a lithium-ion battery, however, we have three phases i.e electrolyte, solid and carbon binder domain and transport process in each domain effects overall performance so a pore network model that includes all three phases is inevitable.

Chapter 3 Dual Network Extraction for Multiphase Transport

3.1. Preface

The paper extended the capability of current network extraction algorithm to dual-phase extraction that includes solid and void phase and interconnections between these phases. The developed algorithm also includes a technique to estimate the cross-sectional area of throats accurately and hence improve the accuracy of calculations.

3.2. Overview

Image processing of 3D tomographic images to extract structural information of porous materials has become extremely important in porous media research with the commoditization of x-ray tomography equipment to the lab scale. Extracted pore networks from images using image analysis techniques enable transport properties calculation for bigger domains at a low computational cost, allowing pore-scale investigation of porous media over meaningful macroscopic length scales. The present study reports a pore network extraction algorithm to simultaneously extract void and solid networks from tomographic images of porous materials using simple image analysis techniques. Crucially, it includes connectivity and geometrical information of both void and solid phases as well as the interlinking of these phases with each other. Validation was obtained on networks extracted from simple cubic and random sphere packings over a range of porosities. The effective diffusivity in the void phase and thermal conductivity in the solid phase was then calculated and found to agree well with direct numerical simulation results on the images, as well as a range of experimental data. One important outcome of this work was a novel and accurate means of calculating interfacial areas between grains and voids directly from digital images, which is critical to many phenomena where phase interactions occur. The efficient 'dual network' algorithm is written in PYTHON using open source tools and provides a new way to study critical processes that depend on transport in both void and solid phase such as catalytic reactors and electrochemical systems.

3.3. Introduction

Transport in porous media plays an essential part in many prominent applications such as oil recovery and aquifer management in naturally occurring rocks and soils [43], but also devices containing engineered porous media such as battery electrodes [35], filters [44], membranes [45] and catalyst particles [46]. Transport and reaction processes strongly depend on the void and solid structure. Two materials which have the same porosity can have drastically different transport and reaction rates because of differences in pore size, shape, and connectivity, etc [47]. An often overlooked or neglected aspect of porous media studies is the transport in the solid phase (i.e. heat and electrons), which is subject to the same performance-structure competition as the void phase. In applications such as battery electrodes and catalysts supports, the solid structure provides reactive surface area and transport pathways. Moreover, the void and solid phases also impact the transport and reaction processes in opposing phases, so designing optimized materials with enhanced performance requires a detailed study of both phases simultaneously.

Visualization has always been a vital tool in porous media analysis, from optical imaging of serial sections and 2D micromodels to modern tools such as FIB-SEM and X-ray tomography. High-resolution X-ray tomography has become the standard platform to understand the internal structure of porous media [48]. Most benchtop X-ray tomography scanners can produce 3D images of resolution as good as 1-µm voxel, while the recent generation can give a resolution of 20 nm [49]. The deluge of information provided by X-ray tomography [50] has highlighted the need for efficient means of extracting valuable information from these tomograms given the massive size of the image, often over 1 billion elements (1000^3 voxels).

Quantitative image analysis can be used to obtain a range of information about void structure, such as the two-point correlation function [51] or chord-length distribution [52]. However, finding the connectivity of void space from a porous material is one of the most important aspects since it is directly related to the most important properties: tortuosity and permeability. Researchers have tried to extract this structural information from tomographic images using many different algorithms. A network extraction algorithm that is widely used in pore network extraction is maximal ball algorithm by [27], then adopted and developed by [53]. Their method was time-consuming and tended to predict high coordination number. To prevent this issue, [54] made a two-step algorithm that defines voids and throats through a clustering process. In addition to these network extraction algorithms, [55] developed 3DMA software using medial axis transform. [56] developed similar network extraction algorithms based on skeletonization techniques to characterize solid data. [47] performed void space partitioning based on morphological skeletonization by using fully parallel thinning algorithm. They investigated stochastically reconstructed porous media images and shows that identical porosities exhibit a significant difference in geometry and connectivity. Pore network extraction using watershed segmentation was originally investigated by [29] and [30].[31] used this approach to extract network for low porosity sandstone. [57] applied watershed segmentation on the gas diffusion layer of proton exchange membrane fuel cell. Recently, [28] refined the watershed method for high porosity material by extracting a sub-network of the over-segmented watershed (SNOW). This algorithm succeeds by removing several types of spurious peaks in the distance transform that lead to over-segmentation in the watershed step, especially in high porosity images. Importantly, the SNOW algorithm was shown to generally work for both high and low porosity materials.

The commonality in these algorithms is that all of them have been tuned to find void phase structure since transport in the void is of general interest, while solid phase is often ignored. In many chemical engineering applications, however, electron and heat transport through the solid phase is equally important, which demands the need for solid structure extraction. In principle, any existing algorithm can be applied to the solid phase by inverting the image [58], but this would only yield two independent networks, while the interactions and interconnections with void phase have significant importance. Heat can be transferred between the void and solid, and reactions happen at the void-solid interface. Consider a reaction-diffusion process in porous catalyst particles. Here solid-phase requires consideration as the kinetics of chemical reaction is highly dependent on temperature, so modelling heat transfer within the particles is vital [59]. Figure 3.1 shows a catalytic fixed bed reactor along with different transport phenomena taking place inside, including convective heat and mass transfer in void phase region, mass diffusion due to the concentration gradient between void and solid phase, reaction process occurring at the interface of catalyst particle and intraparticle heat conduction between catalyst particles. Therefore, in order to get maximum benefit from network modelling, it is necessary to extract a dual network that incorporates both void and solid phases as well as the local interconnection of these phases.

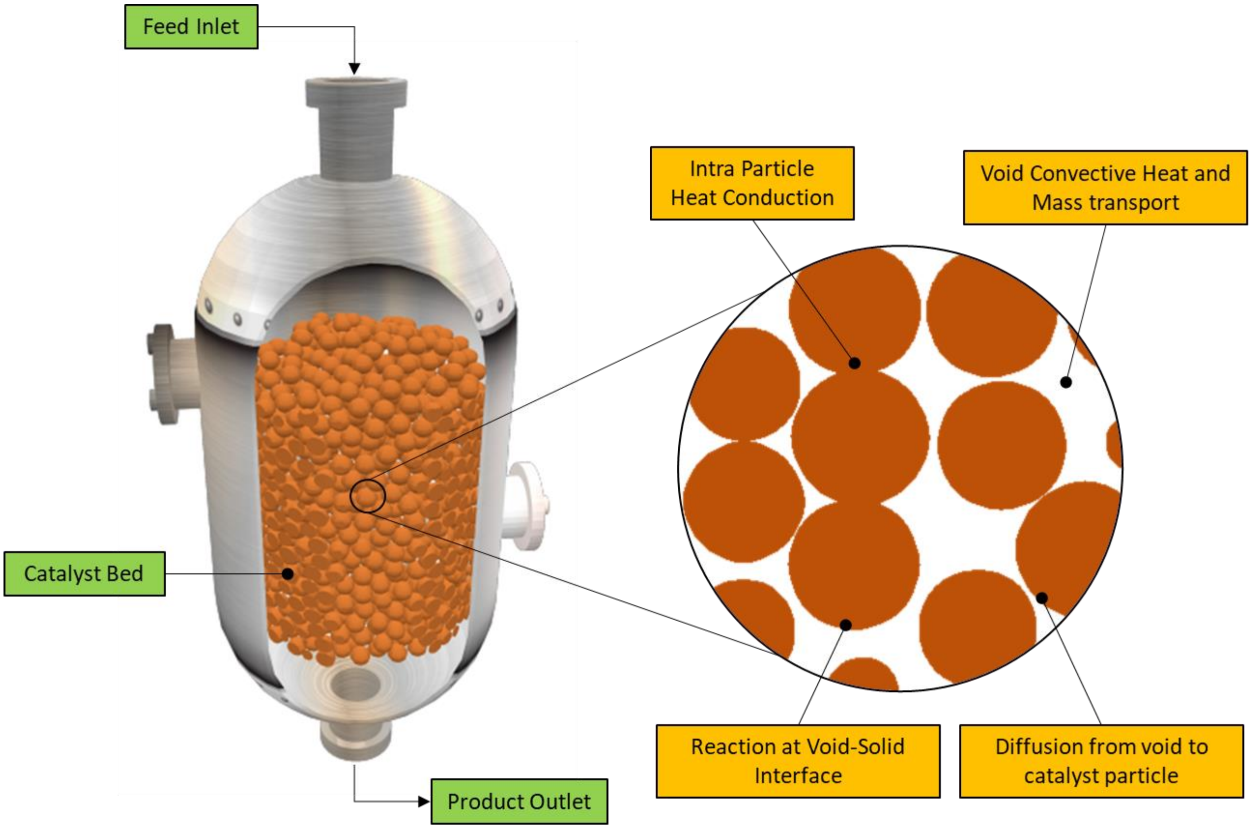

Figure 3.1 Importance of transport phenomena and reaction processes in solid and void phases of catalytic fixed bed reactor

In this work, we present an algorithm that simultaneously extracts both the solid and void network from a tomographic image, including the interlinking of these phases with each other, to create a 'dual network'. The presented algorithm is an extension of the recently published SNOW algorithm [28], which was selected based on its low computational cost, applicability to high porosity materials, and ability to reliably extract the key structural features. The presented algorithm provides a new avenue for pore network modelling, opening the way to investigate many critical processes that require transport in both void and solid phase such as reaction-diffusion in catalyst particles and charging and discharging dynamics of porous electrodes in batteries. To the best of our knowledge, this is first dual network extraction effort in pore network modelling.

3.4. Algorithm

The watershed segmentation algorithm has many benefits for network extraction, but most appealingly it matches the intuitive definition of what constitutes a pore body, as discussed by [60] in his recent monograph. In the present study the watershed approach was used, building on the recently published report of the SNOW extraction algorithm (Sub-Network of an Over-segmented Watershed) [28]. The general procedure to extract only void network is outlined in Figure 3.2a. The algorithm works in two steps. This first is the partitioning of the image into discrete regions for each pore, and the second is to analyze the regions in the partitioned image to extract geometrical and topological information for the network. The procedure starts with a binary image of 0’s as solid phase and 1’s as void phase, then performs distance transform on it the void. A maximum filter is applied to find peaks which will become the basins of the watershed transform, but first any extraneous peaks are trimmed which is the key to avoiding over-segmentation. In the next step, marker-based watershed segmentation is performed on the remaining peaks to get void regions as catchment basins in the network. Lastly, the segmented image is scanned one region at a time to extract the network information such as pore size and neighbours. The details of all relevant geometrical properties can be found in our previous work [28].

3.4.1. Detailed Description of Dual Network Extraction Algorithm

The dual network extraction algorithm presented here was developed on the premise that the analysis of the partitioned image is agnostic to whether the regions are void, solid or either. As such, the basic outline of the algorithm is that the void and solid phases are partitioned using the normal approach described above, but the two images are combined into a single composite image prior to extracting the geometrical and topological information for each region. A post-processing step determines which regions belong to each phase and labels them accordingly. The present incarnation of the algorithm also includes the ability to include boundary nodes on the image prior to extraction, so they appear in the resultant network. The basic framework of the dual network is shown in Figure 3.2b and discussed in following sections. The open-source code is implemented in PYTHON using the SCIPY stack [61] and is provided as part of PoreSpy [62].

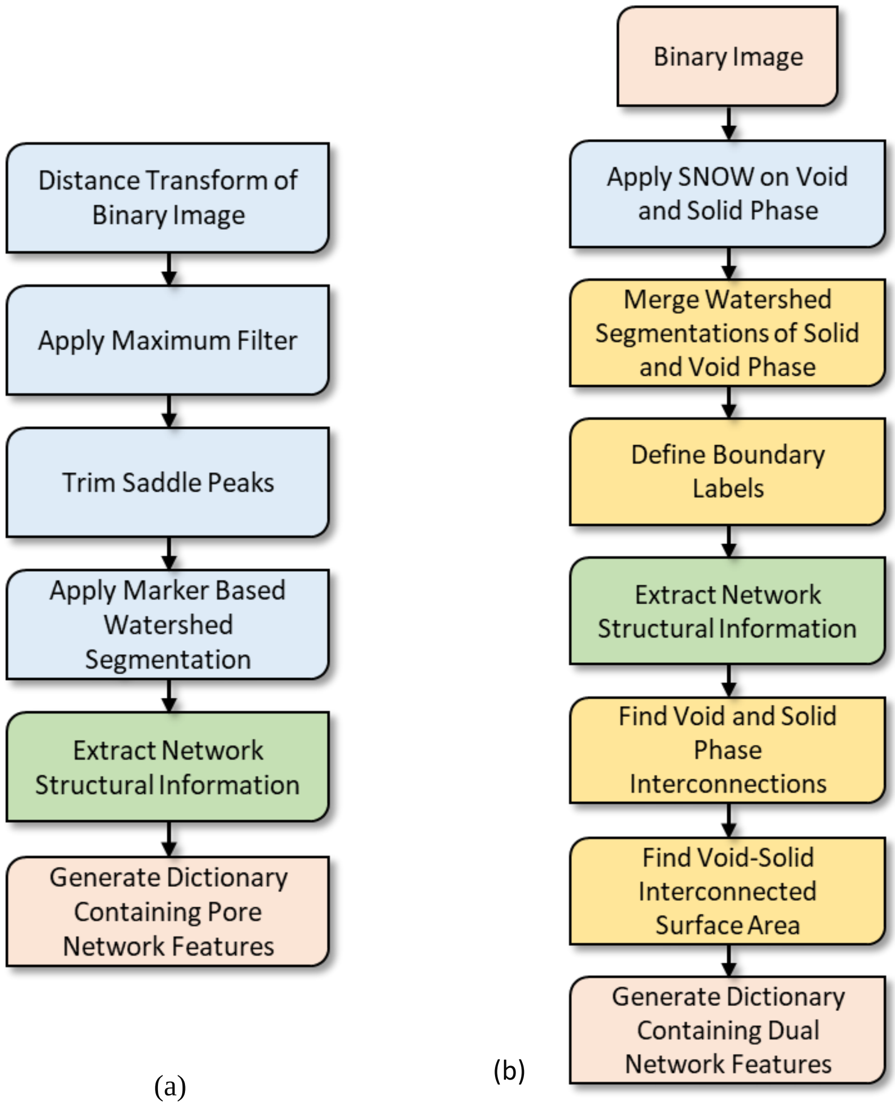

Figure 3.2 a) Void network extraction algorithm using subnetwork of over segmented watershed (SNOW) algorithm b) Dual network extraction algorithm

3.4.2. Applying SNOW algorithm

Given a binary image with 1’s indicating void and 0’s for solid, the SNOW algorithm is applied to both void and solid-phase separately giving the result shown in Figure 3.3. While applying SNOW on the solid phase, the image was inverted to represent solid by 1’s and void by 0’s. The SCIKIT-IMAGE package was used to apply marker-based watershed segmentation [63].

3.4.3. Merging watershed segmentation

Next, the void and solid-phase segmentations are merged into a single composite image. The largest value of peak label in the void segmentation was added to solid-phase segmentation in order to differentiate between void and solid properties labels (thus void regions are labelled $1 \rightarrow N_V$, and solid regions $N_V + 1 \rightarrow N_V + N_S = N_T$). Figure 3.3(a,b) represents watershed segmentation applied on void and solid-phase independently. In Figure 3.3c the merged watershed segmentation of void and solid phases is shown with void labelled as 1,2,3,4 and 5 and solid labelled as 6,7, and 8. Similarly, the distance transforms of void and solid phase were also merged in order to provide combined distance transform; this is necessary so the sizes of the underlying region, such as diameter of an inscribed sphere, can be found during the network extraction phase.

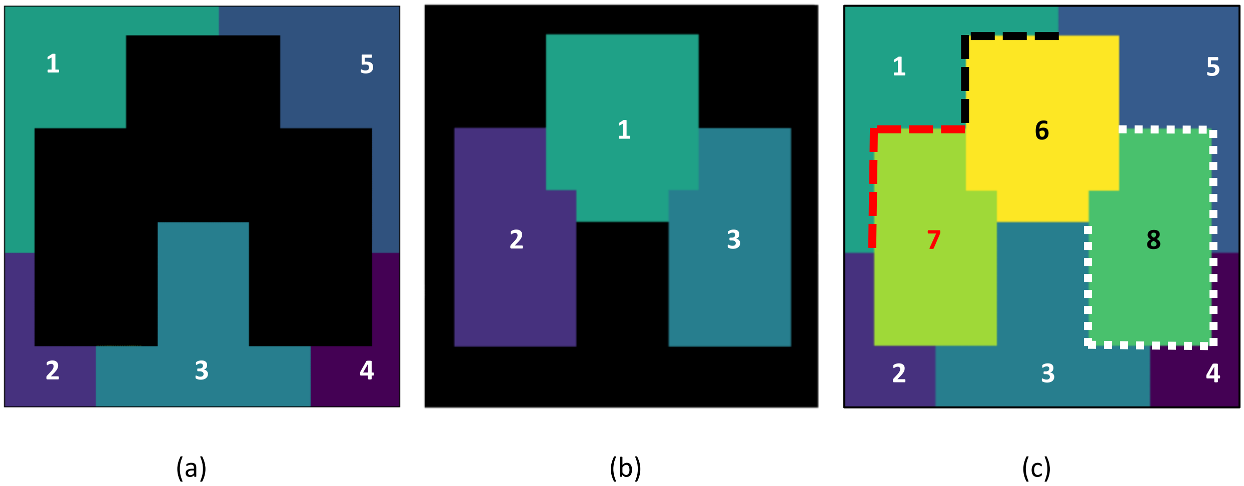

(a) (b) (c)

Figure 3.3 a) Void phase labeled watershed segmentation, b) Solid phase labeled watershed segmentation c) Merged watershed segmentation of pore and solid regions

3.4.4. Defining boundary nodes

Defining boundary conditions in an irregular pore network is a challenging task because of rough surfaces at boundary faces. This problem gets more complicated in the dual network as now two phases with different voids and solid orientation exist at the boundary of the network. These irregular faces lead to many difficulties during simulation of transport process. Firstly, domain length and area cannot be calculated precisely, which can either over- or underestimate the effective property calculation (e.g. effective diffusivity) which depend on domain area and length. It is also difficult to calculate flux as there is no definitive control surface which complicates simulation of transport process. This issue was discussed in previous work [40] for randomly generated Voronoi and Delaunay network. In that work, a method was developed to create flat boundary faces by mirroring the base points outside the working domain and trimming outside pores after tessellation. A similar approach was applied in the present work:

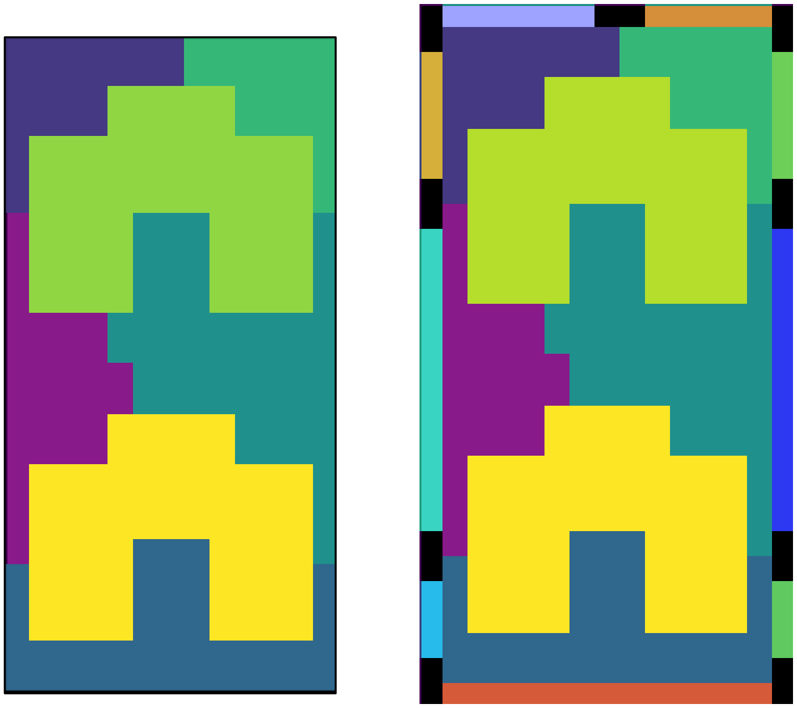

(a) (b)

Figure 3.4 a) Image segmentation without boundary nodes, b) Image segmentation with boundary nodes showing dead zones in black color to avoid boundary nodes interconnections

The merged watershed segmentation containing both phases was padded with a layer of extra voxels. This process copied the void and solid labels at the surface of the image and formed an external layer of void and solid labels. Subsequently, all labels on the padded surface were given new values (starting at $N_T + 1$ where N_T was the total number of labels in the merged watershed image) so that they could be extracted as separate nodes in the dual network. In the next step, interconnections of boundary nodes with each other were prevented by using the SCIPY-NDIMAGE *find_boundaries* function. This created a boolean mask of boundary faces identifying boundary nodes interconnections location which was then labelled as 0's to represent a border region between boundary labels. Note that any values in the watershed image labelled 0 will be ignored during the network extraction step. Figure 3.4 shows segmented images with and without specifying boundary nodes. The black colour on the boundary surfaces represents fictitious solid regions to avoid interconnections of boundary nodes, while coloured regions show boundary nodes interconnected with adjacent void/solid inside the segmented image.

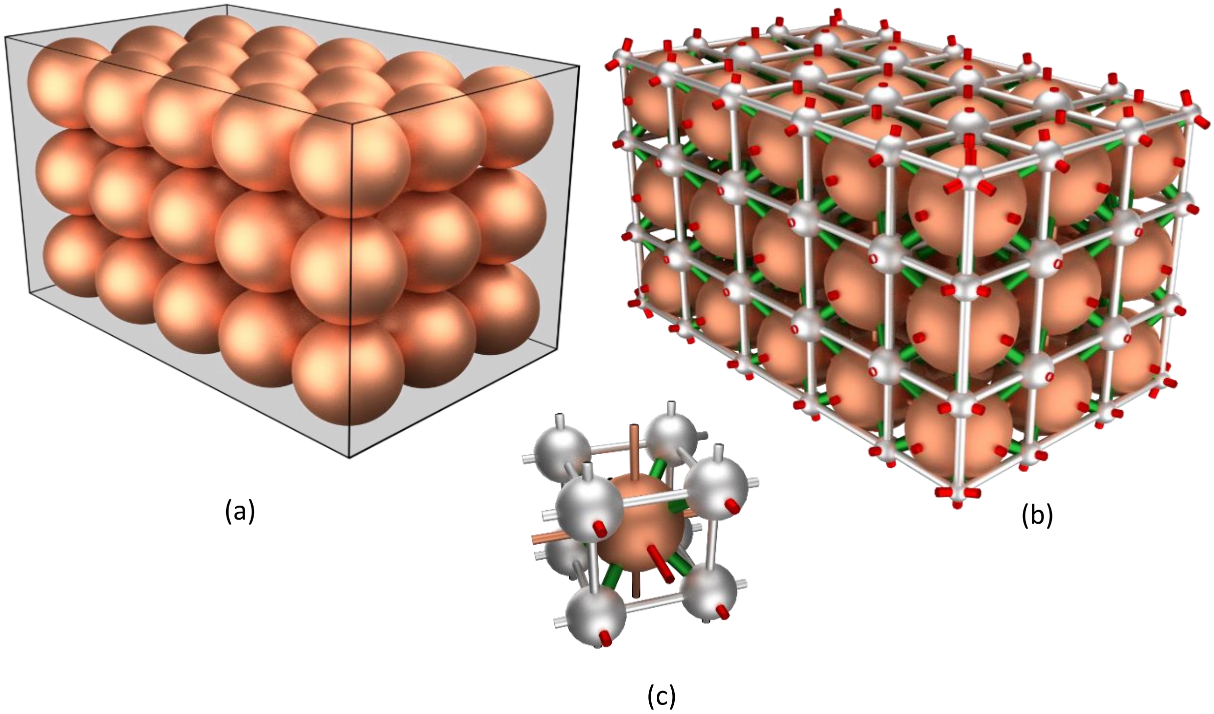

Figure 3.5 a) Simple cub packing of 45 spheres in a (148,148,249) voxels container, b) Extracted dual network of cubic packing with void and solid-phase represented in silver and copper colour respectively while interconnection and boundary nodes are represented in silver and copper colour respectively while interconnection and boundary nodes are represented in green and red colour respectively, c) Unit cell of extract dual network for better illustration

3.4.5. Extracting Dual Network Information

After defining boundary nodes, the merged watershed segmentation and distance transform were scanned to extract the geometrical and topological properties of the void, solid and throats. The process treats all labelled segments as voids (or more generally nodes) so calculates the connectivity and geometrical properties of the solid phase by treating it as a void phase. To measure size, area, volume etc. each labelled region is isolated from its neighbouring region and the number of voxels associated with the specific geometrical property are analyzed. Similarly, throat properties are calculated by scanning neighbouring regions and analyzing the size of the boundary defined by shared voxels. This process is outlined in detail in previous work [28].

3.4.6. Labelling Phases and Finding Interconnections

The output of the previous step contains no information about which nodes or connections belong to which phase, so a post-processing procedure was necessary. The data from the previous step was stored in arrays of length N_T or N_C, where N_T is the total number of nodes in the network (solid + void) and N_C is the total number of connections. Because of the way the regions were numbered it is known that the first N_V entries correspond to voids and the remaining N_S values the solid phase. Similarly, the connections can be identified by the node numbers being connected. The options are void-to-void, solid-to-solid, and void-to-solid. All this information is stored by labelling each entry accordingly.

3.4.7. Finding interface surface area

The interfacial area between two nodes is one of the most critical aspects of the geometric analysis, but it is difficult to determine. Two neighbouring regions share a common set of voxels, so analyzing the shape of this common set can provide a wealth of information about the connection between the regions, such as interfacial surface area. For instance, as shown in Figure 3.3c void 1 is connected with grains 6 and 7, and grain 8 shares surface area with voids labelled as 3,4 and 5. Although simple in principle, surface areas are difficult to determine in a voxel image [64]. In the present work, this was accomplished using the marching cubes algorithm [65] but a few considerations were necessary. The marching-cubes algorithm operates by constructing a tetrahedral mesh around the perimeter of the region, and the surface area can be found from the triangular facets on the exterior surface. The quality of the mesh is dependent on the input image, however. For instance, a Boolean image will result in a mesh that conforms exactly to the voxel facets so the area estimate will be no better than just counting cube faces. An image with blurry boundaries allows the algorithm to construct a smoother mesh, so in the present work, each region was subjected to mean filter with a 3^3 cubic structuring element prior to analysis. It was confirmed on images of single spheres at different resolutions that this approach yields the correct value within 5% as long as diameter of voids or solids is more than 10 voxels. The other consideration is that the marching cubes algorithm does not work well on 2D (or nearly 2D) regions, so the interface between two regions cannot be analyzed directly. A simple and elegant workaround was developed here, whereby the surface area of region A and region B were found independently, and then for A and B combined. The interfacial surface area between A and B can be found from the sum of the individual areas, minus the combined area then halved.

3.5. Generation of Sphere Packings for Validation

For validation of the extracted networks, images of simple cubic and random sphere packings of monosized spheres were used. These were generated using open-source discrete element software Yade [66]. For simple cubic packing *regularOrtho* function was used to get 45 equal sized spheres of 50 voxels diameter (∅) in a rectangular chamber of 148 × 148 × 249 voxels size in x, y and z coordinates respectively. As shown in Figure 3.5a. This packing was used for direct validation discussed in detail in algorithm validation section. The SpherePack function was used to generate random spheres packing in a 525^3 voxels container. After generation, periodic compression was performed with PerilsoCompressor to stuff as many spheres as possible. The final porosity of random sphere packing after compression was 0.44.

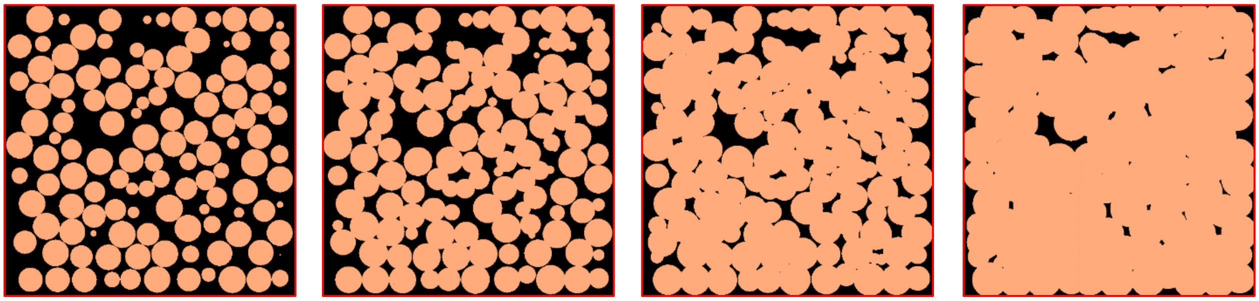

∅ = 50 mm
ε = 44.2%

∅ = 54 mm
ε = 31.5%

∅ = 60 mm
ε = 16.2%

∅ = 68 mm
ε = 5.1%

Figure 3.6 Random sphere packing densification by increasing particle radius from 50 mm to 68 mm

It was of interest to validate the extracted networks on packings of various porosities, but sphere packings always have a porosity near 0.44, so instead, the spheres were dilated to create overlaps. This overlapping was analogous to a sintering effect in solid phase which gradually decreased the porosity (ε) from 0.44 to 0.052 [67]. 2D slices of four different porosities packings are shown in Figure 3.6. It can be seen clearly that some spheres at low porosity overlap into each other and form a cluster of solid-phase while many voids are isolated from neighbouring voids in void phase. Overall eight different porosity packings were used to investigate the performance of the dual network across a range of scenarios.

3.6. Results and Validation

3.6.1. Validation on Periodic Packings

3.6.1.1. Topology and Geometry Structure

The present algorithm was validated directly by comparing the extracted network to that of simple packing which has known coordination number and size distribution in both void and solid phase. For this purpose, regular orthogonal cubic packing of porosity 0.487 and sphere diameter of 50 voxels was chosen, as shown in Figure 3.5a. It has a nominal coordination number of 6 (surface, edge and corner sites have less) and known solid radius of 25 voxels. The total size of the container in x, y and z coordinates was 148 × 148 × 249 voxels respectively. After applying the present algorithm, the resulting extracted network can be seen in Figure 3.5b. The solid, voids and throats of individual phases are shown in copper and silver colour respectively. Similarly, interconnections between solid and void phase, as well as, boundary throats are shown in green and red colour respectively. For better visualization, a representative unit cell of cubic packing is shown in Figure 3.5c. Each solid is connected with 6 neighbouring spheres and 8 neighbouring voids with a total coordination number of 14. The diameter of solids and their respective throats in the extracted network is approximately 50 voxels and 7 voxels. For void phase, the coordination number depends on the location of a void in the image. Each void is connected with 6 neighbouring voids, as well as interconnected with solid spheres depending upon its location (surface, edge, or corner). The total coordination number in void phase is 7, 8, 10 and 14 at corners, edges, faces and inside body respectively.

Unlike solid phase, the size of voids and throats depends on their location in the extracted network. The diameter is highest inside body of cubic packing while it is lowest at edges and corners, which occurs because the walls of the container are implicitly included in the extraction. Table 3.1 shows a comparison of extracted and theoretical values of the packing obtained by summing up voxels of the image for a particular property. These results show a very good match of the structural properties in both void and solid phase of simple cubic packing.

Table 3.1 Comparison between extracted and theoretically calculated properties of simple cubic packings

Value	Extracted				Theoretical			
Porosity (%)	46.9				46.9			
Solids - N_s	45				45			
Voids - N_v	96				96			
Solids throats - N_{ts}	96				96			
Void throats - N_{tv}	224				224			
Soid-Void Interconnections -N_{int}	360				360			
Boundary Nodes - N_b	206				206			
Coordination Number (Solid Phase)	14				14			
Spheres Diameter (voxels)	49.6				50			
Spheres throat diameter (voxels)	8				8			
	B	**F**	**E**	**C**	**B**	**F**	**E**	**C**
Coordination Number (Void Phase)	14	10	8	7	14	10	8	7
Voids Diameter (voxels)	48	38	29	23	49	-	-	-
Voids throat diameter (voxels)	23	16	10	10	22	-	9.8	9.26

**B,F,E,C are abbrevation of Body, Faces, Edges and Corner respectively*

Table 3.2 Comparison of SNOW DUAL and analytical values of interfacial area in void and solid phase

Phase	**SNOW DUAL Interfacial Area**	**Analytical Solution Interfacial Area**	**Relative Error (%)**
Void Structure:			
Interphase	7396.0	7171	3.04
Intraphase	2760	2937	3.29
Total	10156	10108	0.47
Solid Grain:			
Interphase	7806.17	7851	0.57
Intraphase	3.0	3.0	0
Total	7809.17	7854	0.57

3.6.1.2. Interfacial Surface Area

Validation of interfacial surface area of individual solid and void for irregular geometries is a challenging task because there is no analytical solution to compare against given the random nature of the particle contacts. In the present study, validation is performed on a regular cubic packing, which allows the exact determination of interfacial area of solid and void from analytical expressions. Figure 3.7 shows the structure of a single void connected with solid grains in a regular cubic packing. The area associated with neighbouring solids and voids is represented as green and yellow coloured faces respectively. The total surface area of the void structure and solid grain calculated analytically are given in Table 3.2. The surface area of the void structure was calculated analytically according to:

$$A_s = 24r^2 - 2\pi r^2 - 6\pi r_{st}^2 - 24r_{st}.w \tag{3.1}$$

where r is the radius of spherical grain, r_{st} is the radius of the throat between two spherical grains and w is the width of the corner in the void structure. The value of $r_{st} = 6$ and $w = 2$ voxels were obtained by visual examination of the 3D image.

Equation (3.2) was then used to find the surface area A_c of region 1 associated with region 2. The intraphase and interphase parts are determined by checking if the two connecting regions belong to same or different phase respectively

$$A_c = \frac{1}{2}(A_{region\ 1} + A_{region\ 2} - A_{combined}) \tag{3.2}$$

where $A_{region\ 1}$ and $A_{region\ 2}$ is the surface area of region 1 and region 2 respectively while A_c is the surface area of region 1 associated with region 2 as shown in Figure 3.7c.

Also shown in Table 3.2 are the interfacial surface areas between the void and solid as determined using the image analysis technique outlined in Section 3.4.7. There is less than 5% error between these two values, indicating a good agreement between SNOW DUAL estimated area and analytical solution.

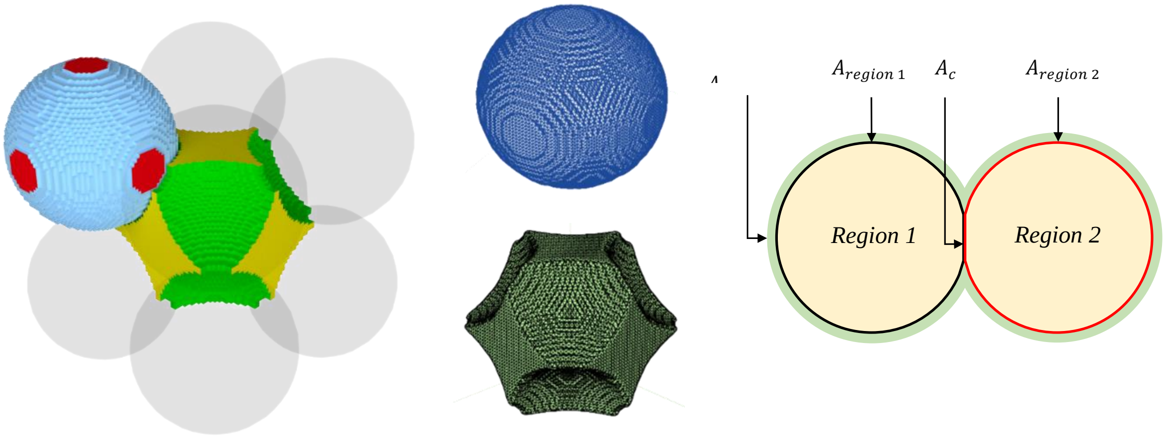

a) b) c)

Figure 3.7 a) Interfacial surface area of one solid grain and void in regular cubic packing. Interphase and intraphase interfacial area are shown in cyan and red color for solid and green and yellow color in void respectively. b) Vertex diagram of same solid and void after applying marching cube algorithm in SNOW DUAL. c) Intraphase and interphase surface area calculation schematic using marching cube algorithm

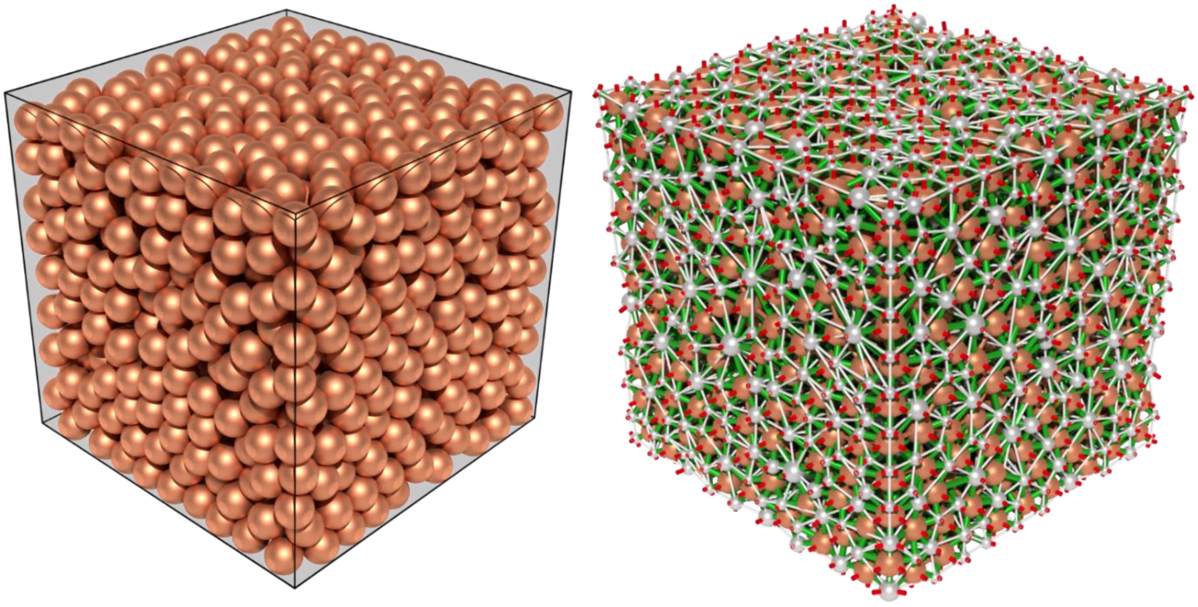

(a) (b)

Figure 3.8 a) Random sphere packing of 1250 spherical particles of 50 voxels diameter in a 5253 voxel container, b) Extracted dual network of random sphere packing with void and solid phase reprsented in silver and copper color respectvely while interconnection and boundary nodes are represented in green and red color respectvely

3.6.2. Validation on Random Packings: Transport Properties

Although direct validation on a well-defined periodic packing gives insight into the accuracy of the extracted dual network, more realistic packings are of interest. A validation study was carried out by simulating the effective thermal and diffusive conductivity in the solid and void phase respectively of a random packing of spheres and comparing the results with other modelling methods and published experimental data where available. A dual network was extracted from a 525^3 voxel image containing 1250 spheres as shown in Figure 3.8. The initial diameter of all spheres was 50 voxels, but they were morphologically opened using a 1 voxel spherical structuring element to ensure they fully touched each other and avoid digitization artefacts. The void and solid phases are shown in silver and copper while interconnections and boundary throats are coloured green and red respectively.

In order to estimate steady-state thermal conductivity in the solid phase network, heat flow into and out of each solid sphere was calculated. For each sphere, *i*, in the solid phase network, thermal equilibrium requires that:

$$\sum_{i=1}^{n} J_i = 0 \tag{3.3}$$

where *J* is heat flow in *W* and *n* is the number of contacts of the sphere *i.e* number of thermal conductance elements connected with sphere *i* under consideration. In this simulation, steady-state Fourier's law was applied to calculate heat flow in the solid phase. Heat conduction between sphere *i* at temperature T_i and sphere *j* at temperature T_j can be calculated according to the following discretized form of the 1-dimensional Fourier equation:

$$\dot{J}_{i,j} = kA\frac{(T_i - T_j)}{\Delta x} = g_{i,j}(T_i - T_j) \tag{3.4}$$

where *k* is bulk thermal conductivity of the material in *W/m.K*. *A* is the area of cross-section in m^2 between sphere *i* and *j* and *x (m)* is the length between sphere *i* centroid to sphere *j* centroid. These terms can be represented as thermal conductance $g_{i,j}$. Moreover, since the area between sphere *i* and *j* is not uniform, the term $g_{i,j}$ with an interconnected throat *k* is calculated using linear resistor theory for resistors in series:

$$\frac{1}{g_{i,j}} = \frac{1}{g_{i,k}} + \frac{1}{g_k} + \frac{1}{g_{k,j}} \tag{3.5}$$

For the thermal conductance calculation, the connections between spheres resulted in a situation where g_k in equation (3.5) was 0 since the length of the neck between the two grains was 0. Even as the grains were dilated to decrease the porosity, and new connections where made, the neck (or throat) had 0 lengths. This is illustrated in Figure 3.9a.

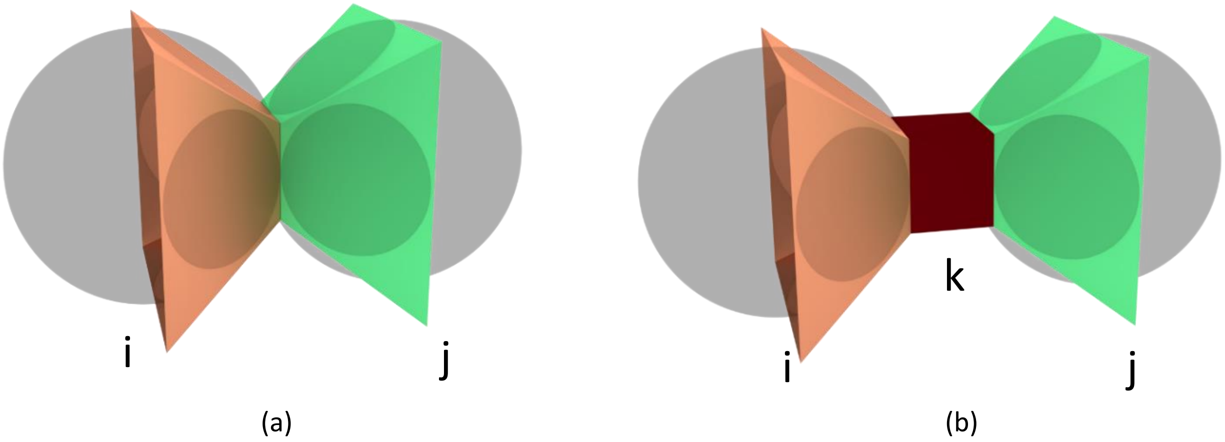

Figure 3.9 a) Square Pyramid model without throats for overlapping spherical particles (Case 1), b) Square pyramid model with throats for void phase of random sphere packing (Case 2)

The thermal conductance in each sphere was determined by accounting for the nonuniform area of the sphere cross-section by representing the sphere with an equal volume pyramid as shown in Figure 3.9a. Although an exact geometrical model could be obtained for the spherical cross-section of the grains, this was not possible for the void space as discussed below, so the same pyramidal approximation was applied to both phases. The resulting expression for solid-phase thermal conductance in sphere *i* can be calculated by the following expression:

$$g_{i,k} = 4k\frac{r_i r_k}{\Delta x_i} \tag{3.6}$$

where r_i and r_k are radii of sphere *i* and constriction, respectively, while Δx_i is the length of sphere *i* from the centroid to constriction boundary.

An analogous approach was adopted to estimate steady-state effective diffusivity in the void phase. Therefore, 1-D Fick's laws for steady-state and diffusive conductance between void *i* and *j* can be represented in discretized form as equation (3.7), (3.8) and (3.9) respectively.

$$\sum_{i=1}^{n} q_i = 0 \tag{3.7}$$

$$\dot{q}_{i,j} = \frac{DA}{RT}\frac{(p_i - p_j)}{\Delta x} = d_{i,j}(p_i - p_j) \tag{3.8}$$

$$\frac{1}{d_{i,j}} = \frac{1}{d_{i,k}} + \frac{1}{d_k} + \frac{1}{d_{k,j}} \tag{3.9}$$

where *q* is the molar flow rate in *mol/s*. *p* is the partial pressure of the gas in the respective void. *D* is bulk diffusion coefficient of specie in void phase, *d* is diffusive conductance in void phase, *T* is the temperature of voids and *R* is universal gas constant.

Unlike the solid phase, the pores in the void phases did not form overlapping spheres but instead consisted of inscribed spheres at the interstices of the grains, and throats connecting them. This is shown in Figure 3.9b. The same pyramidal shape was applied to the void pores as for the solid grains, resulting in the following formula:

$$d_{i,k} = \frac{4D}{RT}\frac{r_i r_k}{\Delta x_i} \tag{3.10}$$

The total conductance between pores also included a throat section. The value of d_k in equation 7 was found by assuming the throat has a square cross-sectional area that did not vary, thus:

$$d_k = \frac{4D}{RT}\frac{r_k^2}{L} \tag{3.11}$$

where L is the length of the throat.

Boundary conditions in both solid and void phase were applied to opposite faces of the extracted network in the x-direction. The temperature of the solid at x = 0 and x = 525 μm was set to 373K and 298 K respectively. The spherical particle was assumed to be of copper material with intrinsic thermal conductivity k of 385 *W/m.K*. Similarly, the partial pressure oxygen in void phase at $x = 0$ and $x = 525$ μm was fixed to 21 *kPa* and 0 *kPa* respectively and oxygen bulk diffusivity D of 2.09×10^{-5} m^2/s in air was assumed in void phase.

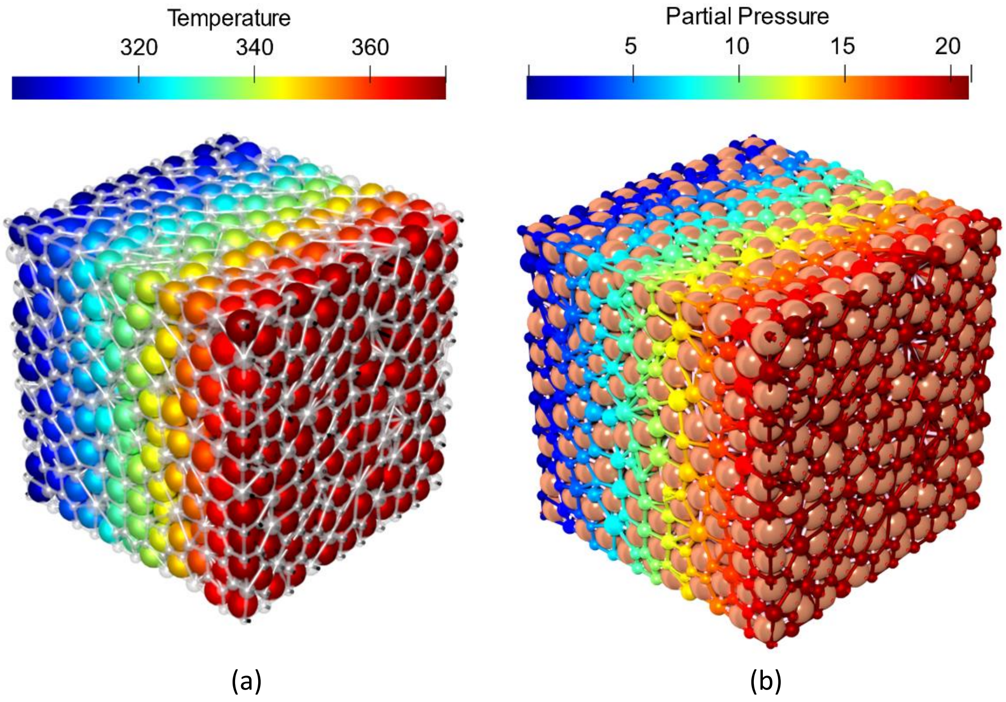

Figure 3.10 a) 1-dimensional steady state thermal conduction in solid phase, b) 1-dimensional steady state diffusion void phase

The simulation performed in solid and void phase on the extracted dual network using OpenPNM [32] open-source software, yielding the temperature and concentration profiles shown in Figure 3.10. Moreover, algorithm validation was performed by comparing the results of effective transport properties with Lattice Boltzmann and random walker simulation [68], which are described in more detail in the following sections.

3.6.2.1. Lattice-Boltzmann Simulation

Lattice-Boltzmann calculations were performed using the open-source software Palabos to model steady-state conduction and diffusion in solid and void phase. D3Q7 lattice was used as descriptor and Bhatnagar–Gross–Krook (BGK) collision model was used to describe dynamics of heat and mass flow. A tolerance value of 10^{-4} was selected to calculate normalized values of effective transport properties. The simulation was carried out along all three axes of 525^3 mm^3 image and an average value of the effective property is reported. The main benefit of the LBM solver is that the voxel image is used directly as the computational mesh, thereby avoid the time consuming and error prone process of creating a mesh suitable for FEM solvers.

3.6.2.2. Random Walker Simulation

Discrete-time random walker method was used to find the tortuosity of solid and void phase in random sphere packing by calculating the mean square displacement of 1×10^5 random walkers. The method and its open-source, parallelized implementation are described in detail in a recent work [69] The probability density function p(x,t) of a walker at location x and time t [70] can be described according to the equation (3.12):

$$p(x,t) = \frac{1}{\sqrt{4\pi Dt}} \exp\left(\frac{-x^2}{4Dt}\right) \tag{3.12}$$

The variance of equation 9 is termed as mean square displacement (MSD) and can be written as:

$$MSD = \int_{-\infty}^{\infty} x^2 p(x,t)dx \tag{3.13}$$

The mean square displacement (MSD) of a simple walker with unbiased movement is assumed to follow a Gaussian distribution and the gradient of MSD when plotted over a period of time gives tortusity factor τ^{-1}. The tortuosity τ calculated is used to find effective coefficient in sphere packing of known void fraction ε according to [71]:

$$\frac{D_{eff}}{D} = \frac{\varepsilon}{\tau} \tag{3.14}$$

The normalized effective conductivity as a function of solid fraction for SNOW DUAL, Lattice Boltzmann and random walker simulation is shown in Figure 3.11a. The results of [72,73] for 304L stainless steel spherical powder is also reported. From the graph, it can be seen that SNOW dual results agree well with other modelling approaches for spherical particles. The normalized value of effective conductivity increases with increasing solid fraction. This agrees with equation (3.4) as at high solid fraction more area is exposed for heat conduction in the solid phase. Moreover, as tortuosity factor in equation (3.14) decreases with increasing solid fraction, effective conductivity value becomes higher at high solid fraction. Figure 3.11b shows the normalized effective diffusivity value against void fraction in spherical particles. The results obtained by [67] and [74] are also reported, which agree well with SNOW Dual simulation. The effective diffusivity values decrease with increasing sintering effect in the solid phase. At 0.045 solid volume fraction, almost no diffusion takes place in void phase because of high tortuosity and small exposed area available for diffusion.

3.6.3. Resolution Study

In order to check the robustness of dual extraction, a resolution study was conducted. Random sphere packings were produced as described above and spheres of diameter 54 voxels were inserted into the image containing 525^3 voxels. The resolution of the image was changed by decreasing or increasing the number of voxels using nearest neighbour interpolation. The resulting values of effective conductivity and effective diffusivity in solid and void phase as the resolution was varied from 0.5 to 1.7 of the original image is shown in Figure 3.12. At low resolution, the relative error in both void and solid phase at resolution 0.5 was 3.8% and 16% respectively which is acceptable to get preliminary results with low computational cost and low memory (RAM) usage while simulating bigger porous material domains which is currently not feasible in direct numerical simulation and Lattice-Boltzmann modelling. It should be noted that robust behaviour towards resolution is not expected to translate to noisy images. Obtaining clean and correct segmentations from greyscale images remains a challenge [75].

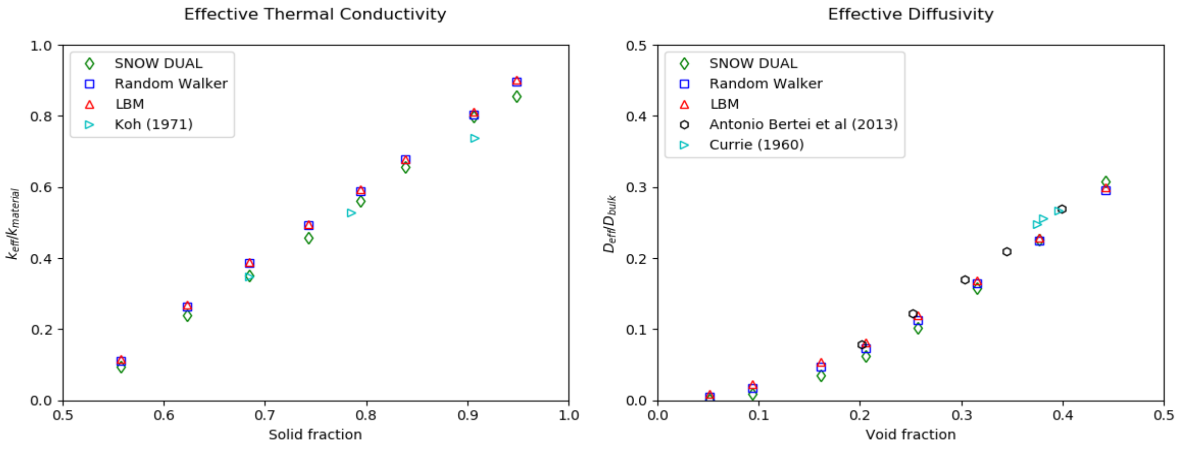

(a)

(b)

Figure 3.11 a) Normalized thermal conductivity in solid phase, b) Normalized diffusivity in void phase of random sphere packing at different porosities

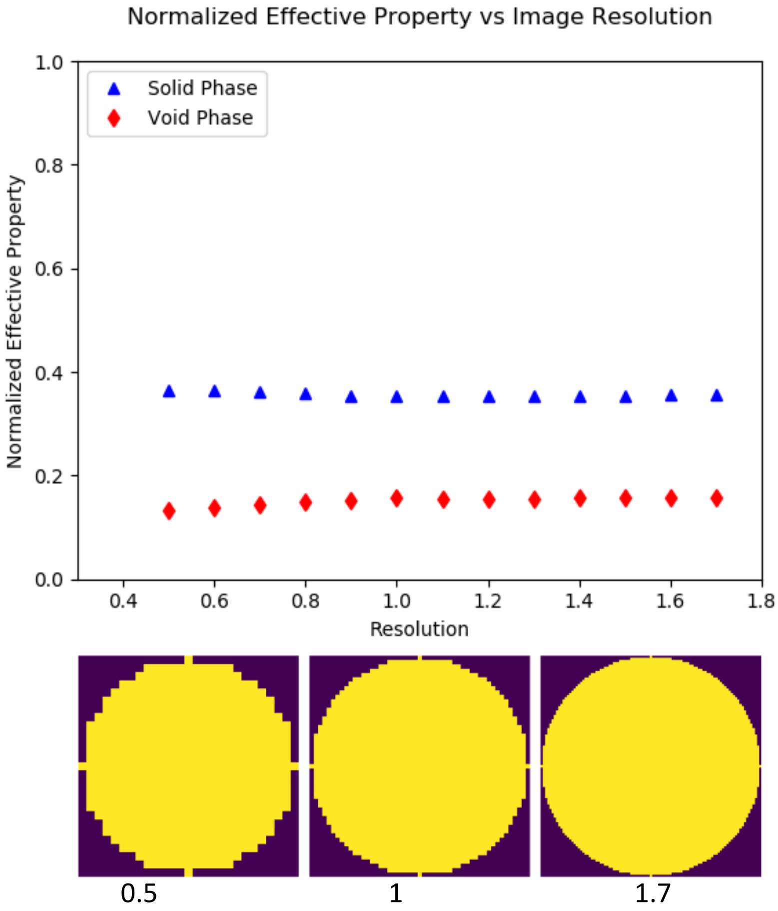

Figure 3.12 Resolution study of random sphere packing in both void and solid phase.

3.6.4. Performance

Modern X-ray tomography scanners can produce images at a high resolution of 1000^3 voxels or more, so any network extraction algorithm must process this large amount of data in a realistic time. Moreover, the algorithm should run on easily accessible computational resources such as desktop computers or laptops rather than depending on supercomputers. Good computational performance was ensured while developing dual network extraction algorithm by using Numpy array operations and the scipy.ndimage library for image analysis. Figure 3.13 shows algorithm run time as a function of image size. Five image sizes, from 200^3 to 1000^3 voxels, were used to analyze performance. The total function time includes the time required to apply SNOW algorithm on both pore and solid phase, as well as processing time of SNOW_DUAL. For 600^3 voxels image, it takes 37 minutes to extract whole dual network, which is passable though speed-ups would be welcome.

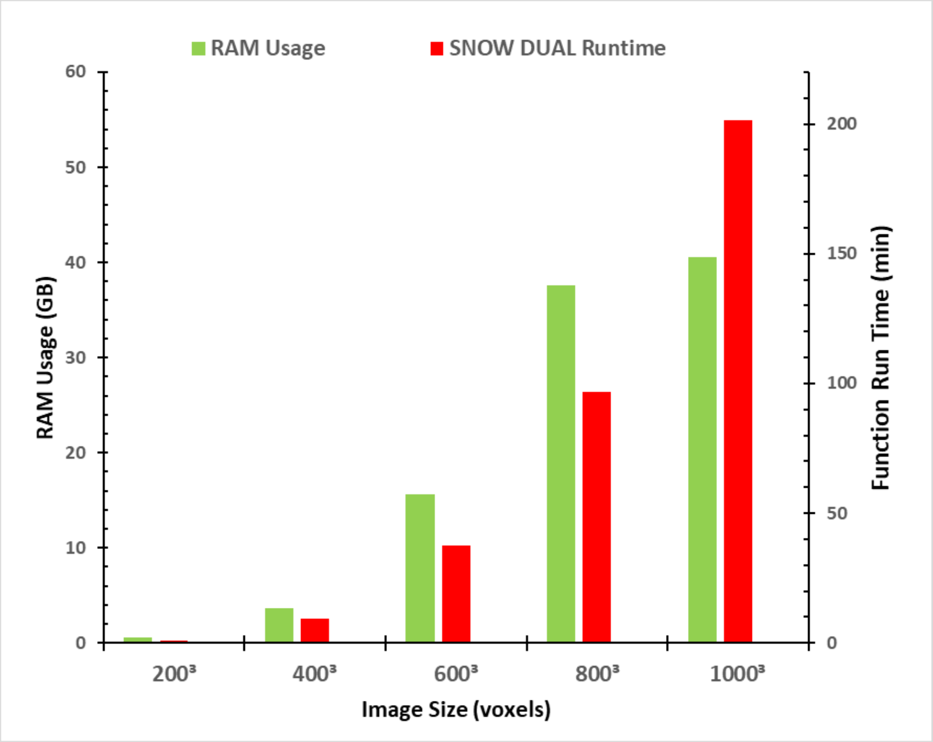

Figure 3.13 Algorithm run time and memory usage for different image sizes. Simulations were performed on a Dell Precision T5610 Workstation with a Xeon E5-2665 Processor (16 cores) and 128GB of RAM.

Although the dual network extraction algorithm is light in terms of computational resources, the watershed segmentation step in SNOW algorithm requires large RAM for images with billions of voxels. Figure 3.13 shows the amount of RAM usage in SNOW algorithm for different image sizes. It can be seen that until 400^3 voxels image size, the RAM usage is below 16 GB, indicating easy implementation of code on a normal workstation. An image having a size of 1000^3 voxels requires approximately 50 GB RAM and network extraction time is close to 3 hours. This huge amount of RAM usage can be avoided by using a low-resolution image which is discussed in the Resolution Study section above. The watershed step is also computationally slow, comprising the majority of the extraction time. A recent article by [76] compares performance of different watershed implementations, although preliminary testing suggests that the difference disappear when images approach 1000^3 and have hundreds of basins.

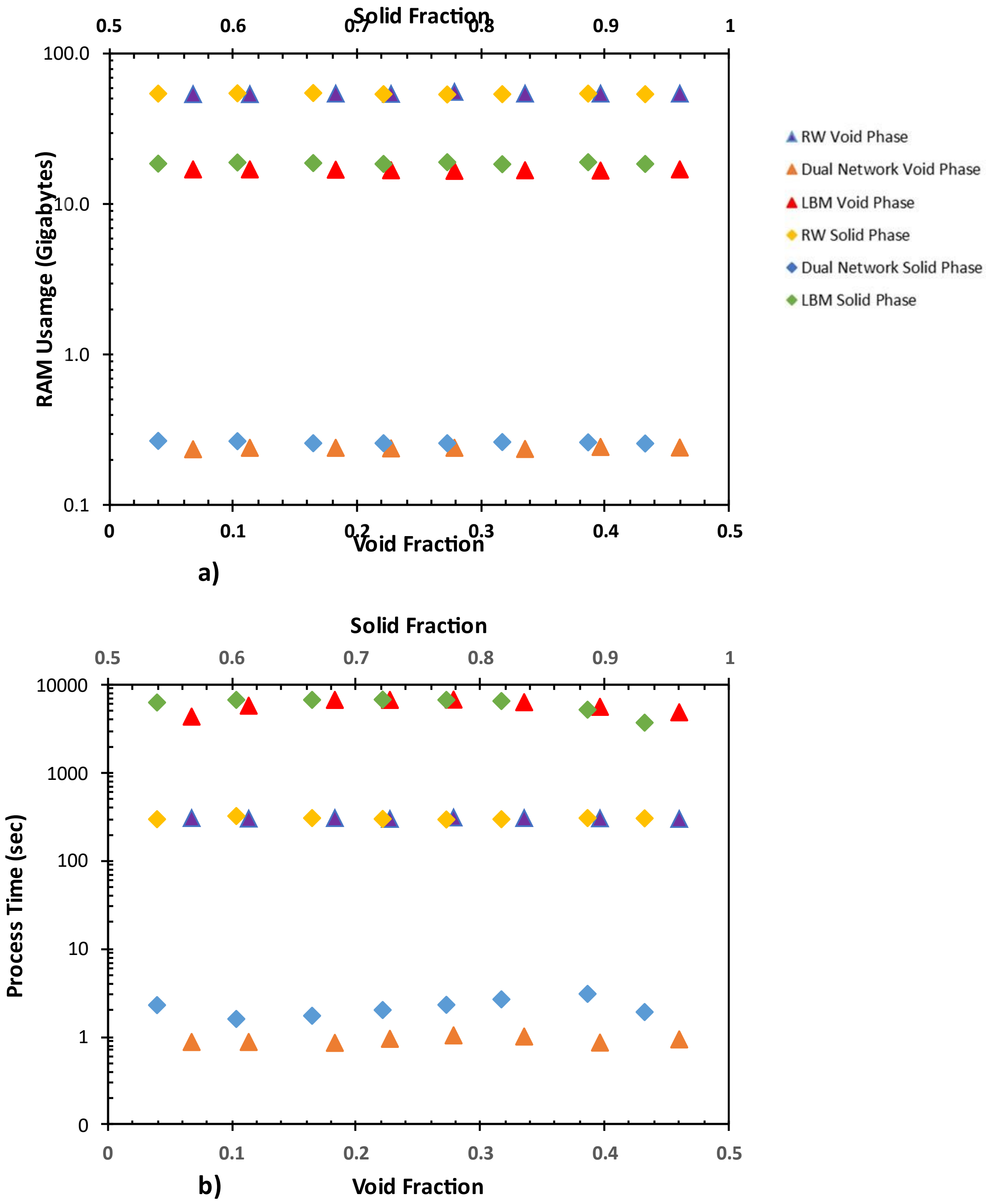

Figure 3.14 a) CPU processing time comparison b) RAM usage comparison in RW, Dual Network and LBM in void and solid phase of random sphere packing

The computational performance of extracted dual network was also compared with random walker simulation and Lattice boltzmann simulation. The CPU processing time and RAM usage for all 8 samples in random sphere packings were measured on both solid and void phases to find effective thermal conductivity and diffusivity respectively. The computational study was performed on a Dell Precision T5500 workstation with Xeon X5650 processor (12 Cores) and 72 GB of RAM. For the LBM and RW simulations, 10 cores were used, while for the PNM simulations all Python UMFPACK module was used which utilizes all 12 cores of CPU. The results are shown in Figure 3.14. It can be seen that the dual network is relatively more efficient in comparison with random walker and Lattice Boltzmann simulation.

3.7. Conclusions

The motivation behind the current study was to investigate the transport processes in porous materials at the microstructural level. The transport of reactive species in the void phase and heat and/or electrons in the solid phase is of central interest to chemical engineers wishing to design or analyze porous catalyst structures, but traditional porous media research in pore network modelling field almost exclusively neglects transport in the solid phase. The advent of x-ray tomographic imaging can provide extremely detailed images of the internal structures, but computer modelling remains prohibitively expensive. The present work utilized an alternative approach to modelling transport at the pore-scale by extracting network models from the images, thereby achieving an extremely significant model-order reduction. The novelty of the present approach is that both void and solid-phase networks are extracted simultaneously, including the interconnections between the phases. Additionally, an elegant and accurate scheme for determining the interfacial surface area was developed, which is not straightforward for voxelized images.

The model output was validated directly on simple cubic packing with known connectivity and void/solid sizes, and the network properties were in good agreement with the known structural information of simple cubic packing. Simulations were also performed on random sphere packing by calculating effective conductivity and diffusivity in solid and void phase respectively. The results were compared with LBM, random walker and experimental data and were found in good agreement across a wide range of porosities. The current work opens a new avenue to study void-solid interactions in reactive systems where microstructural features such as connectivity, interfacial contact, and heterogeneity play a significant role in performance.

Chapter 4 Structure-Performance Relationship of Lithium-Ion Battery

4.1. Preface

This study extends the capability of dual-phase extraction algorithm to N phase network extraction algorithm. This was essential as most of the lithium-ion cathode material usually consists of three phases such as active material, electrolyte phase and carbon and binder domain phase. The developed algorithm extracts these three phases from fully resolved X-ray tomography image of NMC-811 cathode. The algorithm performance was tested by simulating reaction-diffusion and reaction conduction transport processes and results were compared with direct numerical simulations. Moreover, the importance of including carbon binder phases was highlighted to understand performance structure relationship.

4.2. Overview

Pore-scale simulations of Li-ion battery electrodes were conducted using both pore-network modelling and direct numerical simulation. Ternary tomographic images of NMC811 cathodes were obtained and used to create the pore-scale computational domains. A novel network extraction method was developed to manage the extraction of N-phase networks which was used to extract all three phases of NMC-811 electrode along with their interconnections Pore network results compared favourably with direct numerical simulations (DNS) in terms of effective transport properties of each phase but were obtained in significantly less time. Simulations were then conducted with combined diffusion-reaction to simulate the limiting current behaviour. It was found that when considering only ion and electron transport, the electrode structure could support current densities about 300 times higher than experimentally observed values. Additional case studies were conducted to illustrate the necessity of ternary images which allow separate consideration of carbon binder domain and active material. The results showed a 24.4% decrease in current density when the carbon binder was treated as a separate phase compared to lumping the CBD and active material into a single phase**.** The impact of nanoporosity in the carbon binder phase was also explored and found to enhance the reaction rate by 16.8% compared to solid binder. In addition, the developed technique used 1.8 times larger domain volume than DNS which opens up the possibility of modelling much larger tomographic data sets, enabling representative areas of typically inhomogeneous battery electrodes to be modelled accurately, and proposes a solution to the conflicting needs of high-resolution imaging and large volumes for image-based modelling. For the first time, three-phase pore network modelling of battery electrodes has been demonstrated and evaluated, opening the path towards a new modelling framework for lithium-ion batteries.

4.3. Introduction

Lithium-Ion batteries (LIBs) are the most widely used electrochemical energy storage devices for portable electronics and electric vehicles (EVs). They offer a good trade-off in terms of energy density, cycle life, low weight, low self-discharge, and high power-density and these advantageous properties have driven the revolution in portable electronics and, more recently, EVs. However, there is a continual need to improve their realizable energy density, enhance their safety, and extend their lifetime [77] as well as to reduce their cost. The positive electrodes in LIBs are composed of active material (typically a layered metal oxide material) into which Li-ion intercalation/deintercalation occurs, and a conductive additive (usually carbon black) that improves electrical conductivity throughout the electrode. These two components are combined with a binder into a porous structure and the remaining void space is filled with Li^+ containing electrolyte, creating a 3-phase porous electrode. Understanding the multiple, coupled transport processes within this porous electrode is key to enhancing the transport of Li ions and electrons, and hence to optimise design of LIBs.

To this end, mathematical modelling techniques are an essential tool to guide the experimental development of novel electrode structures. On one end of the spectrum lie the volume-averaged models originally developed by Newman et al [12]. The majority of these efforts focus on developing more accurate and/or complete continuum scale models that require less computational cost [78,79]. The drawback of continuum models is that they only include the microstructural properties of porous electrodes through volume-averaged correlations, but it is well known that structure plays a key role in the species transport and ultimately device performance. At the other end of the spectrum, models based on direct numerical simulation (DNS) techniques using 3D images of the electrode microstructure as the computational mesh have been developed [80–82]. The relatively recent growth in application of 3D X-ray tomographic imaging to electrochemical devices and DNS models [83,84] have greatly enhanced the understanding of transport processes occurring inside the electrode by capturing details of the geometrical structure; however, DNS is computationally expensive. To incorporate all the necessary multiphysics, as well as transient behaviour, is prohibitively demanding, such that even simulating the entire thickness of the cathode (on the order of 30-75 µm) is an unreasonable task. Thus only DNS of small sections of electrode can be undertaken, and these are not large enough to be representative of a real LIB. There is thus a strong need to develop a modelling framework that can bridge the gap between the continuum models of entire devices and DNS on subsections of microstructure, but at low computational expense while maintaining the crucial microstructural details. To meet this objective, pore network models are a promising option.

Briefly, pore network modelling is a method whereby a porous material is abstracted as a network of nodes and interconnections that represent pores and throats. It is possible using image processing to extract geometrical and topological details of porous media from a tomography image, then map this onto a network of interconnected nodes. Each node is a single unknown to be solved for, which approximates some of the pore-scale details of electrodes but allows simulation of large porous domains with very low computational cost as compared to DNS, with minimal difference in output (if the network extraction is performed correctly). Recently, pore network modelling has been used to model various electrochemical energy conversion and storage devices. For example, Aghighi et al [41] developed a pore network model to simulate a polymer electrolyte fuel cell (PEMFC) membrane electrode assembly. Aghighi et al [35] later extended this model to measure the effect of phase change in a PEMFC cathode. El Hannach et al [85] developed a pore network model to analyze water management and electrical performance of a PEMFC cathode catalyst layer. Their model discussed both pore and solid-phase networks and integrated different transport phenomena as well as electrochemical reactions in the catalyst layer. Similarly, pore network models have been utilized to study multiphysics transport processes in redox flow batteries (RFB)with the recent work of Sadeghi et al [86] that developed a multiphysics pore network model to study the impact of electrode microstructure in redox flow batteries (RFBs). Gayon Lombardo et al [87] used an X-ray CT image of an RFB electrode to extract a topological equivalent pore network and studied transient convective and diffusive transport processes. The results showed that concentration and pressure distribution inside electrodes greatly depends on microstructural properties. Some volume averaged approaches has also been adopted for fuel cell recently [88,89]. Together these recent works illustrate a new trend toward more complex multiphysics modelling using PNMs.

To date, no PNMs have been applied to Li-ion battery electrodes. Lagadec et al [90] have simulated the diffusion of Li-ions through a porous membrane separator, but they did not investigate the electrode structure or electrochemical reactions. Torayev et al [91] used a pore network model of Li-O_2 batteries. They applied their model to four different regions of the electrode and found that galvanostatic discharge curves in each region varied significantly in terms of capacity and overpotential, supporting the notion that pore interconnectivity and macroscopic arrangement play a crucial role in performance. In another article, Torayev et al [92] compared the ability of continuum and pore network modelling techniques to measure the impact of discharge performance and electrode pore size in Li-O_2 batteries. They concluded that continuum models should be used with caution as they are unable to capture important microstructural effects. It was also noteworthy that the pore network model, which explicitly captured pore interconnectivity, matched more closely with experimental data. These two studies were performed on the 3D reconstruction of super-P carbon electrodes with only pore and solid phase under consideration. Commercial lithium-ion battery cathode electrodes consist of three phases; electrolyte, carbon binder domain (CBD) and active material such as lithium iron phosphate ($LiFePO_4$, or LFP), lithium nickel manganese cobalt oxide ($LiNiMnCoO_2$, or NMC) and lithium cobalt oxide ($LiCoO_2$, or LCO). Treating the solid carbon binder and active material phases separately cannot only change the measured active surface area available, but also the transport mechanism of electrons in the solid phase because of significantly higher conductivity of the carbon binder domain (CBD) compared to active material [93]. Assuming carbon binder and active material as a single solid phase can significantly alter the electrochemical performance of the model. Hence, a computationally efficient pore network model is required that includes all the three phases with interphase and intraphase connectivity taken into consideration. As such, tomographic images containing all three phases are also essential.

The main objective of the present work is to apply and validate pore network modelling for studying the multiphysics involved in three-phase porous lithium-ion electrodes. A network extraction algorithm was developed to extract an arbitrary number of phases from X-ray CT images. The developed extraction algorithm is a continuation of previous work [94] and is used here to extract a topologically mapped network from a ternary tomogram of a $LiNi_{0.8}Mn_{0.1}Co_{0.1}O_2$ (NMC-811) electrode. The pore network was then used to simulate diffusion of lithium-ions in the electrolyte phase, conduction of electrons inactive material and carbon binder phase and the reaction of lithium and electrons at the interface of active material and electrolyte phases of the porous cathode. Finally, two case studies are performed to highlight the importance of simulating three-phase lithium-ion cathodes and the influence of the CBD nanopores on maximum attainable current density and voltage distribution. The presented pore network model provides a new avenue to study critical transport and reaction process in lithium-ion battery porous electrodes. To the best of our knowledge, this is the first network extraction of a lithium-ion battery cathode. The algorithm is written in python and is shared in the open-source project PoreSpy [95] available at https://github.com/PMEAL/porespy.

4.4. Methodology

4.4.1. Electrode Material

The material explored in this work is a nickel-rich lithium-ion cathode: $Li(Ni_{0.8}Mn_{0.1}Co_{0.1})O_2$ or NMC-811, and was fabricated by Targray (Kirkland QC) via printing from a slurry onto an aluminium current collector and subsequently calendared to reduce electrode porosity. Additional information provided by the supplier can be found within the supplementary material Table S4- 1 and Table S4- 2.

4.4.2. X-ray Computed Tomography

To prepare the sample for imaging, a disk ca. 1.0 mm in diameter was punched from the electrode sheet and fixed atop of a 1.0 mm diameter, 10.0 mm tall steel dowel using quick-set epoxy. A single X-ray tomogram was collected using a Versa micro-CT instrument (Zeiss Xradia 520 Versa, Carl Zeiss., CA, U.S.A.). Imaging was conducted with a source accelerating voltage of 80 kV at a power of 7 W using a tungsten target for an un-filtered, polychromatic emission with a characteristic peak at 58 keV. The tomogram was collected using 3201 radiograph projections, each with an exposure of 16 s. Geometric magnification coupled with a scintillator and 20× optical magnification resulted in an image with a pixel size of 400 nm. These radiographs were then reconstructed using standard cone-beam, filtered-back-projection (FBP) algorithms using commercial software (‘Reconstructor Scout-and-Scan’, Carl Zeiss., CA, U.S.A.). After reconstruction, the tomogram data was processed using a non-local means filter to improve the image quality for segmentation. The data was then cropped, the greyscale values were segmented according to cathode particles (NMC811), binder and void/pore space. Further information on the quality of the image contrast, filtering and segmentation can be found in the supplementary material Figure S4- 1, Figure S4- 2 and Figure S4- 3. All filtering, cropping and segmentation were achieved using Avizo Fire software (Avizo, Thermo Fisher Scientific, Waltham, Massachusetts, U.S.).

4.4.3. Pore Network Extraction

4.4.3.1. N-Phase Extraction Algorithm

The developed network extraction algorithm is based on the watershed segmentation technique which defines the porous regions and throat connectivity in a visually intuitive manner [60,96]. The current algorithm is based on our previously published SNOW algorithm (Sub-Network of an Over-segmented Watershed) [97] and its extension SNOW_DUAL algorithm [94]. The basic SNOW algorithm consists of two steps. Firstly, marker-based watershed segmentation is performed to partition the image into pore regions. Before applying this step, however, spurious markers are trimmed by applying several filters (Figure 4.1a) to avoid over-segmentation by the watershed filter. Secondly, the discretized regions are further analyzed one at a time to extract geometrical and topological properties of the pore regions. The basic steps involved in the network extraction process are shown in Figure 4.1a. The SNOW algorithm was later extended to the SNOW_DUAL algorithm to extract both solid and void phases and, crucially, the interlinking of these phases with each other to study transport and reaction mechanisms in catalyst packings. However, lithium-ion cathode material consists of three phases, namely active material, CBD and electrolyte phase. Therefore, the dual approach was generalized to an N-phase extraction algorithm which can be applied to any material with an arbitrary number of phases. The developed model can be used for any kind of commercial cathode material such as lithium iron phosphate ($LiFePO_4$) and lithium cobalt oxide ($LiCoO_2$) if 3-phase tomograms were provided – or indeed for any tomographic data set of N-segmented phases.

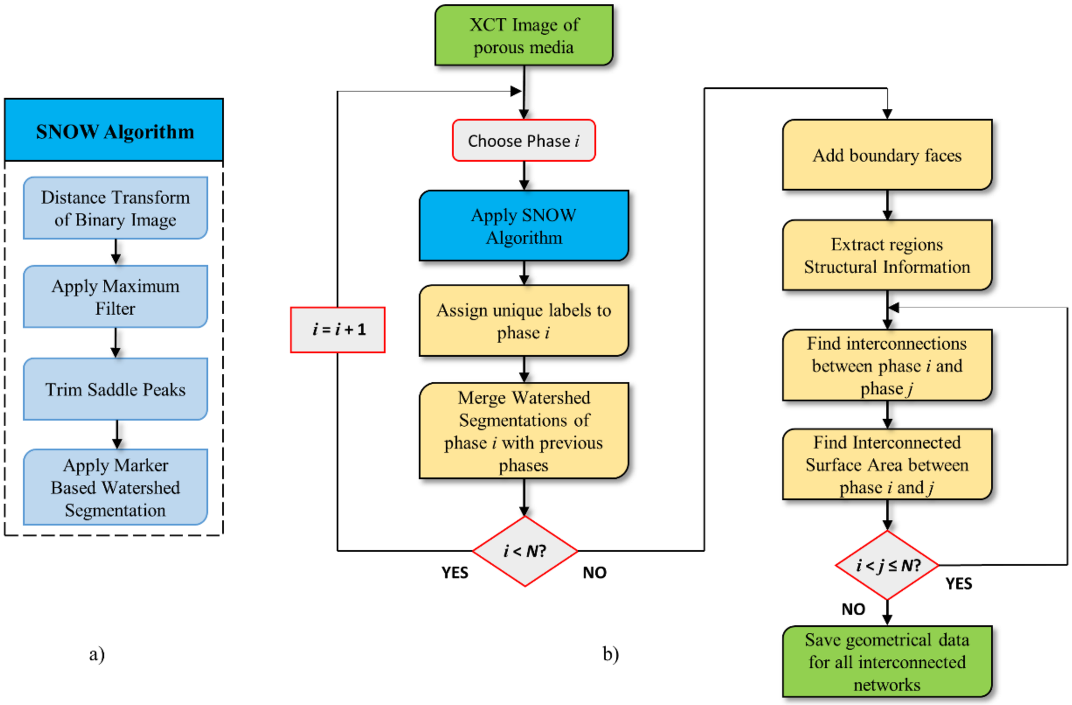

Figure 4.1 a) SNOW algorithm basic steps b) SNOW_N extraction algorithm flow chart

The N-phase network extraction algorithm (SNOW_N) was developed on the premise that the watershed segmentation can be applied on each phase in an image individually, and then these individual segmentations can be combined to form a composite image. The overall algorithm implementation is shown in Figure 4.1b. Firstly, each phase (1 to N) is partitioned into regions using the SNOW algorithm individually. Before recombining the segmentations, the partitioned regions of the j^{th} phase are relabeled in order to differentiate it from other phases. For this, if Np_i is the maximum label of i^{th} phase region then j^{th} phase first label will begin from $Np_i + 1$. After the relabeling process, all partitioned regions are merged together to form a composite watershed segmentation image. In the next step, boundary nodes are added to specify boundary conditions during the simulation process [94]. After assigning boundary nodes, the geometrical and structural features of each region are extracted one at a time without considering its phase association. The connectivity of the region under consideration is determined by scanning its neighbouring regions. This allows extracting throat properties of connected regions, including pore-to-pore, pore-to-CBD, binder-to-NMC, and so forth. Once all the geometrical and connectivity information is determined, the next step is to label the interconnections between each phase with other phases. This step finds throats that interlink any two phases with each other and stores it in the form of separate arrays. For N phases there will be NC_2 interconnection arrays. Next, the interfacial area between any two phases is determined using the marching cube algorithm which has been demonstrated to produce much more accurate values for interfacial area between regions [94]. Lastly, the extracted information is stored in the form of a Python dictionary which can be opened directly in the open-source modelling package OpenPNM [98]. The code is implemented in Python and is included in the open-source package PoreSpy [95].

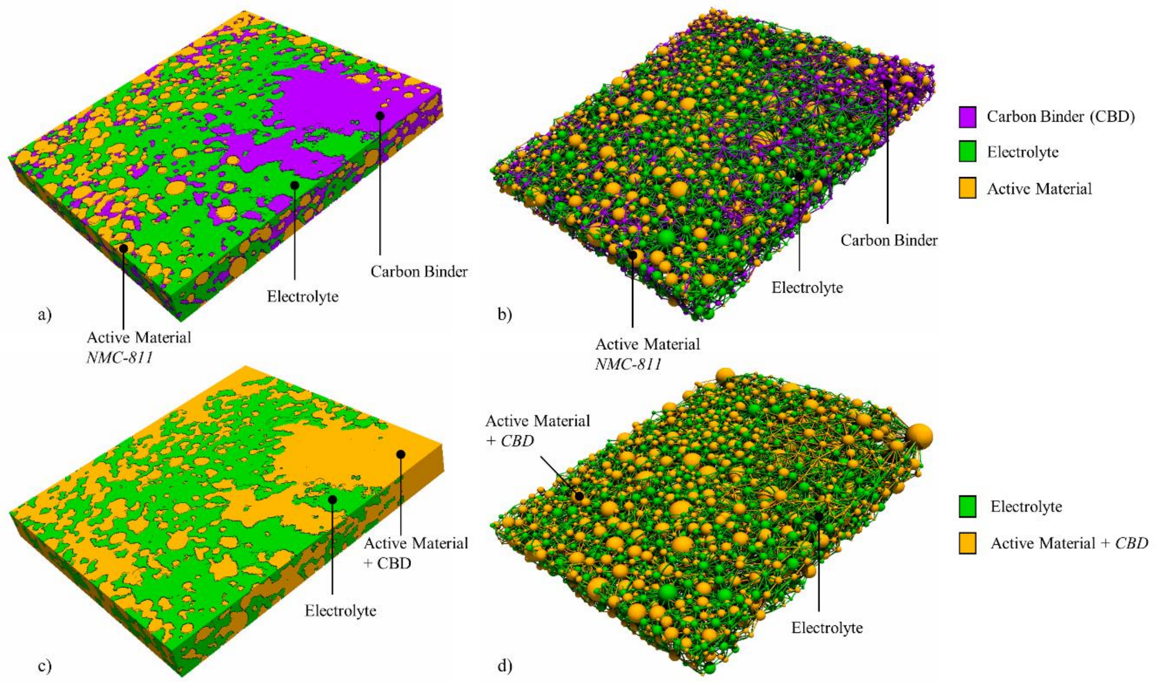

Figure 4.2 a) X-μCT image of lithium nickel manganese cobalt oxide ($LiNi_{0.8}Mn_{0.1}Co_{0.1}O_2$) cathode, b) Extracted three-phase network of (a), c) Two-phase image of porous cathode where active material and CBD correspond to one solid phase, d) Extracted two-phase network of (c)

To illustrate the impact of treating the binder and active material as a single phase, the developed SNOW_N algorithm was used to extract both two-phase and three-phase networks of the Li-ion NMC-811 cathode. The two-phase network was extracted by assuming the carbon binder domain (CBD) and active material phase as one solid phase. The extracted networks are shown in Figure 4.2. The green, purple and orange colour shows electrolyte, carbon binder and active material phase, respectively. The pore and particle size distribution for all phases is shown in Figure 4.3 and properties of both networks and original image are presented in Table 4.1.

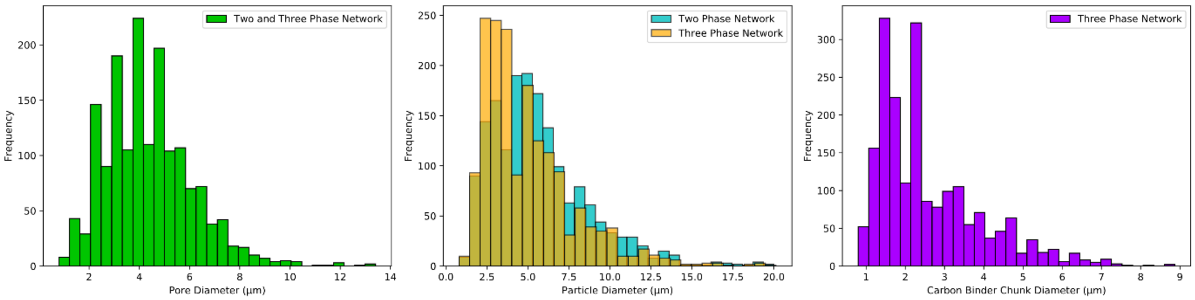

a) b) c)

Figure 4.3 a) Pore size distribution of electrolyte phase in both two and three-phase network, b) Active material particle size distribution in two and three-phase network, c) Carbon binder particle size diameter in three-phase network

Table 4.1 Properties of image and Extracted Pore Networks

Value	**X-μCT image**	**Three Phase Network**	**Two Phase Network**
Dimension *[voxels]*	568 x 639 x 65	568 x 639 x 65	568 x 639 x 65
Voxel Size *[nm]*	400	400	400
Phase *[vol %]*			
1. Electrolyte	38.6	38.23	38.1
2. Active Material	39.6	39.53	61.9
3. Carbon Binder	21.9	22.23	-
Electrolyte Phase: N_p, N_T	-	1648, 3619	1648, 3619
Active Material Phase: N_p, N_T	-	1712, 2057	1726, 5316
CBD Phase: N_p, N_T	-	1976, 4227	-
Interconnections:			
1. Electrolyte-Active Material	-	6888	11419
2. Electrolyte-CBD	-	8878	-
3. Active Material-CBD	-	7435	-

4.4.4. Network Validation by Direct Numerical Simulation

The SNOW network extraction algorithm has been previously validated for sandstone, fibrous media, and artificial foams (Voronoi tessellations) [97], and the SNOW-dual was validated for sphere packs [94], but it is still necessary to validate 3-phase extraction on the present Li-ion battery material image. The triple phase nature of the material (and its requirement for a triple phase boundary to exist) leads to specific sensitivities of the modelling.

The most direct validation is obtained by performing direct numerical simulation (DNS) on the image using a finite volume approach. This provides reference values for effective diffusivity of the pore space (i.e. tortuosity) and effective conductivity of the solid phase (including both NMC and CBD particles). These values can then be compared to those predicted by the extracted network to ensure that it accurately represents the porous structure. The following sections detail the procedure used to obtain the DNS results.

4.4.4.1. DNS Model Formulation

The predictive capabilities of the pore-network model were validated against the results computed by a DNS model, implemented in the FVM-based code ANSYS Fluent. The numerical domain was created using a direct mapping between the voxel image of the electrode and a hexahedral mesh generated with the same resolution (23,591,880 cells). Species and charge conservation equations (i.e., Laplace equation) were solved via user-defined scalars to determine the lithium-ion concentration and electronic potential, respectively. Therefore, the governing equation is given by:

$$\nabla \cdot (\Gamma \nabla \phi) = 0 \tag{4.1}$$

where Γ is either the mass diffusivity or electrical conductivity, and ϕ is the corresponding solution variable. In all cases, the Laplace equation was discretized in ANSYS Fluent using second-order central difference.

Several user-defined functions were used to customize the model, including boundary conditions, transport properties and output results. The material properties and boundary conditions were similar to those prescribed in the pore-network model. The only difference is that boundary conditions were also set at internal interfaces. Consequently, in the reaction-diffusion simulation, zero concentration was imposed at the electrolyte/active material interface to model limiting-current conditions, rather than prescribing a high reaction-rate constant at electrolyte/active material interface (as done in the pore-network model described below). Similarly, in the reaction-conduction simulation, current density at the electrolyte/active material interface was determined by direct application of Faraday’s law on the interfacial diffusive flux determined previously. A no-flux boundary condition was set at the electrolyte/CBD interface, while a coupled (i.e., continuity) boundary condition was prescribed at the active material/binder interface.

4.4.5. Pore-Network Formulation

The present study focuses on the cathode electrode of Li-ion battery that includes current collector and lithium nickel manganese cobalt oxide ($LiNi_{0.8}Mn_{0.1}Co_{0.1}O_2$) porous cathode operating under pseudo steady-state conditions. Figure 4.4 illustrates the schematic of a cell of lithium-ion battery domain. During discharge, lithium ions travel from the membrane side, through the electrolyte phase (pores) and intercalate into the active material (NMC-811) surface to form lithium nickel manganese cobalt oxide according to following electrochemical reaction:

$$x\mathrm{Li}^{+} + xe^{-} + Li_yNi_{0.8}Mn_{0.1}Co_{0.1}O_2 \rightarrow Li_{x+y}Ni_{0.8}Mn_{0.1}Co_{0.1}O_2 \qquad (4.2)$$

The physical processes occurring in the lithium-ion battery cathode during discharge are (a) diffusion and migration of lithium-ions in the electrolyte phase, (b) conduction of electrons in the active material and carbon binder domain and (c) reaction (i.e., intercalation) of lithium-ion at the interface of electrolyte and active material. Several simplifying assumptions were made in this work since the focus was on the pore-scale transport processes rather than complete battery operation. The generation and transport of heat were neglected, as were any side reactions such as SEI formation. Migration of ions due to electric fields were also neglected. Electrochemical kinetics were not included, but rather it was assumed that the kinetics of the lithium intercalation reaction was very fast on the surface of the active material. This assumption simplifies the problem by decoupling the electrolyte and solid-phase potentials, reducing it to reaction-diffusion in the electrolyte phase and reaction-conduction inactive material phase. It was also assumed that effective transport properties are not concentration-dependent as recently suggested in [99,100]. We assume all transport properties to be constant with changing concentration. The extension of this model to transient conditions relevant to charging and discharging will also be left for future work. The transport and kinetic equations that were used in the developed pore network model are given in the following sections.

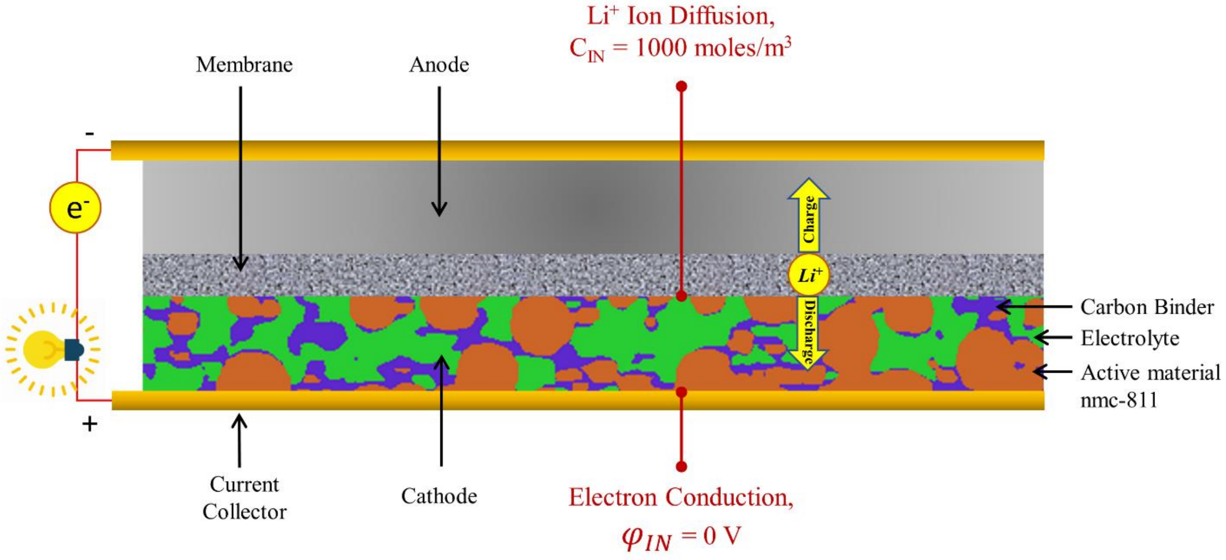

Figure 4.4 Schematic diagram of full cell lithium-Ion battery. The applied boundary conditions are shown in red colour

4.4.5.1. Lithium-ion transport

The lithium-ion transport in the electrolyte phase was considered to follow a reaction-diffusion process during the discharge cycle of the battery. The conservation of lithium-ions around a pore *i* in pore network under steady-state conditions can be represented by:

$$\sum_{j=1}^{N_i} q_{i,j} = R_i = kc_i \tag{4.3}$$

where q is the molar flow rate in mol/s. R_i is the net reaction rate of Li-ions in pore i. k refers to the reaction constant and c_i refers to the concentration of Li-Ion in pore i. N_i is the number of neighbour pores to pore i.

The molar flow rate q_{ij} between pore i and j can be defined using 1D Fickian diffusion:

$$q_{i,j} = \frac{D_{Li^+}A}{x_{i,j}}\left(c_i - c_j\right) = d_{i,j}\left(c_i - c_j\right) \tag{4.4}$$

where D_{Li+} is the bulk diffusion coefficient of Li^+ ions in the electrolyte phase. A is the cross-sectional area of conduit from pore i to pore j , $x_{i,j}$ is the length of conduit from pore i to pore j, c_j is the concentration of Li ion in the neighbouring pore j and $d_{i,j}$ is the diffusive conductance between pore i and j.

4.4.5.2. Electron transport

The charge conservation for an arbitrary solid particle i is represented by the following governing equation:

$$\sum_{j=1}^{N_i^{AM}} I_{i,j} = R_i^e = \mathrm{z} \cdot F \cdot R_i \tag{4.5}$$

where $I_{i,j}$ is the rate of charge transport from solid particle i to solid particle j in Coulombs s^{-1}. R_i^e is the net reaction rate of electrons at surface of particle i. F is Faraday's constant and z is the number of electrons.

The rate of charge transport is proportional to the potential difference between particle i and j as stated by Ohm’s law:

$$I_{i,j} = \frac{\sigma_e A}{l_{i,j}}\left(\varphi_i - \varphi_j\right) = \sigma_{i,j}\left(\varphi_i - \varphi_j\right) \tag{4.6}$$

where φ_i and φ_j are the electric potentials inactive material at particle i and j respectively. σ_e is the bulk electronic conductivity of active material (NMC-811). $l_{i,j}$ is the conduit length from particle i and j. $A_{i,j}$ is the cross-sectional area of the conduit. $\sigma_{i,j}$ is the electrical conductance between active material particle i and j.

It is assumed that no reaction takes place in the carbon binder phase. Therefore, the governing equation for charge conversation in this phase is as follows

$$\sum_{j=1}^{N_i^{CB}} I_{i,j}^{CB} = 0 \tag{4.7}$$

The rate of charge transport in carbon binder phase can be represented as 1D Ohm's law under steady-state conditions as

$$I_{i,j} = \frac{\sigma_{CB} A}{k_{i,j}} \left(\varphi_i^{CB} - \varphi_j^{CB}\right) = \sigma_{i,j}^{CB} \left(\varphi_i^{CB} - \varphi_j^{CB}\right) \tag{4.8}$$

where σ_e^{CB} is the electronic conductivity of carbon binder domain. φ_i^{CB} and φ_j^{CB} are potential difference in carbon binder region i and j respectively. $k_{i,j}$ is the conduit length in carbon binder region i and j respectively. The overall summary of the parameters used in this study is shown in Table 4.2.

Table 4.2 Summary of the parameters used in this study

Parameter	Value	Units	Description
$L_{cathode}$	2.6×10^{-5}	m	Cathode thickness
$A_{cross\text{-}section}$	5.807×10^{-8}	m^2	Cross-sectional area of cathode
$V_{cathode}$	1.51×10^{-12}	m^3	Volume of cathode
D_{Li^+}	1.81×10^{-10}	$m^2.s^{-1}$	Bulk diffusivity of Li ion in electrolyte phase [80]
σ_{CBD}	760	$S.\ m^{-1}$	Electronic conductivity of carbon binder phase [101]
σ_e	1.7×10^{-3}	$S.\ m^{-1}$	Electronic conductivity of NMC-811 [102]
C_{IN}	1000	$kg.m^{-3}$	Concentration of lithium ion at membrane-cathode interface
φ_{IN}	0	$Volt$	Voltage at cathode current collector
F	96485	$C.\ mol^{-1}$	Faraday's constant

4.4.5.3. Boundary conditions

The boundary conditions implemented for mass and current transport for different cases were as follows:

1. In the electrolyte phase, a Dirichlet boundary condition of 1000 mol m^{-3} concentration of lithium ions was assigned in inlet pores at the separator surface. For the simulation in which only effective diffusivity is calculated, a Dirichlet boundary condition of 0 mol m^{-3} at outlet pores (near the current collector) and zero-diffusive flux at solid/electrolyte interface was applied, while for reaction-diffusion simulation Neumann boundary condition of zero diffusive flux was set in the outlet boundary pores.
2. In the active material and carbon binder phase, 0-volt Dirichlet boundary conditions were implemented at the current collector. For simulations which calculate effective conductivities of the active material and carbon binder phases, 1 volt Dirichlet boundary conditions at outlet particles and zero-conductive flux at solid/electrolyte interface were applied, while for reaction-conduction simulation, Neumann boundary condition of zero flux of charge was implemented at outlet particles.

4.4.5.4. Pore-scale conductance models

To calculate the transport rate between two pores i and j it is necessary to determine the total conductance of the conduit between the two pores, which consists of half of pore i, the throat, and half of pore j. In the present work, a custom geometrical model for the conductance of each pore was applied, based on truncated pyramids as shown in Figure 4.5. Due to the generally spherical nature of the grains in the electrode (both NMC and CBD phases), the contacts between two pores essentially have no throat of length greater than zero. This overlapping sphere-sphere contact was modelled as the intersection of pairs of 4-sided truncated pyramids. The base of the pyramids was found from the diameter of pore, and the truncated side was set to the throat diameter. In this model, the conductance of the throat was assumed negligible because of zero length and the effect of the constriction between pores was included in each pore's contribution. The total conductance, G, in a conduit made up of pores i and j and throat k can be calculated since the resistances act in series:

$$\frac{1}{G_{i,j}} = \frac{1}{g_{i-k}} + \frac{1}{g_{j-k}} \tag{4.9}$$

where g_{i-k} and g_{j-k} are found for each individual pore-throat section as described below.

This results in the following expression for the electrical conductance of pore i connected to throat k:

$$g_{i-k}^{e} = \sigma \frac{d_i d_k}{L} \tag{4.10}$$

where d_k is the diameter of throat, L is the distance from centroid of pore i to centroid of throat k and d_i is the diameter of pore i which is adjusted so that volume of truncated pyramid is equal to half of the volume of pore i.

The pore space is defined by the interstitial regions between grains of solid material. In this case, like the solid phase discussed above, the throats are essentially constrictions defined by the converging-diverging nature of the spheres. As such, the same truncated pyramid model was also applied:

$$g_{i-k}^{d} = \mathcal{D}_{Li^{+}} \frac{d_i d_k}{L} \tag{4.11}$$

where $\mathcal{D}_{Li^{+}}$ is the diffusion coefficient of the Li-ion in the electrolyte and the geometrical properties are defined as above. All of the lengths and diameter values were determined during the network extraction stage described above.

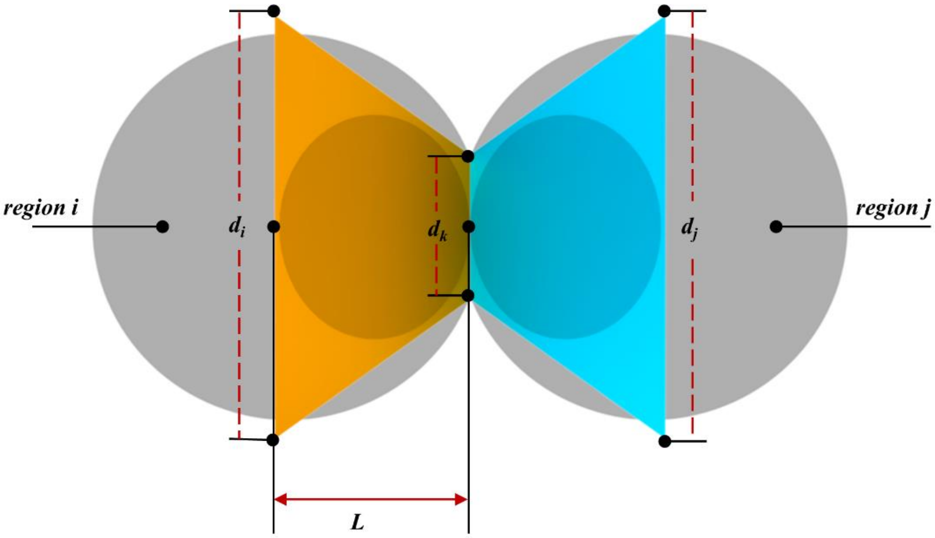

Figure 4.5 Schematic of geometric properties of pore scale conduit in network model

4.5. Results and discussion

4.5.1. PNM validation against DNS

4.5.1.1. Effective Transport Properties

The pore network model (PNM) results were compared with direct numerical simulations (DNS) for two different conditions. In the first case, effective transport properties were determined using both PNM and DNS in both the electrolyte and solid phase under steady-state conditions. Dirichlet boundary conditions were used in both inlet and outlet pores as described in section 4.4.5. The comparison of results is shown in Table 4.3. The combined effective conductivities in the active material and carbon binder phase were calculated using both approaches and the relative error was found to be approximately 3%. The normalized effective diffusivity of Li-ions in the electrolyte phase is 0.178 in PNM in comparison to 0.145 in DNS simulation, meaning that the PNM model overestimated diffusivity by 18.5% (taking the DNS result as correct), which is not as close as the solid phase, but still quite acceptable. These higher relative errors in this case of diffusion can be attributed to the simplification of irregular pore-scale conduit geometry to truncated pyramids, which evidently works better for the solid phase because it's generally spherical than the pore phase. Given that the pore network modelling approach takes significantly less computational time than DNS the relative errors reported in Table 4.3 are acceptable for performing engineering design and optimization calculations. The simulation results in terms of concentration and voltage profiles are compared for both cases in Figure 4.6.

Table 4.3 Summary of results in this study

Variable	**Pore Network Model**	**Direct Numerical Model**	**Relative Error (%)**
D_{eff}/D_{bulk}	0.178	0.145	18.5
σ_{eff}	31.9	30.92	3.07
Li^+ $flux_{void\text{-}NMC}$	1.481×10^{-2} mol/m^{2}s	1.496×10^{-2} mol/m^{2}s	0.67
$i_{void\text{-}NMC}$	1429.8 A/m^2	1411.7 A/m^2	1.26

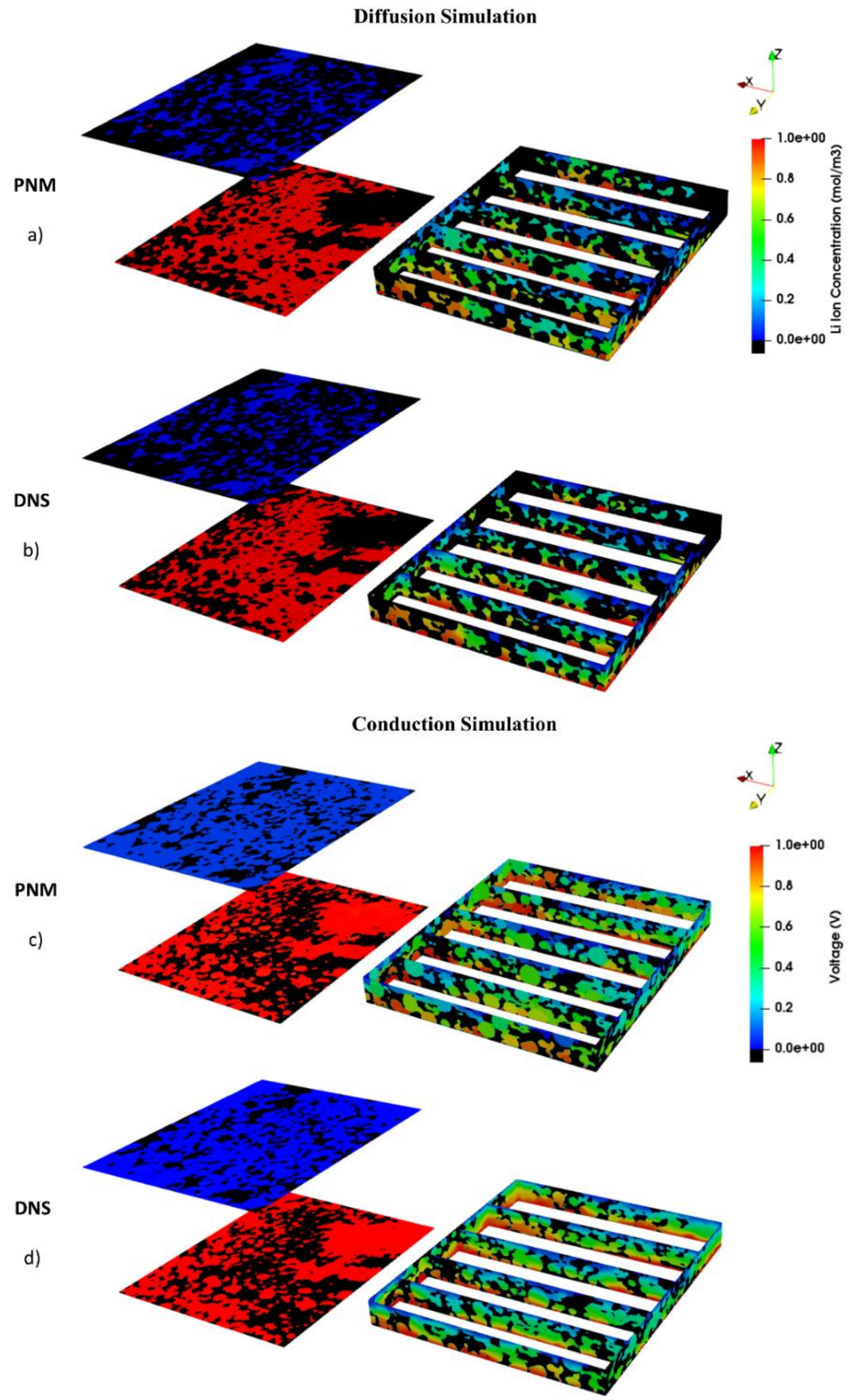

Figure 4.6 (a) and (b) Comparison of DNS and PNM model in pure diffusion simulation, (c) and (d) DNS and PNM model comparison in pure conduction simulation

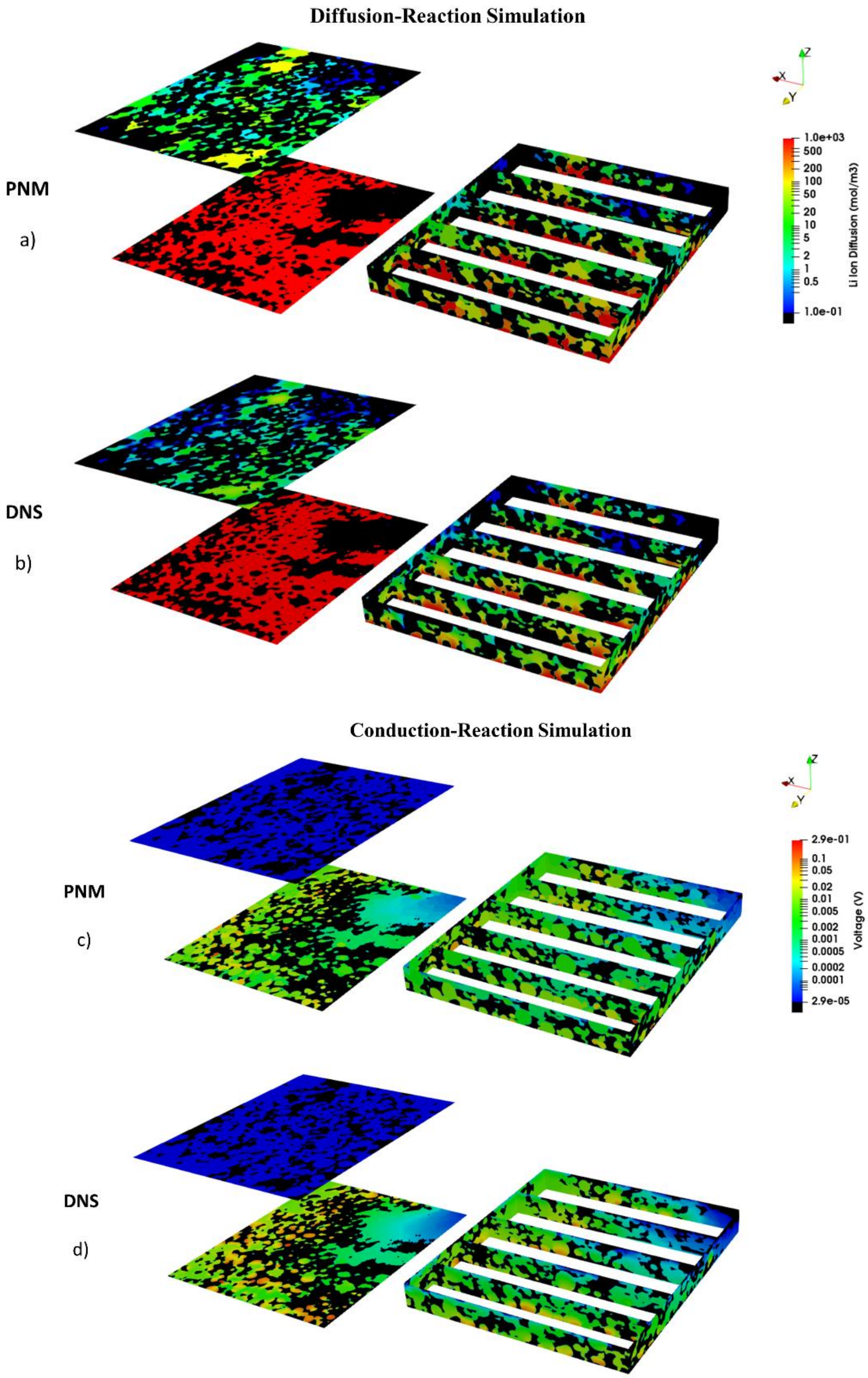

Figure 4.7 a) Direct Numerical simulation of Li ion diffusion and reaction, b) Pore network modelling simulation for same case as in (a), c) Direct numerical simulation of conduction-reaction in active material and carbon binder phase, d) Pore network modelling simulation of same case as (c)

4.5.1.2. Comparison of Computational Costs

One of the benefits of pore network modelling over direct numerical method is low computational cost required for simulations. To study the computational cost of the simulations described above we have divided computational time into two parts. 1) Meshing or extraction time and 2) Problem solution time. In this study, the approximate time taken to build 25.5 million mesh elements domain was 1 hr. On the other hand, in pore network modelling the equivalent to meshing is extracting the network, which required approximately 5 minutes to extract 6460 nodes. However, when comparing the computational cost of running the simulations, the average solution time in DNS and PNM was 25 min and 1.21 seconds respectively. The computational time was calculated in Inter Xeon E5-2640, 2.40 GHz, 128 GB RAM and 20 Cores. For direct numerical simulation, the solver was parallelized across 10 cores to achieve residual below 10^{-8} while PNM solution was calculated using only 1 core. This comparison highlights the major advantage of the PNM approach over DNS, especially while simulating large electrode domains. The comparative advantage of PNMs would become even more important when considering multiphysics such as migration of ions, and transient behaviour.

4.5.2. Coupled Electron Conduction and Diffusion-Reaction

With the pore-network extraction and geometrical representation validated by the comparison of overall effective transport properties above, the model was then used to predict the maximum achievable current density. For this study, reaction-diffusion of lithium-ions in the electrolyte phase and reaction-conduction of electrons in the active material and carbon binder domain phases were analyzed simultaneously in the presence of a fast reaction of Li-ions at the NMC phase surface, as discussed in section 4.4.5. This assumption forces Li-Ion reaction to follow first-order kinetics instead of Butler-Volmer kinetics as per equation (4.3). Although actual Butler-Volmer kinetics can be implemented in the PNM model [86], the purpose of this work was to explore the impact of structure on the maximum performance of Li-ion cells and to validate our PNM approach to solve lithium-ion battery problems as a foundation for future work. As can be seen in Table 4.3, the PNM and DNS models predict a maximum or limiting current density of 1.43 and 1.41 mA mm^{-2}, respectively. These values are substantially higher than experimentally observed values, which are typically in the range of 1x10^{-3}-2x10^{-2} mA mm^{-2} [80]. It was expected that the present simulations would be higher than an operational battery since mass transfer limited conditions were forced by applying very high reaction rates at the electrolyte-active material boundary. Moreover, we did not consider that Li-ions must diffuse into the active material after intercalation occurs. It is actually quite instructive to note that the pore structure is capable of supporting such high current densities and that the cumulative effect of the real phenomena not considered in this study hinders the reaction rate substantially. Adding more complexity to the pore network model in future work will be valuable for understanding the contribution of each process.

It is also observed that both the DNS and PNM simulations give very similar results for this case study. The average Li-Ion flux at electrolyte-active material interface differs by less than 1% between the PNM and DNS approaches. The results of the two approaches in terms of concentration and voltage distributions are shown in Figure 4.7. From the results in Table 4.3 it can be visually confirmed that the PNM approach produces results well within acceptable error to be used as an alternative modelling method for simulating Li-Ion battery problems.

4.5.3. Impact of Electrode Structure

Most pore-scale models of lithium-ion batteries in the literature treat the electrode as a two-phase system consisting of void and solid, meaning the active material and carbon binder domain are treated as a single phase. Given that carbon is specifically added to overcome the poor electrical conductivity of the active material, it is expected that such a simplification can produce erroneous results. This simplification was necessary since previously available tomography images only contained binary phase information. Attempts to work around this limitation have been made by algorithmically adding CBD to the solid phase [103,104]. The available of a true 3-phase image in the present work provides an opportunity to better understand the importance of treating CBD as a separate phase. he developed pore network was used to study two different cases described below.

4.5.3.1. Impact of treating carbon binder as a separate phase

As described in section 4.4.4, the SNOW_N algorithm was used to extract both two and three-phase networks of lithium-ion cathode. The schematic diagram of both networks is shown in Figure 4.2. These networks were used to perform comparisons of electrodes with and without carbon binder phase as shown in Figure 4.3. Table 4.4 shows the surface area, effective conductivities and current density calculated in both two-phase and three-phase network. As expected, the average particle size in the two-phase network is larger than the three-phase case due to the fact that carbon binder particles are lumped together with the active material.

As a limiting case, the maximum current density that can be supported by the structure was calculated by simultaneously modelling the diffusion of Li-ions with a rapid reaction in the active material. Limiting current may not be observed practice, but it is an interesting modelling target since it reveals that maximum current that can be supported by the electrode structure if electrolyte phase transport were the only source of mass transfer resistance. The current density was found by calculating the total rate in mol s^{-1} of Li-ions entering the domain from the membrane, converting to total current, I, using Faraday's law, then normalizing by the cross-sectional area of the current collector. As shown in Table 4.4 the current density is 24.4% higher in the two-phase network compared to the three-phase case. This decrease when considering the CBD is due to the reduction in reactive surface area available when CBD is treated explicitly. It should be noted that the few studies which did treat the CBD as a separate phase used DNS. Due to high computational cost, these studies were limited to a domain volume of approximately 20.2 µm × 18.13 µm × 12.4 µm [80] compared to the electrode volume of 227.2 µm × 255.6 µm × 26 µm used in the current study; approximately 1.8 times larger when the voxel sizes are considered. The volume limitation in the present work was not due to computational cost, but rather the field of view of the image. This has considerable implications for battery modelling – using a PNM approach it would be possible to model whole electrodes imaged via 3D stitching of several CT data sets without compromising on acquisition resolution.

Table 4.4 Summary of results in case study 1

Variable	Units	Three Phase Network	Two Phase Network
$SA_{\text{interface}}$	m^2	$1.08x10^{-7}$	$2.84x10^{-7}$
σ_{effl}	S/m	31.9	$8.32x10^{-4}$
Li^+ $\text{flux}_{\text{void-NMC}}$	mol/m^2s	$1.481\text{x}10^{-2}$	$7.44\text{x}10^{-3}$
$i_{\text{current collector}}$	mA/mm^2	2.652	3.51

4.5.3.2. The role of nanopores in the carbon binder phase

It has been reported that nanoporosity of the carbon binder phase in the porous cathode affects overall ionic and electronic transport process [93,103,105]. This nanoporosity not only alters ionic diffusion pathways and access to the active material, but also affects the electron conducting network. To understand the importance of nanopores in the carbon binder phase, a parametric study was conducted where the porosity for the carbon binder was varied. These nanopores were not modelled explicitly as this would massively increase the computation demand of the model, negating the value of the PNM approach. Instead, the effect of nanoporosity was included by altering the effective conductivity and diffusivity of the CBD nodes in the network. To scale these transport parameters as a function of nanoporosity a Bruggeman-type relation was used [106], given by equation (4.12) and (4.13):

$$D_{CBD}^{Li^+} = \mathcal{D}_{Li^+}(\varepsilon_{CBD})^n \tag{4.12}$$

$$\sigma_{eff} = \sigma_{CBD}\,(1-\varepsilon_{CBD})^n \tag{4.13}$$

where ε_{CBD} is the nanoporosity of the carbon binder phase, $\mathcal{D}_{Li^+}$ is the intrinsic diffusivity of Li-ion in electrolyte phase, σ_{CBD} is the intrinsic electronic conductivity of carbon binder phase. $\mathcal{D}_{Li^+,CBD}$ and σ_{eff} represent effective diffusivity and electronic conductivity after inclusion of nanopores in the carbon binder phase. n represents the Bruggeman constant which depends on how the nanopores are connected.

Traditionally, $n = 1.5$ for a sphere pack, but is often higher for real random structures, so in this study, n was varied between 1.5 and 3.

Figure 4.8 shows the impact of varying ε_{CBD} on various aspects of the electrode performance with n as a parameter. Figure 4.8a shows how the effective electrical conductivity of the entire network decreases as the nanopore fraction of the carbon binder increases. As $\varepsilon_{CBD} \rightarrow 1$ the electrical conductivity for the electrode nears 0 for all values of n, since the conducting carbon material is sacrificed. Figure 4.8b shows that the effective diffusivity of the network increases as ions are able flow through the nanoporosity. As $\varepsilon_{CBD} \rightarrow 0$ the effective diffusivity approaches the value obtained in 4.5.1.1 for the pore network. The electrolyte phase tortuosity $\tau_{Li^+} = \frac{\varepsilon D_{Li^+}}{D_{eff}}$ match well with recent study on LIB's transport "distortion"[107]. It was observed that addition of high amounts of nanoporosity more than doubles the ability of Li ions to transport throughout the network. It is unlikely, however, that such high amounts of porosity could be achieved. Moreover, as already seen, high porosity drives the electrical conductivity of the network toward zero value so is not a practical target anyway. For both transport processes, the value n has only a small impact, except at low values of ε_{CBD}. For $\varepsilon_{CBD} < 0.2$, the effective diffusivity is almost unchanged while the electrical conductivity decreases noticeably. Note that equation (4.12) and (4.13) do not include percolation effects, which would make this behaviour at low ε_{CBD} even more pronounced.

More interesting is the interplay between increasing effective diffusivity and decreasing conductivity as the nanoporosity is increased. Simulations were performed with the ion diffusion-reaction coupled to the electron conduction, such that the voltage drop in each particle was determined that ensure a sufficient flow of electrons were delivered to each active site to match the consumption of ions there. Figure 4.8c shows the voltage of each NMC and CBD particle in the network as a function of position in the thickness direction of the electrode. These results were obtained for $\varepsilon_{CBD} = 0$ and $n = 3$. It can be seen that a small number of NMC particles display a high voltage. This may indicate that these particles suffer from artificially decreased connectivity with the current collector due to edge effects from image cropping. None of these particles are fully disconnected (i.e. floating in space) as sometimes occurs due to image cropping, but the topology near the edges is unavoidably impacted and this could explain the observed voltages.

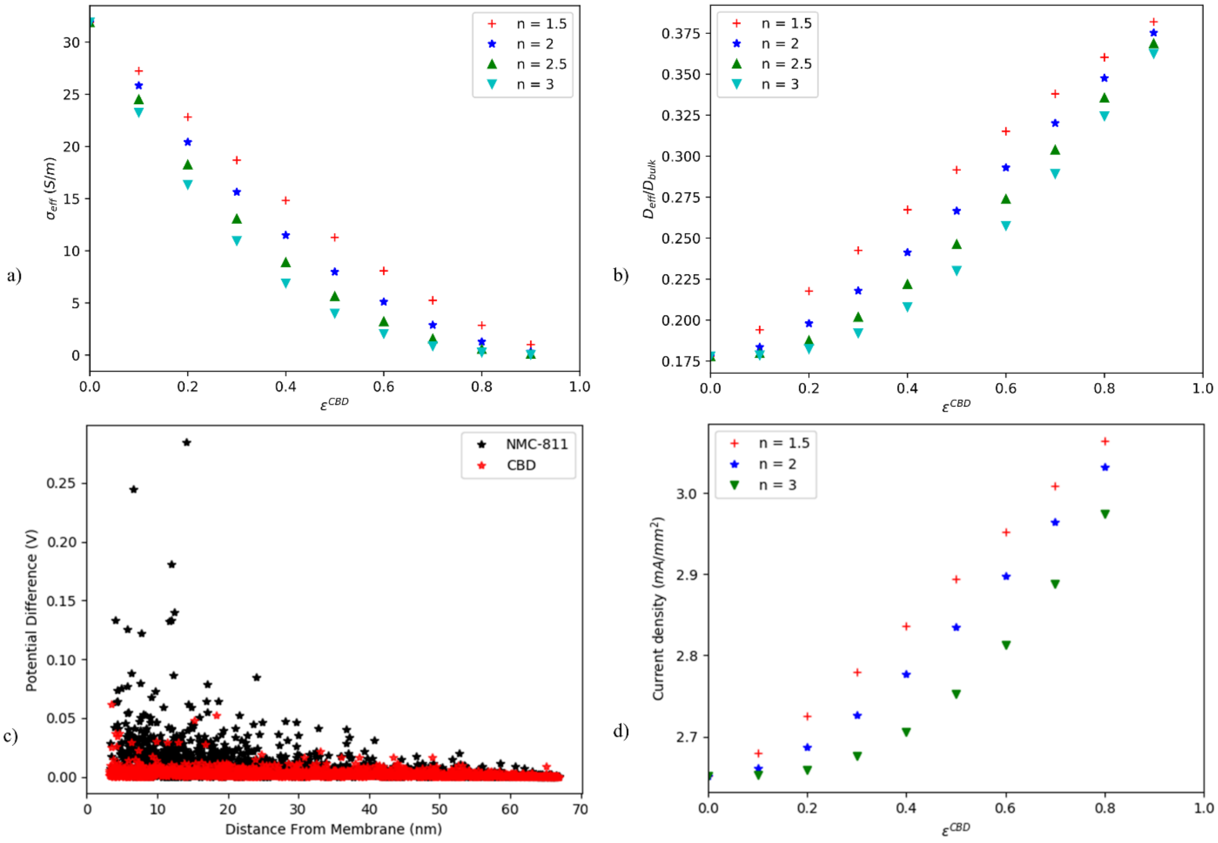

Figure 4.8 a)Effective electronic conductivity of solid matrix (NMC+CBD) vs nanoporosity of CBD, b) Effective diffusivity of Li-Ion in electrolyte phase vs nanoporosity of CBD, c) Potential difference in solid matrix vs distance from membrane at ε_CB=0 and n=3, d) Current density of solid matrix vs CBD nanoporosity.

Figure 4.8d shows current density simulated at different ε_{CB} values. It can be seen that current density increases from 2.65 $mA.mm^{-2}$ to 3.1 $mA.mm^{-2}$ by changing the nanoporosity from 0 to 80% phase. This represents an 16.8% increase in maximum current density, but it must be conceded that simulation is not indicative of actual performance, since in reality, the reaction rate would drop significantly in sites with a high ohmic overpotential due to the exponential dependence of electrochemical kinetics on voltage. The observed behaviour is due to more available reaction area and more Li-ion pathways available from the electrolyte phase to active material due to the presence of nanopores in CBD. The loss of electrical conductivity is not factored into this result, and it is quite likely that a peak in current would be observed as some intermediate value of ε_{CBD}, though this is outside the scope of the present work.

4.6. Conclusions

In this work, a pore network extraction algorithm was developed to extract connectivity and geometrical information from a ternary X-ray tomography image of a three-phase lithium nickel manganese cobalt oxide ($LiNi_{0.8}Mn_{0.1}Co_{0.1}O_2$) porous cathode. The extracted three-phase network not only includes geometric information of each phase but also topological information such as the interlinking of all phases with themselves and each other. This enables the study of pore-scale transport through the structure while considering the transport process in each phase.

For validation, effective transport properties including the effective diffusivity of the pore phase and effective conductivity of the solid phase were calculated using DNS as a reference solution, and results compared favourably with the extracted network. Once the model was validated, more sophisticated simulations were performed by considering reaction-diffusion and reaction-conduction process in electrolyte and solid phase of three-phase network. These studies mimicked battery operation for the limiting case of maximum current since only diffusion in the electrolyte phase and very fast kinetics at the electrolyte-active material interface were considered. This revealed that the maximum currents that can be supported by the electrode structure are substantially higher than experimentally observed currents.

The developed pore network model was used in two case studies to highlight the effect of incorporating nanopores in the carbon binder phase, as well as the importance of using three-phase network over two-phase network of lithium-ion battery. The results showed a 24.4% decrease in current density when the carbon binder was treated as a separate phase compared to lumping the CBD and active material into a single phase, as is often done in previous pore-scale simulations on binary images. Moreover, it was observed that ionic and electronic transport properties are affected by inclusion of nanopores in the carbon binder phase. The current density was observed to increase by 16.8% as the nano-porosity of CBD increases from 0 to 80%.

As compared to direct numerical simulation, the present work uses relatively large electrode domain to model multiple coupled phases together in a computationally efficient way. With the increased ability to stitch larger regions of electrode images together and decreasing data acquisition time, the approach explored here will become increasingly necessary in order to accurately describe realistic Li-ion battery electrodes and the inhomogeneities that can be present across their entire area. Also, the current study focuses only on steady-state processes, but due to low computational cost of pore network models, a transient approach to simulate porous media can be adopted.

Chapter 5 Efficient Extraction of Massive Size Pore Networks

5.1. Preface

This paper removes a major bottleneck in network extraction algorithms and enables the extraction of massive size tomograms without running out computational limits of standard workstation or laptop machine. The developed algorithm uses geometric domain decomposition approach to divide large size image into smaller sub-domains and stitching processed subdomains as a postprocessing step. The study also addresses an important drawback of image-based modelling i.e resolution effects that can lead to inaccurate results and highlights the importance of using high-resolution images for extraction for pore network modelling studies.

5.2. Overview

Image-based modelling of porous media to study the transport and reaction processes has become an essential tool. The availability of increasingly large image datasets at high resolution creates a need to develop algorithms that can process massive size images at a low computational cost. This study presents an efficient workflow to extract pore networks form large size porous domains using a watershed segmentation with geometrical domain decomposition. The method subdivides a porous image into smaller overlapping subdomains and performs a watershed segmentation on each subdomain in parallel or serial modes of operation to save CPU time or memory RAM, respectively. The computational performance of the algorithm was analyzed on a large size image and found to consume 50 percent less memory and up to 7 times less CPU time than the standard watershed implementation. Pore networks of four massive digital rock images were extracted and the effective permeability predicted by the networks agreed well with previously investigated values illustrating the accuracy of the method. An additional application of this methods, taking advantage of the reduced computational cost, is the upgrading of low-resolution image. It was found that that increasing the resolution of a coarse image leads to more accurate predictions by helping the watershed segmentation produce a more faithful pore network model. The developed algorithm is implemented in Python and included in the open-source project PoreSpy. It uses highly optimized and efficient modules such as Dask and Numba to obtain maximum performance. The domain decomposition approach used here will also lend itself well to processing on distributed memory clusters, enabling the processing of even larger porous domains.

5.3. Introduction

Image-based modelling of porous media to study transport and reaction processes has become a key tool thanks to a relentless increase in computational power [36,108–111]. This has been accompanied and spurred on by the advancement of 3D imaging techniques, such as X-ray micro- and nano-computed tomography (CT) and focused ion beam scanning electron microscopy (FIB-SEM), that have enabled the acquisition of massive domains at resolutions better than a fraction of micron. For instance, domains can be imaged with current CT techniques as large as 2000 voxels across and essentially unlimited in height since scans can be stitched together [112–114]. Modelling transport processes, especially complex ones involving reactions and multiple coupled physics, using numerical techniques known collectively as direct numerical simulation (DNS) on such large domains strain even the most advanced modern workstations, however. One common remedy is to use pore network modelling (PNM), which is the most efficient when compared to other pore-scale modelling approaches [115] and its importance has been well established in modelling transport processes of various types of porous media [86,116–118].

The promise of using PNMs to efficiently model complex transport processes in large domains is currently limited by the network extraction step which can take hours or more. There are three main approaches to network extraction and they all depend on image analysis, which can be resource and computationally intensive. The approaches are (1) maximal ball [119,120] , (2) skeletonization or medial axis thinning [121,122], watershed segmentation [123] and 4) some hybrid techniques [124,125]. The present work focuses on the third approach, by adapting the SNOW algorithm developed by [97]. The main computational bottleneck of this algorithm is the watershed segmentation step which requires high computational memory (RAM) and a significant amount of CPU time as the size of the 3D image approaches and exceeds 1000^3 voxels. It should be stressed that the present work can be applied to any technique that uses a watershed segmentation since it is applied to the result of the watershed and is therefore agnostic to how the watershed was performed.

There have been a few recent attempts to accelerate network extraction by employing parallelization. [126] approached the problem by dividing the image into several subdomains and performing watershed segmentation on each subdomain individually. A pore network was then extracted from each subdomain and these networks were subsequently stitched together to get one large network. The stitching was done by analyzing the interaction of the throats at the intersection of two neighbouring subdomains. Although their algorithm obtained an increase in computational efficiency, the accuracy was sacrificed since the pore connections and throat radius at the intersections of two domains are handled based on arbitrary stitching rules. The final pore network was found to differ noticeably from the network extracted from a single large domain, and moreover, the result depended significantly on the number and size of subdomains used. [127] developed a stitching method to join the two neighbouring subdomains statistically. Similar to the approach of [126], stitching networks "post-extraction" introduces errors in the predicted transport properties, and the relative error changes depending on the number of subdomains.

To remedy the limitations of stitching networks 'post-extraction', the present work focused on obtaining a watershed via parallelizing the watershed step, then performing network extraction on the entire image. A key factor to note is that the number of segmented regions in a large image is far fewer than the number of voxels. Therefore, if a segmented image can be obtained efficiently, the network extraction step can be applied to the segmentation without concern for efficiency. In general, there are two approaches to parallelizing the watershed: redefining the inner workings of the algorithm to work in truly parallel way, or dividing the image into chunks then applying an existing algorithm on each chunk individually [76,128,129].

The first approach is quite challenging because as pointed out in several reviews [130,131], the watershed is inherently iterative or sequential in nature requiring multiple passes over the image. Typical performance gains for algorithms in this category are between 2-4x on 8 core machines [130,132–134]. The best performance gain on more than 1000^3 voxels images were achieved by [133]who reported an average speed-up of 5x on a machine with 8 cores, but conceded that the accuracy of the segmentation may not be maintained. Their speed-up was also inflated since they parallelized the immersion algorithm of [135], which is faster than the marker-based segmentation of [136] and [137] as no preprocessing steps to define markers are required. Attempts have also been made to develop parallelized algorithms for use on distributed-memory systems [128,129], but again the need to share information between nodes during the processing limits the performance gains. In general, intrinsically parallel algorithm only achieve moderate speed improvements, each implementation is specific to one type of watershed, and they involve sophisticated implementations that are not widely available for use by porous media researchers.

The other approach to parallelization is referred to as divide-and-conquer or geometric domain decomposition, where the image is divided into chunks and each is processed separately, followed by a post-processing step to recombine each chunk back into a single domain. This approach offers several useful advantages as it can be run on distributed-memory systems as well as shared-memory machines with ease. The former has the benefit that many nodes can be requisitioned and/or each node can have a large amount of RAM, for processing massive images. Of course, this requires access to specialized computational resources. Because no information is exchanged between processes, domain decomposition schemes can optionally be run asynchronously, meaning that a single shared-memory machine can be used to analyze large images by processing each chunk in series. This allows the use of normal desktop or even laptop computers on images that would otherwise be infeasibly large. Domain decomposition schemes can also be run in parallel on shared-memory high-performance workstations, allowing a high degree of flexibility in how they are run. Another advantage is that the user is free to choose which watershed algorithm is applied to each domain. For instance, it has been shown that a marker-based watershed with carefully selected markers is necessary to obtain a valid network from porous media images [97], so the ability to choose the algorithm and its settings is critical. As another scenario, if one had access to a distributed-memory system, each node could use an internally parallelized algorithm (of the type discussed above), and domain decomposition could be used to harness many nodes, significantly increasing the computational performance. The downside of the domain decomposition approach is that the accuracy of the segmentation is not assured, as it depends on the handling of interfaces between each subdomain, which is one of the major points addressed in this work.

This work presents a pore network extraction workflow that is based on parallelized watershed segmentation using domain decomposition. The proposed algorithm is conceptually simple, requiring only that each subdomain overlaps its neighbour by a sufficient amount to prevent edge artefacts, and followed by relabeling of watershed basins by comparison of the overlapping regions. All of this is done in the pre- and post-processing steps, so the actual watershed function is untouched. Crucially, the proposed approach can extract an identical network as that without domain decomposition, and the result is independent of the number of subdomains. The developed algorithm's computational performance was tested on a variety of large images and shown to be many times faster than the currently available approaches based on existing single-core implementations. The presented algorithm, by working on each subsection of the image separately, can also be applied in serial processing mode for cases where RAM is limited, and the effectiveness of this scheme was also explored. The proposed domain decomposition algorithm, therefore, offers the option of fast parallelized processing on high-performance workstations with many cores and ample RAM, or slower serial processing on lesser machines with limited cores and RAM. The possibility also exists for the present algorithm to be deployed on distributed-memory systems, though this aspect was not explored in the present work. An additional benefit of the present approach is that any watershed algorithm can be applied, allowing users to customize the scheme for their own workflow. Lastly, and most practically, this present algorithm is implemented using widely accessible open-source python tools such as the Scipy stack [138], Dask [139] and Numba [140]. The algorithm is included in the in open source project PoreSpy [95], and the output of code is also well aligned with open source pore networking modelling project OpenPNM [32].

Table 5.1 Image Sample used in the present study

Type of Study	Name of Sample	Sample ID	Dimensions [x, y, z]	Resolution µm	Porosity %
Algorithm Validation	Berea	1	1024, 1024, 1024	2.7745	20.25
	Bentheimer	2	1000, 1000, 1000	3.0035	21.67
	Doddington	3	1000, 1000, 1000	2.6929	19.58
	Ketton	4	1000, 1000, 1000	3.00006	13.30
	Random Sphere Packing	5	520, 520, 520	1	30.01
Computational Performance	Bentheimer	6	500, 500, 7040	6	23.9
	Fontainebleau	7	500, 500, 4096	3.662	13.73
Analysis of Large Size Tomograms	Berea	1	1024, 1024, 1024	2.7745	20.25
	Bentheimer	2	1000, 1000, 1000	3.0035	21.67
	Doddington	3	1000, 1000, 1000	2.6929	19.58
	Fontainebleau	8	2048, 2048, 2048	7.324	14.23
Effect of Resolution	Berea1	9a	512, 512, 512	5.549	20.254
	Berea2_zoomed	9b	1024, 1024, 1024	2.7745	20.254
	Berea	1	1024, 1024, 1024	2.7745	20.251
	Bentheimer1	10a	500, 500, 500	6.007	21.03
	Bentheimer2_zoomed	10b	1000, 1000, 1000	3.0035	21.03
	Bentheimer	2	1000, 1000, 1000	3.0035	21.67
	Doddington1	11a	500, 500, 500	5.3858	21.74
	Doddington2_zoomed	11b	1000, 1000, 1000	2.6929	20.00
	Doddington	3	1000, 1000, 1000	2.6929	19.58
	Ketton1	12a	500, 500, 500	6.00012	12.41
	Ketton2_zoomed	12b	1000, 1000, 1000	3.00006	12.41
	Ketton	4	1000, 1000, 1000	3.00006	13.30
	Random Sphere Packing1	13a	250, 250, 250	2	34.51
	Random Sphere Packing2_zoomed	13b	500, 500, 500	1	34.51
	Random Sphere Packing3	14	500, 500, 500	1	33.57

5.4. Methodology

5.4.1. X-ray micro-computed tomography Image Samples

To investigate the computational performance and geometric domain decomposition artefacts if any, 13 different types of 3D datasets were used. These included the X-ray μCT images of different types of rocks provided by Imperial College London [141,142], random sphere packings were generated using PoreSpy [95], and massive size images of the Fontainebleau Sandstone samples were constructed by Institute for Computational Physics at the University of Stuttgart [143]. A large size Bentheimer sandstone image obtained by [112] was downloaded from the DigitalRockPortal [144]. The sizes, resolutions, and porosities of images used in different studies are shown in Table 5.1. Equal size subdomains were created from the original images during the domain decomposition process, so some images were cropped by a few voxels to make it evenly divisible by the decomposition ratio and their final cropped size are mentioned in the respective study.

5.4.2. Network Extraction Algorithm

The SNOW algorithm as elaborated in [97] was used to perform a marker-based watershed segmentation and network extraction for all steps in this study. The algorithm uses a Gaussian blur and two custom filters to remove spurious peaks from the distance transform before performing marker-based watershed segmentation on 3D Image. A detailed comparison with commonly used extraction algorithms and modelling approaches are provided in [97,145]. The segmented regions obtained using SNOW algorithm are then used to extract geometrical and structural information of the network. The workflow for the SNOW pore network extraction methodology is shown in Figure 5.1a.

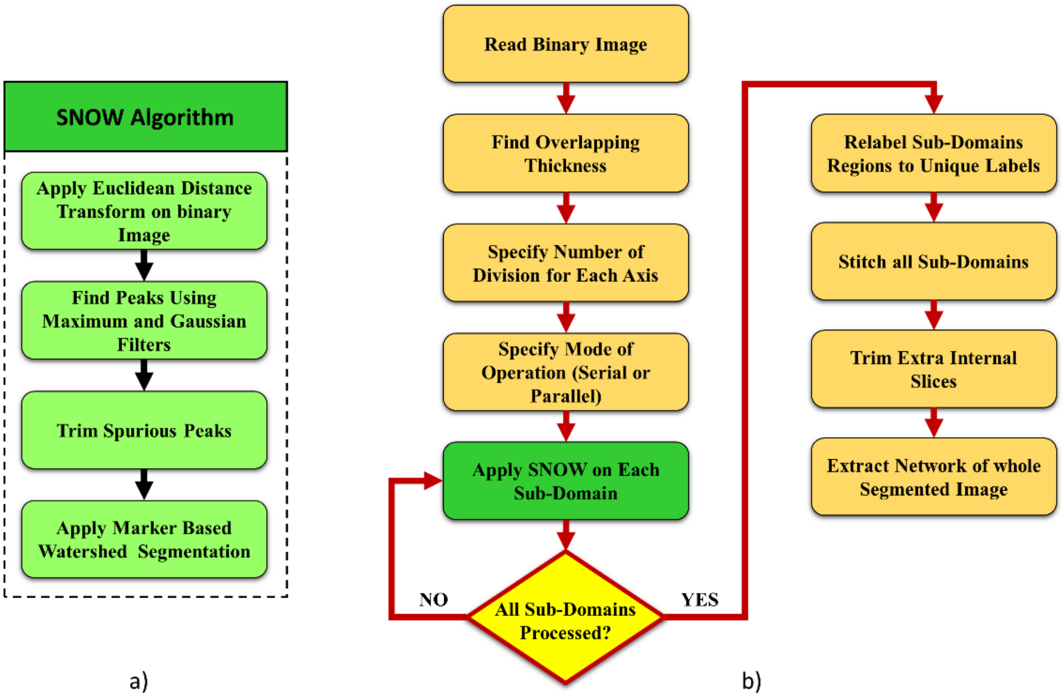

Figure 5.1 a) Basic steps of SNOW algorithm, b) Basic workflow of the domain decomposition algorithm

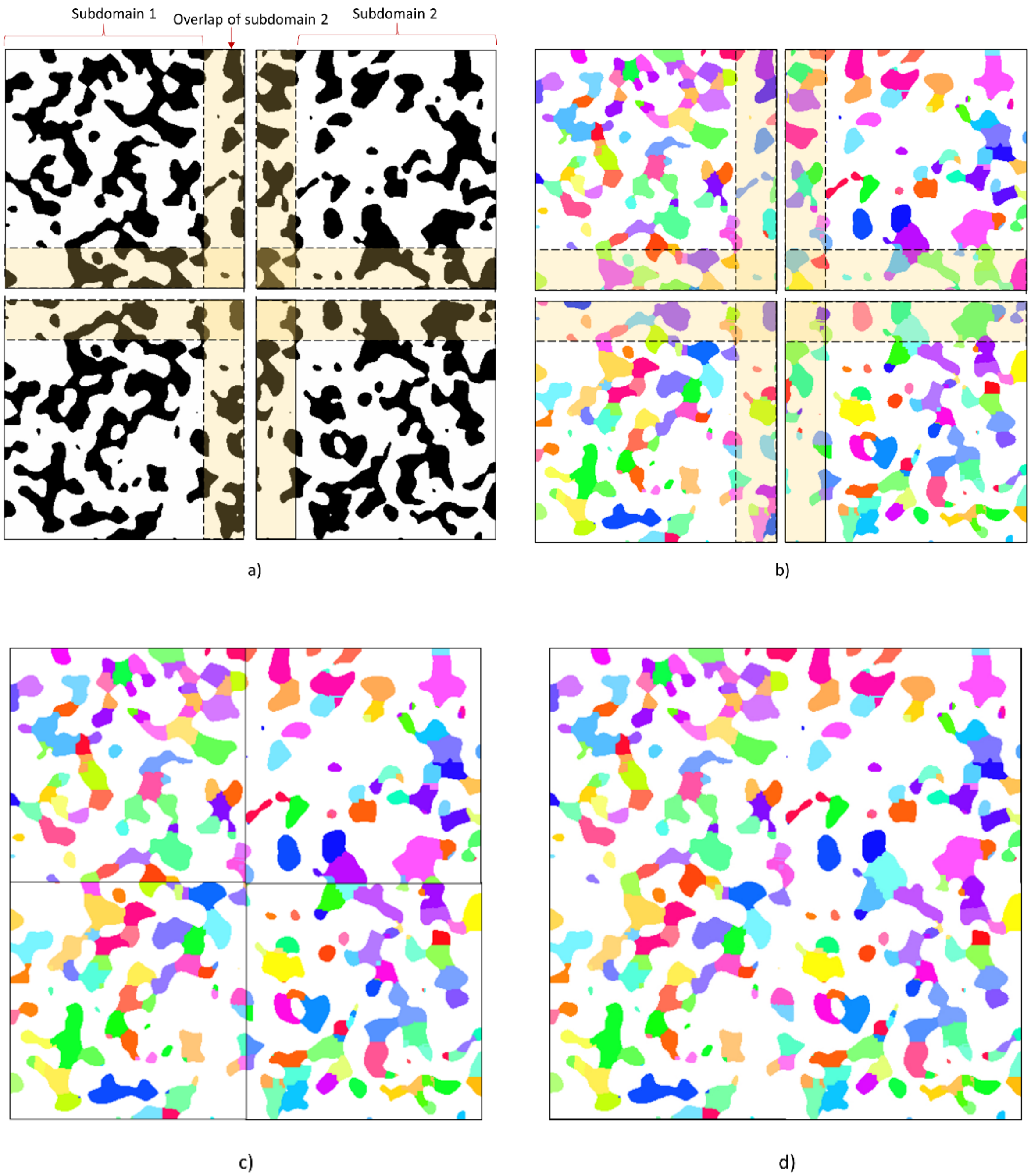

Figure 5.2 a) Binary Image decomposed into four subdomains where each subdomain has some overlapping part of neighbouring subdomains. The overlapping thickness part is shown as a golden colour band, b) Watershed segmentation of each subdomain after applying SNOW algorithm, c) Extra slice are trimmed after extracting labelling information from twin slices, d) Final Watershed segmentation after the stitching process

5.4.3. **Domain Decomposition Algorithm**

The main computational bottleneck of the SNOW network extraction algorithm Figure 5.1a. As the size of the image increases, overall memory and CPU time increases significantly, to the point that it becomes impractical to extract a network on a common laptop or desktop computer which has on average 16 to 24 GB RAM. The high computational cost of this step can be avoided if the image is divided into smaller, manageable sub-domains and watershed segmentation is performed on each individually. These sub-domains can then later be stitched together before the network extraction step. If this stitching is done carefully, it is possible to get an identical pore network to that which would be obtained from applying the watershed on the single large domain. The overall process for domain decomposition developed in this study is shown in Figure 5.1b. The algorithm is implemented in Python using highly optimized and efficient python packages that can handle large size image data sets such as Dask [139] and Numba [140]. The source code is included in the PoreSpy "networks" module as snow_partitioning_parallel. Figure 5.2a to d shows essential steps of algorithm implementation on a 2D slice of a 3D porous material dataset. The step by step description of the workflow shown in Figure 5.1 and Figure 5.2 is as follows:

5.4.3.1. Overlapping Thickness

The image is first divided into smaller sub-domains, such that each sub-domain has some overlapping parts in neighbouring sub-domains. Overlapping is essential to avoid edge artefacts when stitching the result back together but determining the amount of overlap is challenging. The calculation criteria for estimating the overlapping thickness is based on the fact that it should be equal to (or slightly greater than) the size of the largest region in the image, or more precisely the largest region touching subdomain boundary. However, regions are not available for inspection until *after* the segmentation, so a proxy metric must be used, such as the largest pore as well be described below. Figure 5.3a shows a 2D slice of random sphere packing image which is divided into two sub-domains. To get the correct watershed segmentation of each sub-domain, the boundary of each must be extended into the neighbouring sub-domains such that it contains the maximum diameter sphere or at least centre marker of the sphere as shown in Figure 5.3b. This thickness can be determined in one of two ways. The simplest is finding the maximum value in the distance transform[1] of the binary image Figure 5.3c since the distance transform must be calculated anyway as input to the watershed segmentation. The overlap should then be 2x higher than this value to ensure that the if the largest pores happen to lie on a divisional boundary it will be completely encapsulated in both chunks and its watershed basin will be present in both subdomains. This approach may fail if the pore regions are elongated since the distance transform gives only the shortest dimension of a pore region. Alternatively, the overlap size can be approximated by scaling down the image size by a factor of 2 or more, then performing a watershed on the coarsened image. Although this loss of resolution degrades the watershed, the point is to find the largest region which will be the least impacted. The amount of overlap can then be found as the largest dimension of a bounding box around the largest region, as shown in Figure 5.3d. If the material is anisotropic the second approach is recommended despite being more complicated, but in this work, the first approach is used throughout. Naturally increasing the size of the overlap also increases the computational costs since the overlapped regions are effectively processed because since they appear in both subdomains. Strategies for reducing the overlap are discussed and compared later.

---

[1] Note that the distance transform step can also be somewhat time consuming, but a recently released python implementation of [193,194] has drastically improved both the time and the RAM required compard to the native Scipy implementation [138].

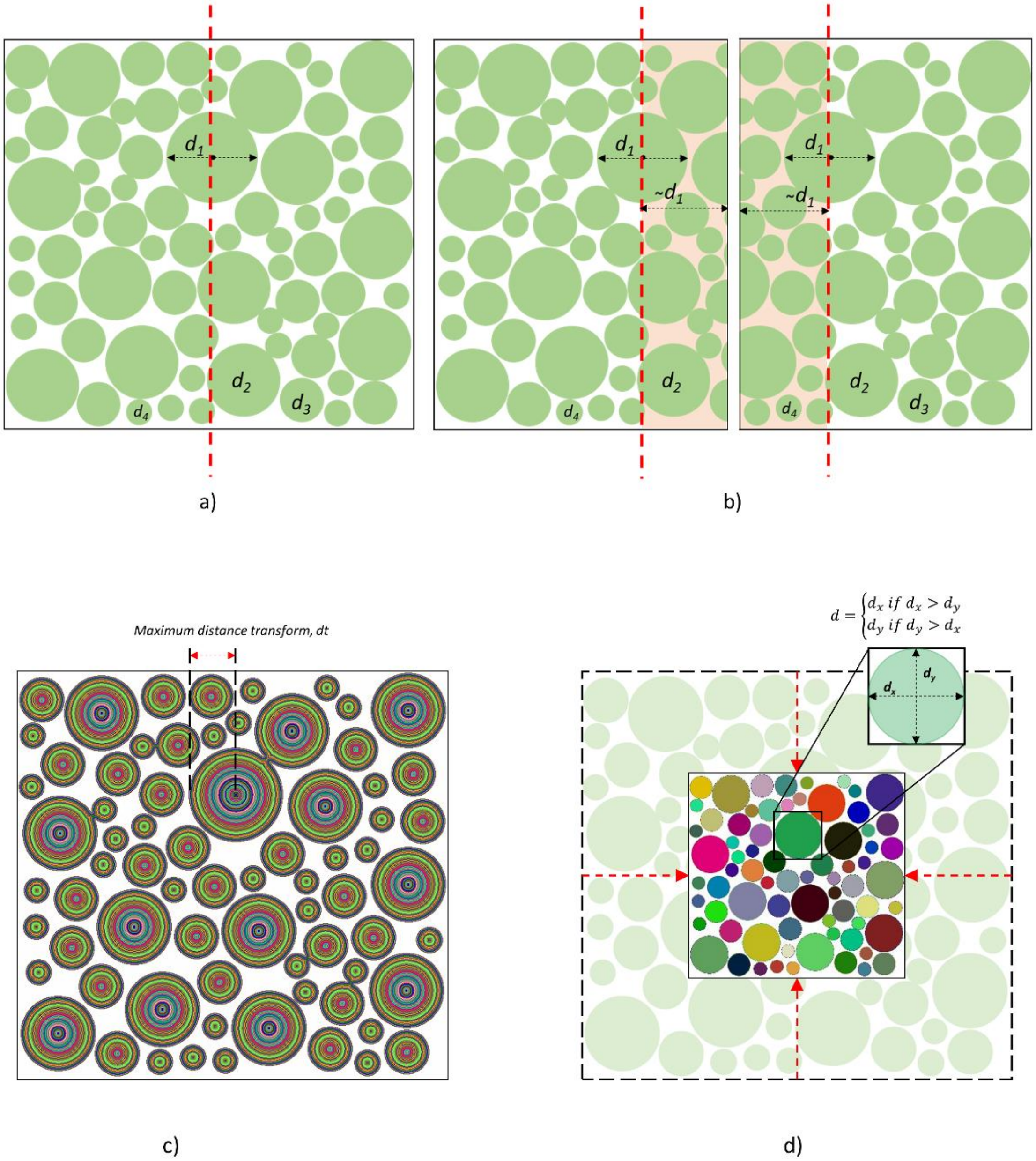

a)

b)

c)

d)

Figure 5.3 a) 2D slice of polydisperse sphere packing having four different diameter beads. The red dotted line indicates division slice, b) The two subdomains obtained after division with overlapping part of neighbouring subdomain having a thickness of slightly greater than d1, c) Euclidean distance transform of the 2D slice of sphere packing where dt indicates the value of maximum distance transform that is used to find overlapping thickness using first approach, d) The SNOW algorithm is applied on the scaled-down image of sphere packing to get the size of the maximum dimension of the bounding box of the largest segmented region

5.4.3.2. Number of Divisions

This number of subdomains created from the binary image can be adjusted depending on the computational resources available, either to utilize all the cores available or to minimize the amount of RAM consumed. If the image size in any axis is not evenly divisible by the desired number of division then the image must be cropped accordingly or else the algorithm can give erroneous results in current form of implementation. This limitation is due to the difficulty in getting the access of extra slices of subdomains during stitching process as explained in section 5.4.3.5 but was deemed acceptable given that at most 9 voxels would be sacrificed and the images are implicitly very large image. Future enhancement in the algorithm will address this more precisely. The size of subdomains at this step does not include the overlapping thickness, which is added after the numbers of divisions are specified. Also, it should be noted if the size of the overlap should not exceed the size of the subdomains, so there is an upper limit to how finely the domain can be decomposed. This essentially defines the upper limit of subdivision and caution the user not to provide very large numbers of division.

5.4.3.3. Modes of Operation

Once the extended subdomains are created the algorithm can be run in either parallel or serial mode. In the parallel mode of operation, each subdomain is processed in one core of the CPU. The serial mode of operation processes subdomains one by one and utilizes only one core of CPU. This reduces the RAM usage to a great extent but computational time increases compared to the standard watershed on the entire image. Overall computational performance graphs are discussed in detail in the Results and Discussion section 5.5.2.

5.4.3.4. SNOW Algorithm on Subdomains

After selecting the mode of operation, the SNOW algorithm is applied to each extended subdomain. This step is performed in a for-loop until all subdomains are processed. The output is a list of watershed segmentation of each extended subdomain Figure 5.2b. At this point, the overlapping thickness of each subdomain is trimmed such that only a 1-voxel thick slice of neighbouring subdomains is kept Figure 5.2c. This extra slice is essential for the stitching operation as detailed in section 5.4.3.5. Furthermore, the watershed basins in the subdomains are relabeled by sequentially finding the maximum label in the first subdomain in the list and adding that number to the labels of the next, and so on. This step ensures that there will be no duplicate labels in the final recomposed image.

5.4.3.5. Subdomains Stitching

After the relabeling process, subdomains are stitched with neighbouring subdomains using the information embedded in the extra slice associated with each neighbouring subdomain Figure 5.2d. Since the last slice of each subdomain and the first slice in the neighbouring subdomain are twins, they should have the same number of regions or in other words, the regions should coincide with each other. Also, the two slices will have an equal number of voxels in all twin regions if the overlapped thickness was sufficient. Once these conditions are met the region labels of the extra slice are used to replace the twin region labels in the neighbouring subdomains. The stitching process is performed along one axis at a time to avoid incorrect relabeling of regions in the corners and edges of the subdomains because these regions can have some part in more than two neighbouring subdomains.

5.4.3.6. Trim Extra Slices

Once the relabeling process is completed for all the subdivisions, the extra slices in each subdomain are deleted and the subdomains are recomposed into a single large image. The output of this step is a segmented image that has the same shape as the original input binary image. The segmented image labels are then sequenced to ensure they are contiguous since some labels are missing after the relabeling step. Also, region labels are spatially randomized such that neighbouring regions have significantly different values which aid visualization of the porous domain.

5.4.3.7. Pore Network Extraction

The segmented image is used to extract a pore network using PoreSpy built-in "regions_to_network" function which scans through all regions in the segmented image and extracts geometrical and structural features of pores and throats. The extraction process and definition of geometrical features are thoroughly explained in [97]. In addition to extracting the pore network, the algorithm can create boundary pores to define boundary conditions during the simulation process. The detail of creating boundary pores is discussed by [145].

5.4.4. Random Walker Simulation

All of the rock images investigated here have reported values for the permeability coefficient which can be compared to value predicted the extracted network. It was also desired to compare tortuosity or formation factors values, which are not as readily available. To remedy this the effective diffusivity of the images was estimated by discrete random walker simulation. This approach is far less computationally expensive than DNS simulations (e.g. such as the commonly used Lattice Boltzmann method [146,147]. While dealing with large size image datasets DNS require the use of a supercomputer which is contrary to the aims of the present study.

An open-source Python package PyTrax [148] was used to perform random walker simulation. A comparison of the computational efficiency of the algorithm with LBM was given by [145]. The random walker algorithm finds the pore phase tortuosity of the binary porous domain using mean square displacement (MSD) (10^5 random walkers were used). Equation 5.1 was used to find MSD, where $p(x,t)$ represents the probability density function of a walker at location x and time t [149] and can be described by equation 5.2.

$$MSD = \int_{-\infty}^{\infty} x^2 p(x,t)dx \qquad 5.1$$

$$p(x,t) = \frac{1}{4\pi Dt} \exp\left(\frac{-x^2}{\sqrt{4Dt}}\right) \qquad 5.2$$

The mean square displacement (MSD) of a walker that is subjected to follow an unbiased movement traces a Gaussian Distribution. The touristy factor τ^{-1} can be found by plotting gradient of MSD over time t. The tortuosity τ calculated can be used to find the formation factor of the porous domain of porosity ε according to [150]. The formation factor in defined as the ratio of effective diffusivity to bulk diffusivity of nitrogen gas in air (2.03x10^{-5} m^2/s [151]) and calculated according to equation 5.3 as follows.

$$\frac{D_{eff}}{D_{bulk}} = \frac{\varepsilon}{\tau} \qquad 5.3$$

5.5. Results and Discussion

5.5.1. Algorithm Validation

The validation of the domain decomposition algorithm was performed on five different types of 3D images (ID: 1-5) mentioned in Table 5.1. The number of segmented regions with and without domain decomposition was counted to ensure no regions were created or lost at the intersection of subdomains. The decomposition ratio, defined as the ratio of the shape of the original image to the shape of the subdomain, was varied from 2 to 4 to ensure algorithm robustness. At decomposition ratio 3 it was necessary to crop the image slightly to perfectly divide it into equal size subdomains. The results are summarized in Table 5.2 and show that the domain decomposition algorithm returns an identical number of segmented regions as compared to the segmentation without domain decomposition. The small differences in a few cases (never more than 2 regions) are due to the size of the structuring element in the peak trimming method of SNOW algorithm and not associated with domain decomposition algorithm. Further improvements of the peak detection method can remove this difference but overall, it represents a very small error considering the number of regions in the images. These results also indicate robustness for different materials, indicating that it can be used on other different types of porous domains such as metallic foams [152], membranes [153], and battery electrodes [116].

Table 5.2 Algorithm Validation

Name of Sample	Dimensions [x, y, z]	Number of Segmented Regions			
		Without Domain Decomposition	*With Domain Decomposition*		
		**dr = 1*	*dr = 2*	*dr = 3*	*dr = 4*
Berea	1024, 1024, 1024	33041	33042	-	33045
Berea	1023, 1023, 1023	32942	-	32943	-
Bentheimer	1000, 1000, 1000	20779	20779	-	20780
Bentheimer	999, 999, 999	20723	-	20723	-
Doddington	1000, 1000, 1000	10172	10172	-	10174
Doddington	999, 999, 999	10144	-	10145	-
Ketton	1000, 1000, 1000	6976	6976	-	6977
Ketton	999, 999, 999	6948	-	6948	-
Random Sphere Packing	520, 520, 520	3399	3400	-	3402
Random Sphere Packing	519, 519, 519	3402	-	3404	-

5.5.2. Quantification of Computational Performance

To analyze CPU time and memory usage of the domain decomposition algorithm, two different large size 3D images samples of sandstones were used in the study. The specifications of the images (ID: 6,7) are shown in Table 5.1. The CPU time was defined as time required to execute all code including preprocessing and postprocessing steps such as calculating overlap thickness, relabeling and stitching etc. To measure computational performance with increasing numbers of voxels, the images were divided into 16 different size samples such that each sample size was obtained by dividing the z-axis of the original image with an integer n between 1 to 16. The algorithm was tested on Lenovo ThinkStation P500 WorkStation, having E5-1650 V3.3 CPU, 16 cores and 256 GB RAM. During parallel and series computation the input samples were subdivided only along the z-axis and no subdivision was performed in y and z-axis so that the number of overlapping voxels scaled proportionally to the number of divisions. For serial operation, each subdomain was processed in a single-core one by one while in parallel operation all subdomains were simultaneously processed in the separate cores. The computational results were also compared with the legacy SNOW algorithm that uses SciPy [138] implementation of watershed segmentation. The CPU time and memory usage are plotted against the number of voxels and results are shown in Figure 5.4a and b respectively. From Figure 5.4a It can be seen that SNOW parallel is significantly faster than SNOW legacy and as the number of voxels increases the computational efficiency increases many folds. In the case when the actual images of Bentheimer sandstone are subdivided into 16 domains, SNOW parallel is 7 times faster than SNOW legacy. This shows an appreciable increase in computational performance.

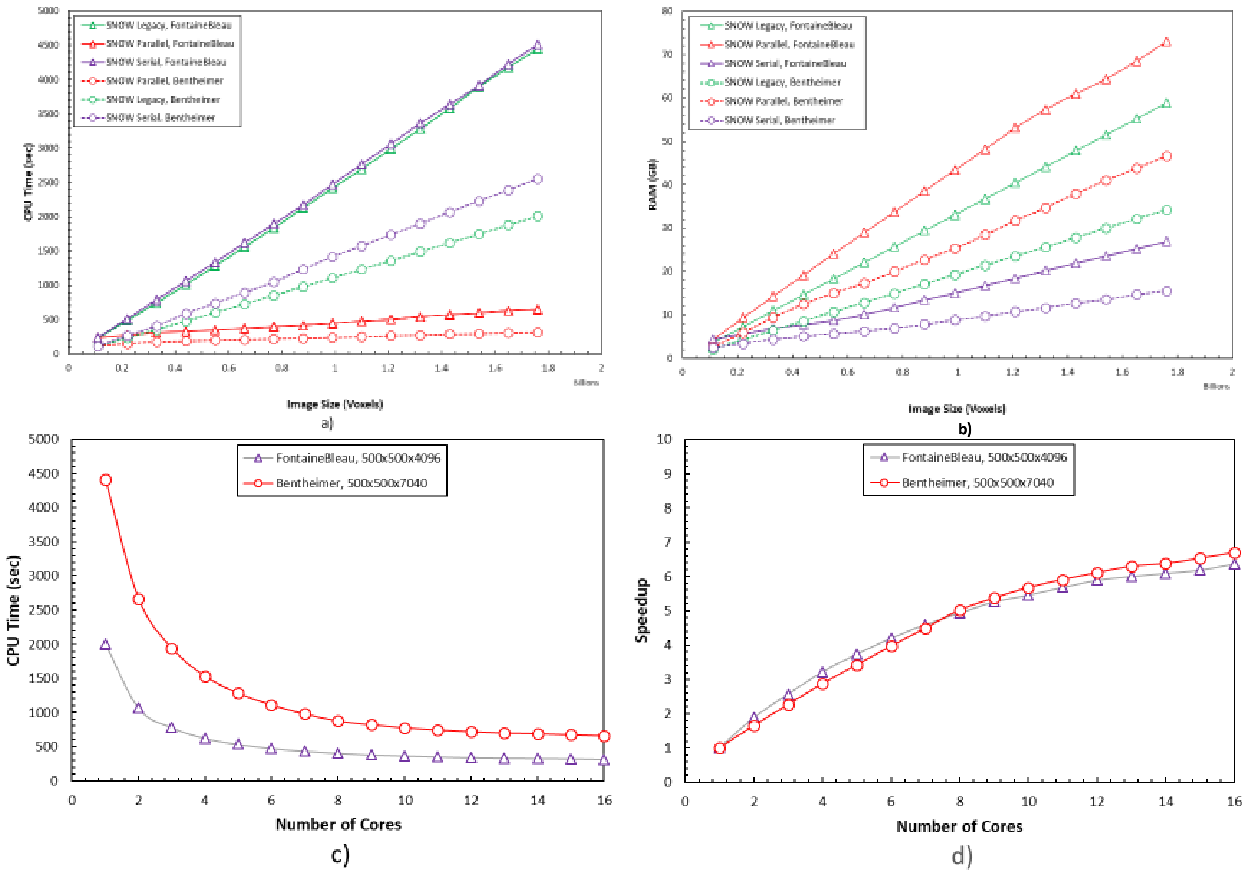

Figure 5.4 a) CPU time comparison of the algorithm with varying voxel numbers, b) RAM usage comparison of the algorithm with increasing domain size, c) Computation time with increasing number of cores for two different rock samples d) Speedup gained due to parallelization against number of cores

Figure 5.4c and d shows CPU time performance and speed up gains against number of cores without changing number of voxels in samples. The speedup in the simulation was defined as the ratio of CPU time without domain decomposition to the CPU time required by N cores with domain decomposition. From Figure 5.4c and d it can be seen that total computational time decreased to approximately 7 times as compared to single-core simulation. In principle dividing the image into 16 subdomains with no overlap should give 16x speedup, neglecting the time of any preprocessing and postprocessing steps such as overlap calculation, relabeling and stitching. In practice, this was found to only result in a 10x speed-up, presumably due to overhead of the parallelization and data i/o between the CPUs and RAM. However, some overlap is necessary for the algorithm to stitch the subdomains together, and this overlap is responsible for reducing the speed-up from 10x to 7x. Section 5.5.4 investigates the impact of the overlap size on speed and memory usages, as well as segmentation accuracy.

Figure 5.4also shows that SNOW serial is relatively slower than SNOW legacy. From Figure 5.4a it appears that SNOW serial implementation is approximately 1.5% and 30% slower than SNOW legacy in Bentheimer and Fontainebleau sample respectively but the major advantage of this mode of operation is significant reduction in RAM usage as shown in Figure 5.4b. SNOW serial uses 2x less RAM than SNOW legacy for equivalent size domains in both samples. This allows a user with average computational resources to extract relatively bigger porous domains which were not possible with SNOW legacy. Also, it should be noted that SNOW parallel consumes more RAM than the legacy SNOW algorithm. This is because during the domain decomposition process SNOW algorithm is applied on all the subdomains simultaneously, adding up RAM usage of all subdomains together. This limits the choice of the user to perform SNOW parallel on a workstation having low computational memory resources.

5.5.3. Pore Network Extraction of Large Size Tomograms

The domain decomposition algorithm was applied to four large size tomograms of porous rocks (ID: 1,2,3,7). The sizes of these tomograms are given in Table 5.1. The decomposition ratio of 4 was used to extract the pore network from Berea, Bentheimer, and Doddington sandstone while the domain decomposition ratio was set to 6 for Fontainebleau image of size 2048^3 voxel. The extracted pore networks were used to simulate directional effective permeabilities for single-phase flow using steady-state Stokes flow. The pore network model conduit was assumed to consists of two half pores (i and j) and their interconnecting throat, k. To find sizes of each half pore and interconnecting throat, spherical and cylindrical geometries were used respectively. The overall conductance of conduit was calculated using series resistor model:

$$\frac{1}{g_{ij}} = \frac{1}{g_{ik}} + \frac{1}{g_k} + \frac{1}{g_{jk}} \qquad 5.4$$

where conductance in each half pore and interconnecting throat is calculated using Hagen Poiseuille equation as:

$$g_N = \frac{A_N^2}{8\pi\mu L} \qquad N \rightarrow i, j, k \qquad 5.5$$

Figure 5.5 to Figure 5.7 shows overplayed pore network of the porous domain, pore size colour map and z-axis pressure field in the extracted pore network for Berea, Bentheimer and Doddington sandstone. The large size Fontainebleau overlaid pore network, pore sizes and pressure field are shown in Figure 5.8. The results of effective permeabilities for single-phase flow in each direction are shown in Table 5.3. The average values of permeabilities were compared with previously reported results in [141,154–156]. It can be seen that the results estimated by the presented algorithm match well with other efforts but with far less computational cost than the previously adopted computational approaches.

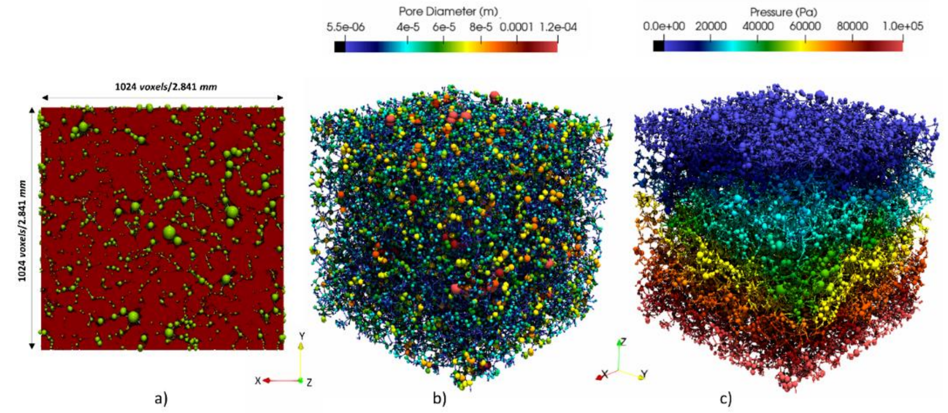

Figure 5.5a) Berea Sandstone with pore network overlayed on pores of voxel image, b) Extracted pore network using domain decomposition ratio to 4. The network shows pore size distribution in porous rock, c) Single phase flow simulated in the z-axis direction

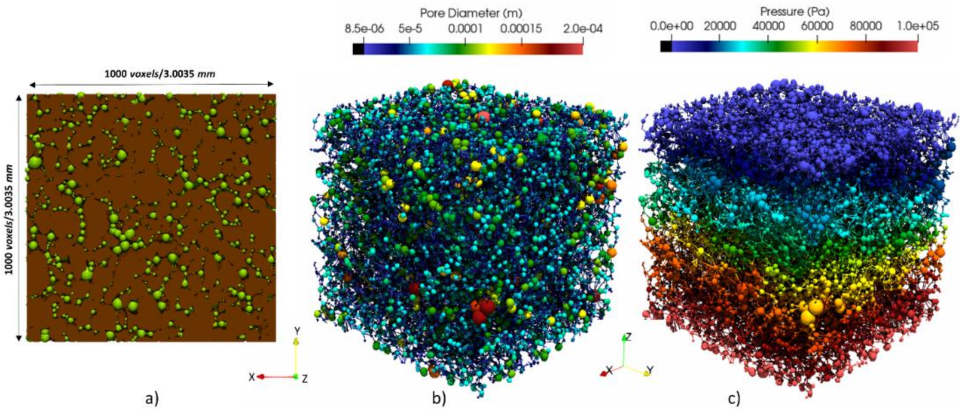

Figure 5.6 a) Bentheimer Sandstone with pore network overlayed on pores of voxel image, b) Extracted pore network using domain decomposition ratio to 4. The network shows pore size distribution in porous rock, c) Single phase flow simulated in the z-axis direction

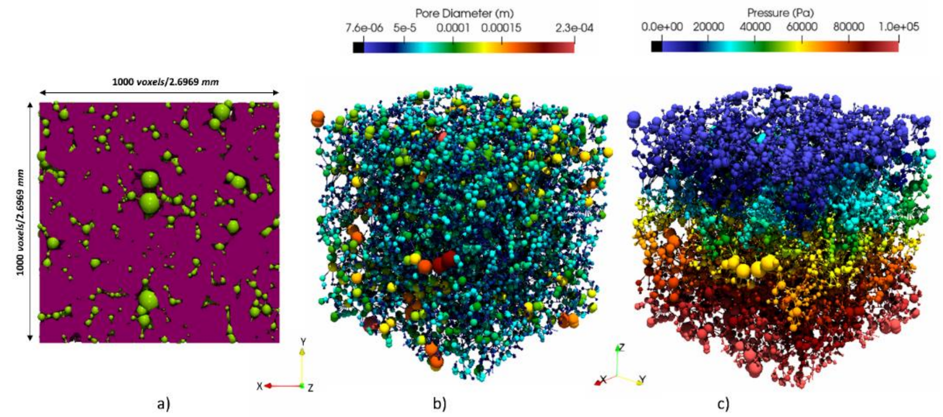

Figure 5.7a) Doddington rock with pore network overlayed on pores of voxel image, b) Extracted pore network using domain decomposition ratio to 4. The network shows pore size distribution in porous rock, c) Single phase flow simulated in the z-axis direction

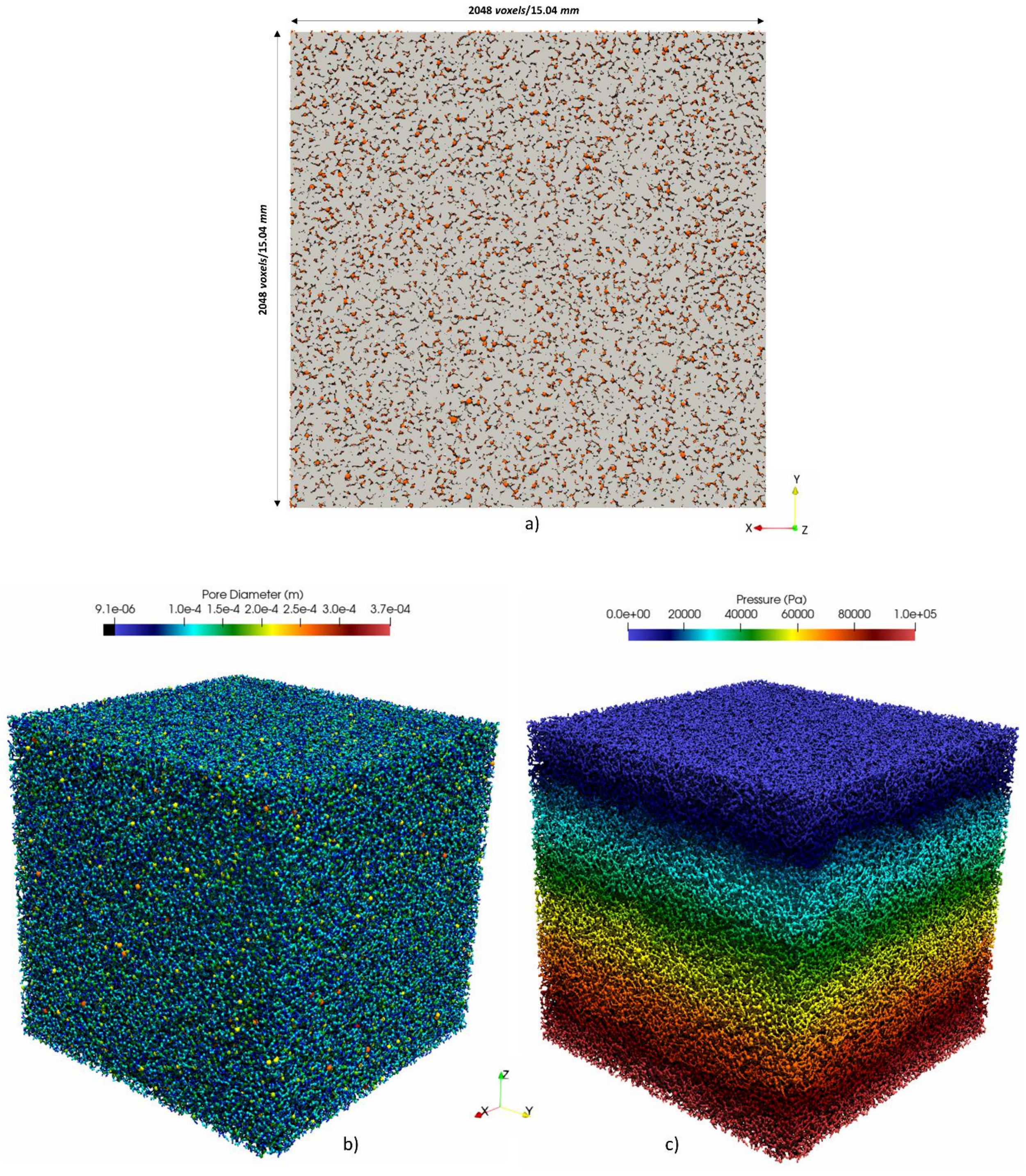

Figure 5.8 a) FontaineBleau rock with pore network overlayed on pores of voxel image, b) Extracted pore network using domain decomposition ratio to 4. The network shows pore size distribution in porous rock, c) Single phase flow simulated in the z-axis direction

5.5.4. Impact of Overlap Thickness on Speed and Accuracy

The overlapping of the subdomains represents a computational inefficiency since these voxels are processed multiple times. In all of the results shown elsewhere in this work, the amount of overlap was conservatively estimated by finding the global maximum of the distance transform. A study was performed to determine the impact that reducing or increasing this overlap could have on computational time, RAM usage and accuracy. A 1024^3 image of Berea sandstone (ID: 1) was used and divided into 8 cubic subdomains. The standard overlap thickness calculated using distance transform approach was 58 voxels and represented as dashed vertical line in Figure 5.11. Figure 5.11(b) shows that a 20% reduction in computational time and RAM usage can be obtained by reducing the overlap from 58 to 20. Intriguingly, Figure 5.11(a) shows that the number of regions obtained by the watershed is nearly stable above 20 voxels of overlap. Similarly, Figure 5.11(c) shows that the permeability and tortuosity of the extracted networks are unaffected by the reduced overlap size above 20 voxels. Unfortunately, there is a sudden and drastic reduction in the accuracy of the results below 20 voxels, creating a precarious situation. The value of 20 voxels presumably depends on the sample morphology and pore size, and image resolution. Further investigation of this lower limit should be considered in future work. The substantial gains in performance do suggest that a safe but less conservative estimate of overlap should be found. One possibility is to calculate the local thickness of a down sampled image, then the values only along the subdomain boundaries could be scanned for a *local* maximum. This would in all probability provide a smaller value for the overlap that would still be sufficient. The present implementation only allows for a single value of overlap thickness for all subdomains, but this local approach would provide estimates for each pair of neighbouring domains, in principle allowing the smallest possible subdomains to be analyzed. Such optimizations are left for future studies.

5.5.5. Pore Network Extraction of Scaled Up Images

Since domain decomposition saves the computational cost of network extraction, it can be used to perform a pore network extraction on a scaled-up image with almost the same amount of computational power that would have been consumed on a relatively small size domain using SNOW legacy. The importance of image resolution enhancement has been discussed in [157,158].To illustrate this advantage, the effective diffusivity results of three different samples of the same porous domain were analyzed at a different level of image resolution. Firstly, a large high-resolution image was used, next the high-resolution image was scaled down by a factor of 2 (by binning the image) to artificially reduce its resolution, and lastly the artificially reduced image scaled-up the size of the actual original high-resolution binary image using a nearest-neighbour interpolation (note that higher-order interpolations may provide even better results, but this detail was left for future work). Pore network extraction on all three images was performed using the presented domain decomposition algorithm. This process was applied to five different types of porous image (ID: 1, 2, 3, 4 and 14) and the results of extracted pores number and effective diffusivities formation factor for all samples are shown in Figure 5.9 and Figure 5.10 respectively. The formation factors were calculated for each high-resolution image in all three directions using random walks and an average value is reported in Figure 5.10. From the results in Figure 5.9, it can be seen that like other extraction algorithms when the resolution is reduced, the number of regions found by the watershed is impacted (almost always reduced), which indicates that the watershed segmentation is indeed resolution-dependent. The reason low-resolution sample has fewer regions is that the fewer markers are found at low-resolution and hence marker-based watershed segmentation merges two or more regions into one. When low-resolution images are rescaled back up to the original size, the number of regions approaches very nearly back to the value found on the original high-resolution images. This is a very promising result since it suggests that natively low-resolution images can be artificially scaled-up to improve the accuracy of the segmentation and extraction. The trends seen for the number of regions are also echoed in the formation factor values predicted by the extracted networks, as can be seen in Figure 5.10(a-c) which reports the network formation factor for all samples at all resolutions, along with the results of the random walker simulation on the high-resolution image as a reference (indicated by the line). This indicates that increasing the resolution of a natively low-resolution image not only improves the watershed segmentation but simultaneously improves the accuracy of the extracted network. The impact of resolution on watershed segmentation and the accuracy of the subsequently extracted networks is worth deeper study. For instance, the resolution effect was almost absent from the sphere pack shown in Figure 5.10 d and e. This effect is probably due to the fact that sphere packs have a narrow pore size distribution, whereas the natural material has a wider distribution and the smaller pore are probably not well segmented. In any case, the outcome of this sub-study is that instead of reducing an image to a manageable size before network extraction, it is now possible (and recommended) to enlarge the image before extraction.

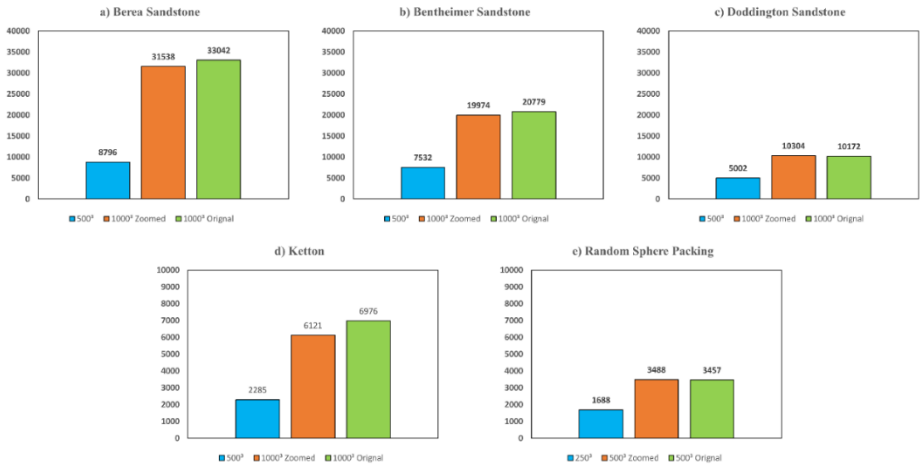

Figure 5.9 Number of segmented regions obtained from three samples of different resolution. The blue bar represents the number of regions in a low-resolution image of the dataset, the brown bar represents the number of regions of scaled-up dataset and green bar represent no of regions in the original dataset

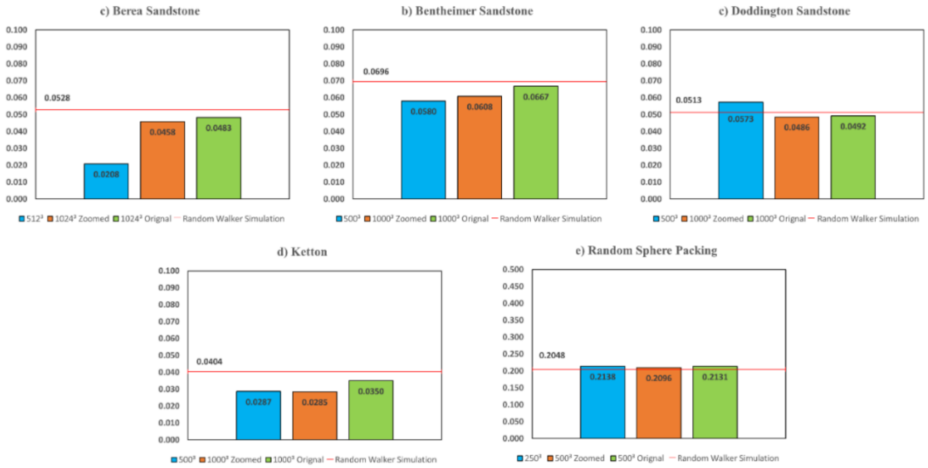

Figure 5.10 Comparison of the formation factor values of three sample with the random walker simulation result

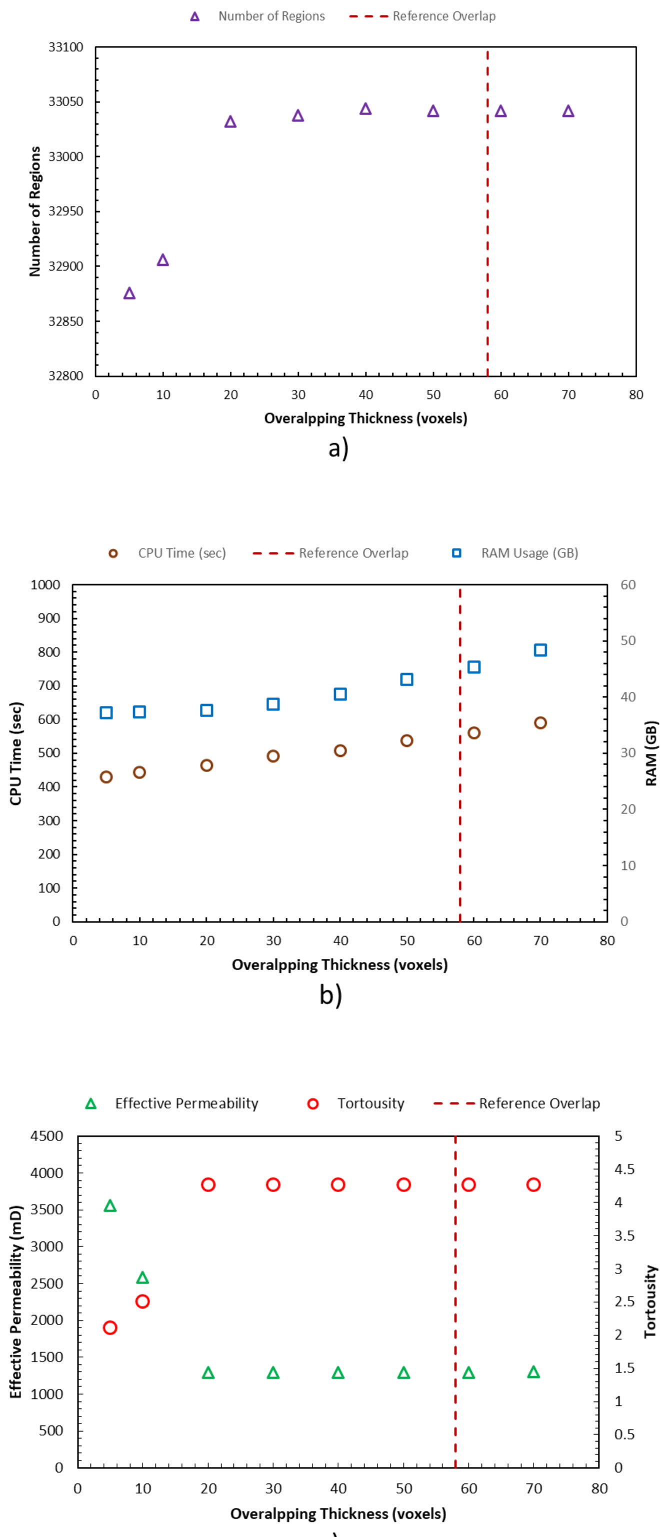

a)

b)

c)

Figure 5.11 Effect of overlapping thickness on pore network extraction a) Number of segmented regions obtained after watershed segmentation b) CPU time and RAM usage at different overlapping thickness c) Effective permeability and tortuosity variation at different overlapping thickness

Table 5.3 Effective Permeability in different large size datasets of digital rocks

Sample	**Voxels**	**Porosity**	**Network Permeability (mD)**				**Image Permeability (mD)**
			x-axis	***y-axis***	***z-axis***	***Average***	
Berea	1024^3	20.25	1177	1410	1304	1297	[942-1286] [141]
Bentheimer	1000^3	21.67	2723	3351	3202	3092	[2800-3547] [155,159]
Doddington	1000^3	19.58	2795	3382	3383	3187	[1900-3500] [154,159]
Fontainebleau	2048^3	14.23	782	793	791	789	628-942 [156]

5.6. Conclusions and Future Work

An efficient geometric domain decomposition algorithm was developed to extract pore network from massive size images of porous domains. The algorithm subdivides the image into small subdomains with sufficient overlap, and these are further processed to get watershed segmentation using the SNOW algorithm. Validation of the algorithm was performed on various different types of porous materials and found to give identical results, in terms of number of watershed basins found, to that obtained without performing domain decomposition. One key feature of the proposed decomposition approach is that it can be applied to all subdomains in parallel for enhanced speed, or each one in serial for reduced RAM usage. The serial mode of operation reduces RAM usage to 50 percent compared to the legacy approach, This allows a user to process large porous domains on a computer with average computational capacity. On the other hand, the parallel mode of operation decreases CPU time by 7 times in the tested image, enabling the processing of larger domains much faster than the legacy method.

Typically images are often scaled-down to more manageable sizes before processing. Due to the improved performance of the proposed algorithm, it becomes feasible to process larger images. A study was performed to see if artificially increasing the size of a low-resolution image resulted in improved outcomes. The pore network extracted from a scaled-up domain was found to give more accurate results than those obtained from a low-resolution image, and the results approached those of the original high-resolution image.

The developed algorithm is implemented in the open-source Python package PoreSpy using highly optimized and efficient python packages such as Dask and Numba. There are improvements that could be made to the proposed algorithm. For instance, the Dask library is able to parallelize across distributed nodes as well as the shared-memory approach used here, which could enable the segmentation of even larger images.

Chapter 6 Multiphysics Pore Network Modelling of Lithium-Ion Battery Cathodes

6.1. Preface

In this manuscript, a pore network modelling framework was developed to relate structural heterogeneities of porous cathodes with half cell performance of lithium-ion battery. The model was validated with experimental data by simulating discharge curves at different C-rates. The framework was used to perform various structural analysis on two different three phase cathodes. The results revealed important insights to understand structural – performance relationship inside porous cathodes and opened up a new avenue to study and optimize battery electrodes microstructure without performing expensive and time-consuming experiments and simulations in the lab.

6.2. Overview

The performance of lithium-Ion batteries (LIB's) strongly depends on 3D microstructure and substantial research is needed for the development and optimization of electrode design that can operate under wide range of operating conditions. In this work, a novel pore network modelling approach is used to understand structural performance relationship of porous cathodes of LIB's. It was demonstrated that PNMs can efficiently predict the rate-dependent capacity of an electrode using only a 3-phase tomogram as input. The developed modelling framework was used to perform structural analysis on two $Li(Ni_{0.5}Mn_{0.3}Co_{0.2})O_2$ (NMC532) cathodes of different thickness and calendaring pressure and revealed important insights of microstructural heterogeneities inside porous structures. Three-phase networks were extracted from X-ray tomography images and pore network modelling approach was used to simulate galvanostatic discharge behaviour of LIB half cell at different C rates. The developed model was used to analyze spatial distribution of concentration, potential and state of lithiation in electrolyte, active material and carbon binder domain and unveiled the dependence of LIB performance on microstructural heterogeneities especially at high C-rate. Lastly, the computational performance of pore network model was analyzed at different C-rates for both electrodes. The results revealed decent improvement in computational performance without compromising on the size of domain. The novel modelling framework reported in this study has enabled user to study local heterogeneities in other types of cathode material to propose next-generation electrode design. Also, in-silico structures that vary arbitrary properties of the electrode, could be produced and screened for performance using PNMs, avoiding the need to perform expensive and time-consuming cell fabrication and testing in the lab.

6.3. Introduction

Lithium-Ion Batteries (LIB) are currently the best available power source for consumer electronics and electric vehicles manufacturing industry due to their high energy and power density as compared to other energy storage devices [160]. However, increasing energy density, lowering cost, and extending life remains essential for broader adoption, especially in transportation. Many options for cathode materials are available, but lithium iron phosphate (LFP) and lithium manganese nickel cobalt oxide (NMC) are the most widely used commercially because of their relative high capacity and reduced price [161–163]. Beside material selection, optimization of electrode microstructure can greatly enhance the transport and reaction processes and thus improve the overall performance of LIB's. For this purpose mathematical modelling can play a vital role to understand the structural – performance relationship of porous electrodes[105,164,165].

A multitude of mathematical model investigating physical and electrochemical processes of LIB's have been developed in the past [166–169], however, most of them either considered porous electrodes as homogenous structures (volume averaged) or incorporated structural heterogeneities using empirical relationships. The most famous pseudo two dimensional (P2D) model based on porous electrode and concentrated solution theory was developed by Newman and co-workers [167,170]. Their model simulates the intercalation/deintercalation process by assuming active material as equal size, isotropic spherical particles and estimates the effective transport properties using Bruggeman expression whose accuracy for non-spherical geometries is still controversial [22]. Although the simplifications of P2D model do not capture the real microstructure, it is still the standard modeling approach in the battery research due to ease of usage. On the other hand, some attempts have been made to extend the capabilities of P2D model by incorporating microstructural effects but due to additional complexity the computational cost increased many fold, becoming infeasible to model large domains with normal computational resources [104,171]. Therefore, to properly understand the impact of microstructure in LIB models, it is necessary to develop a computationally efficient framework, yet captures the structural heterogeneities of porous components of LIB cell.

Pore network modelling (PNM) is a computationally efficient technique that is used to simulate transport at the pore-scale, preserving structural heterogeneities of porous material [172,173], at low computational cost. The technique uses a simplified geometric representation of real porous structures by treating the pore space as a network, where cavities or pores are the nodes and they are interconnected by constrictions or throats. Each pore is considered as a well-mixed body that exchanges species with its neighbouring pore bodies via the network connections. These networks are extracted from X-ray tomography (XCT) images of real porous materials via different types of network extraction algorithms [28,174,175]. Recently, PNM models have shown their utility to simulate electrochemical devices like fuel cells [175] and redox flow batteries [175] but to the best of our knowledge, they have not been applied to the active materials of lithium-ion battery during charging and/or discharging. PNMs are ideally suited for such microstructural modelling since the computational efficiency compensates for the high demands of transient multiphysics modelling. Their lack of adoption is likely due to the lack of an existing PNM code base capable of handling the various complexities of the problem, including the intercalation reaction, migration effects, and three intermixed phases (void, active material and carbon binder) that all must be captured.

Torayev et al. [91] developed a pore network model of super P carbon electrode of lithium-oxygen battery. The 3D network of pore phase was extracted to find the discharge behaviour of four different zones of same electrode tomography image. The results showed deviations of model results with experimental data due to the variation of pore interconnectivity in different zones. The model, however, does not incorporate the solid phase strucutural-performance relationship. Lagadec et al [176] highlighted the importance of pore interconnectivity in lithium-ion battery separator by comparing two different separators of same porosity and tortuosity but different pore interconnectivity. The results showed that concentration gradient due to diffusion for both separators varies although porosity and tortuosity correction of both structures were same. Khan et al. [116] developed a 3D pore network model of lithium-ion battery cathode from a full resolved XCT image of $Li(Ni_{0.8}Mn_{0.1}Co_{0.1})O_2$ (NMC811). The model highlighted the impact of treating carbon binder as separate phase. The PNM model was developed to simulate simple steady-state diffusion-reaction and diffusion conduction process in electrolyte and solid-phase respectively but did not analyze transient intercalation/ deintercalation process.

Several recent publications attempt to model the impact of microstructure using direct numerical simulation, despite the computational challenges. Chouchane et al. [177] simulated a 4D electrochemical model of LIB cathode using direct numerical simulation to investigate the spatial location of carbon binder domain on overall electrochemical performance of the battery. All three-phases of cathode were meshed as separate phases and pore size distribution were calculated using extracted pore network. The results showed changed in overall cell performance due to spatial variation in carbon binder domain (CBD). It was found that CBD without nanopores can lead to decrease in current density by increasing the tortuosity of pores. Due to DNS approach, the computational cost of the model was high. Lu et al. [2] recently, developed a fully resolved 3D microstructure model of NMC cathodes using XCT images and confirmed that LIB performance is indeed dependent on structural heterogeneities. They altered the particle size distribution to predict next-generation electrodes architecture. The model used DNS approach and did not include pore to pore analysis of concentration and potential distribution and used relatively small size domain for simulation. Therefore, due to this structural- performance dependence of porous cathode there is a need to develop a modelling framework that can simulate big porous domains without using too much computational resources.

In the present work, an existing pore network modelling framework (OpenPNM) was extended to study the galvanostatic discharge behaviour of lithium-ion battery half-cell. The model incorporated the three-phase network of $Li(Ni_{0.5}Mn_{0.3}Co_{0.2})O_2$ (NMC532) cathode material extracted from X-ray tomography images, using a multiphase network extraction technique recently developed [95,116,178]. The galvanostatic discharge behaviour of the two cathodes was then compared with experimental data and found to be in excellent agreement. Impressively, the PNM was able to predict capacity of both electrodes at various C-rates (between 0.2 and 3), using only imaging data to generate the model. Moreover, the relatively low computational time allowed modeling of relatively large domains, spanning the full thickness of a normal electrode, to capture the effect of structural heterogeneities in material. To the best of our knowledge, this is first transient pore network model of lithium-ion battery discharge and opens up a new avenue to study and optimize next-generation battery electrodes microstructures.

6.4. Modelling Approach

6.4.1. Cathode Samples

X-ray tomography images of two porous cathodes were obtained from open-source electrodes library of National Renewable Energy Laboratory (NREL)[10]. Both cathodes consist of $Li(Ni_{0.5}Mn_{0.3}Co_{0.2})O_2$ (NMC532, TODA America Inc.) as active material, C45 carbon (Timcal), polyvinylidene fluoride (PVDF) (Solvay, Solef 5130) as carbon and binder domain and 1.2 MLiPF6 in ethyl carbonate/ethyl methyl carbonate (EC:EMC, 3:7 w/w, Tomiyama, Japan) as electrolyte. The thickness of both electrodes was achieved by a multi-pass calendaring process with a constant but untracked applied force. The specifications of the two electrodes are listed in Table 6.1. Cathodes image segmentation containing two labels (0 and 1) were taken for analysis. Label 0 correspond to electrolyte and carbon binder domain (CBD) while label 1 corresponds to NMC532 active material particles. The CBD phase was added using morphological image closing transform to the image [179]. This technique was recently shown to be more suitable than other physics-based carbon binder models [180–182] as it only binds the contact points between active material particles. A detailed comparison can be seen in Hein at al [183]. The cathode domain sizes used in this study are larger than the representative element volume (REV) that was estimated to be 50 x 50 x 50 μm^3 [184]. The renderings of both cathodes after addition of CBD phase can be seen in Figure 6.1(a, i).

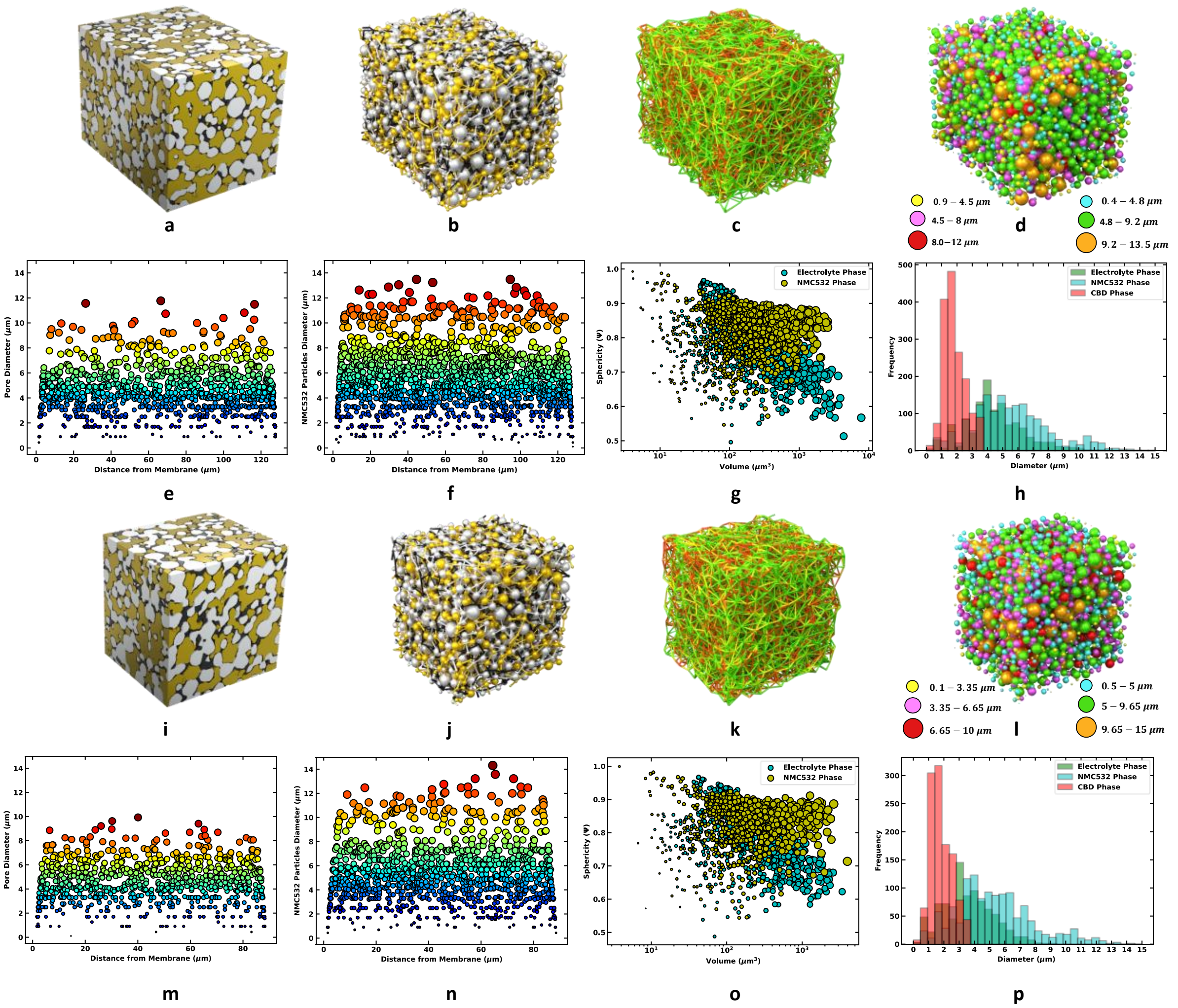

Figure 6.1(a, i) Three-phase rendering of 1CAL and 3CAL cathodes with golden, silver and black colour representing electrolyte, active material and CBD phase respectively, (b, j) Extracted networks of 1CAL and 3CAL respectively, (c, k) throat interconnection between two phases, green, yellow and red colour show interconnections between electrolyte-NMC532, electrolyte-CBD, NMC532-CBD respectively, (d, l) Size distribution of electrolyte and NMC532 phase. The sizes are classified into three categories. Yellow, pink and red colour represent electrolyte phase size distribution while cyan, green and copper represent particle size distribution in NMC532 phase, (e, m) Pore size distribution in the electrolyte phase of 1CAL and 3CAL with respect to distance from the separator, (f, n) Particle size distribution in NMC532 phase for 1CAL and 3CAL with respect to distance from the separator, (g, o) Sphericity vs Volume of pores particles in electrolyte and NMC532 phase, (h, g) Size Distribution comparison of all three phases in 1CAL and 3CAL.

6.4.2. Pore Network Extraction

The key to the following pore network modelling simulations presented herein was the extraction of three-phase networks from the tomograms. A watershed-based network extraction tool reported previously [28] was adapted to work on multiphase images [178], and it was confirmed that such networks could predict the effective transport properties in both the solid and void phase of NMC microstructures by comparing with direct numerical simulations [116]. Crucially, the extracted network contains interconnections between each pair of phases, which is necessary to simulate interphase mass transport and Li-ion intercalation between the electrolyte and NMC nodes. The extracted networks for both cathodes samples can be seen in Figure 6.1(b, j) where nodes on each network are shown as spherical balls while throats are shown as cylindrical sticks. The interconnections between phases are shown in Figure 6.1 (c, k).

Table 6.1 Properties of XCT images of NMC532 Cathodes

Property	Units	NMC532 (1CAL)	NMC532 (3CAL)
Coating Thickness	μm	129	88
Volume Fraction	%	-	-
Electrolyte phase	-	36.8	36.6
Active Material (NMC532)	-	49.28	49.74
Carbon and Binder Domain (CBD)	-	13.92	13.66
Density	mg/cm^{-2}	29.78	20.40
Experimental C-rate	mAh/g_{NMC}	178	182
Image size	$voxels$	320 x 250 x 250	221 x 250 x 250
Voxel Size	nm	398	398
Extracted Network	(Nodes, Bonds)	4637, 31427	3510 , 23126
Electrolyte phase	-	1238, 1943	982, 1459
Active Material (NMC532)	-	1722, 3736	1295, 2760
Carbon and Binder Domain (CBD)	-	1680, 3375	1233, 2310
Interconnections	Bonds	22373	16597
NMC532-CBD	-	7620	5355
Electrolyte-CBD	-	6602	4979
Electrolyte-NMC532	-	8151	6263

6.4.3. Governing Equations

The developed mathematical model simulates galvanostatic discharge behaviour of $Li/ Li(Ni_{0.5}Mn_{0.3}Co_{0.2})O_2$ half-cell sandwich as shown in Figure 6.2. The cell contains three regions: namely lithium foil as anode, porous separator filled with electrolyte and porous cathode containing electrolyte, active material (NMC532) and carbon binder domain (CBD). During discharge process, lithium-ions are liberated from lithium foil anode, pass through the separator, and then into the cathode via the electrolyte-filled void; while electrons travel from the Li-foil anode to cathode current collector via external circuit. No expansion of active material upon insertion of lithium metal is considered to avoid model complexity.

The electrochemical reaction at the electrolyte/active material surface of cathode during galvanostatic discharge is:

$$Li^{+}+e^{-}\rightleftharpoons \quad Li(s) \qquad 6.1$$

The concentration (c) of the electrolyte in the cathode region can be estimated using the Nernst-Plank equation. The equation is written in discrete form for every i^{th} pore in electrolyte phase of pore network as:

$$\begin{aligned} v_i\left(\frac{c_i^{t+\Delta t}-c_i^{t}}{\Delta t}\right) = & \sum_{j=1}^{N_{k_{elec}}}\left[G_{ij}^{d}+max\left(-G_{ij}^{m}\left(\varphi_i^t-\varphi_j^t\right),0\right)\right]c_i^t \\ & -\sum_{j=1}^{N_{k_{elec}}}\left[G_{ij}^{d}+max\left(G_{ij}^{m}\left(\varphi_i^t-\varphi_j^t\right),0\right)\right]c_j^t + a_{ij}j_{n,rp}^{t} \qquad 6.2 \end{aligned}$$

$$k_{elec}=1,2,\dots,N_p^{elec}$$

where v_i is volume of pores, φ is electrolyte potential, a_{ij} is the interfacial area between active material particle i and electrolyte pore j and $j_{n,rp}$ is the pore wall flux of lithium ion across the interface between active material particle i and electrolyte pore j. This term is only applicable for reaction pores (rp) and is considered zero for pores that are not at the interface of electrolyte/active material particle. Lastly, G_{ij}^{d} and G_{ij}^{m} are the diffusive and migrative conductance between pore i and j that are calculated using linear resistor theory for resistors according to equation 6.3 and 6.4 respectively.

$$G_{ij}^{d} = \left(\frac{1}{g_i^d} + \frac{1}{g_{ij}^d} + \frac{1}{g_j^d}\right)^{-1} \tag{6.3}$$

$$G_{ij}^{m} = \left(\frac{1}{g_i^m} + \frac{1}{g_{ij}^m} + \frac{1}{g_j^m}\right)^{-1} \tag{6.4}$$

where

$$g_i^d = \frac{A_i D_{Li^+}}{l_i} \tag{6.5}$$

$$g_i^m = \frac{zF}{RT} g_i^d \tag{6.6}$$

The potential distribution in the electrolyte phase is calculated with respect to lithium reference electrode, which leads to the following potential equation written in terms of current density in the cathode region for every i^{th} pore as:

$$i_{i,elec} = -zF\left(\sum_{j=1}^{N_{k_{elec}}} G_{ij}^{d}(c_i^t - c_j^t)\right) - \sum_{j=1}^{N_{k_{elec}}} K_{ij}^{elec}(\varphi_i^t - \varphi_j^t) \tag{6.7}$$

$$k_{elec} = 1, 2, \dots, N_p^{elec}$$

where $i_{i,elec}$ is the current density of i^{th} pore in the electrolyte phase of cathode region and K_{ij}^{elec} is the ionic conductance of the electrolyte solution between pore i and pore j as follows:

$$K_{ij}^{elec} = \left(\frac{1}{k_i^{elec}} + \frac{1}{k_{ij}^{elec}} + \frac{1}{k_j^{elec}}\right)^{-1} \qquad 6.8$$

where

$$k_i^{elec} = zFg_i^m c_i^t \qquad 6.9$$

The diffusivity and conductivity of $Li^+ ion$ in the separator and cathode region is assumed to be dependent on electrolyte phase concentration. Also, lithium diffusivity in active material is assumed to be dependent on state of charge. The relationship to estimate diffusivity and conductivity is defined in Table 6.2. The diffusion of lithium inside active material obeys Fick's law and expressed for active material particle i for time step Δt as equation 6.10. Where G_{ij}^{sd} is the diffusive conductance of lithium in the active material phase defined by equation 6.11.

$$v_i\left(\frac{c_i^{t+\Delta t} - c_i^t}{\Delta t}\right) = \sum_{j=1}^{N_{k_{AM}}} G_{i,j}^{sd}\left(c_i^t - c_j^t\right) \qquad k_{AM} = 1, 2, \dots, N_s^{AM} \qquad 6.10$$

$$G_{ij}^{sd} = \left(\frac{1}{g_i^{sd}} + \frac{1}{g_{ij}^{sd}} + \frac{1}{g_j^{sd}}\right)^{-1} \qquad 6.11$$

where

$$g_{ij}^{sd} = \frac{A_i D_{Li}}{l_i} \qquad 6.12$$

The distribution of potential of an arbitrary particle i in the active material and carbon binder phase of cathode region was calculated using Ohm's law by equation 6.13 and equation 6.14 respectively. It was assumed that no reaction takes place in carbon binder phase so current in carbon binder phase is same as current in active material phase.

$$i_{i,AM} = -\sum_{j=1}^{N_{k_{AM}}} G_{ij}^{AM}\left({\varphi^t}_{i_{AM}} - \varphi_{j_{AM}}^t\right) \quad k_{AM} = 1, 2, \dots, N_S^{AM} \qquad 6.13$$

$$i_{i,CBD} = -\sum_{j=1}^{N_{k_{CBD}}} G_{ij}^{CBD}\left({\varphi^t}_{i_{CBD}} - \varphi_{j_{CBD}}^t\right) \quad k_{CBD} = 1, 2, \dots, N_S^{CBD} \qquad 6.14$$

where G_{ij}^{AM} and $G_{ij}^{CBD}$are electrical conductance in active material and carbon binder domain respectively. The values are estimated using similar expression of linear resistor theory as previously defined in equation 6.8. The value of conductance in arbitrary active material or carbon binder particle i is defined as

$$g_{ij}^{e} = \frac{A_i \sigma_{AM/CBD}}{l_i} \qquad 6.15$$

The Butler-Volmer expression was used to relate phase potentials to reaction kinetics of the intercalation process [167] of an arbitrary pore i as shown by equation 6.16 below. The exchange current density, overpotential and equilibrium potential polynomial fit [185] were defined according to equations 6.17, 6.18, and 6.19 respectively.

$$aj_{n,i}^t = \frac{\nabla i_{elec}}{zF} = i_i^{0,t}\left(exp\left(\frac{(1-\alpha_c)F}{RT}\eta_{i,c}^t\right) - exp\left(\frac{-\alpha_c F}{RT}\eta_{i,c}^t\right)\right) \qquad 6.16$$

$$i_i^0 = \sum_{j=1}^{N_{i_{elec}}} \left(a_{ij} F k \left(c_{j,elec}^{1-\alpha_c}\right)^t \left(c_{i,max}^t - c_{i,AM}^t\right)^{1-\alpha_c} \left(c_{i,AM}^{\alpha_c}\right)^t\right) \qquad 6.17$$

$$\eta_{i,c}^t = \sum_{j=1}^{N_{i_{elec}}} \left(\varphi_{i,AM}^t - \varphi_{j,elec}^t - U_{i,cathode}^t\right) \qquad 6.18$$

$$\begin{aligned} U_{i,cathode} = {} & 5744.862289\, soc_i^9 - 35520.41099\, soc_i^8 + 95714.29862\, soc_i^7 \\ & - 147364.5514\, soc_i^6 + 142718.3782\, soc_i^5 - 90095.81521\, soc_i^4 \\ & + 37061.41195\, soc_i^3 - 9578.599274\, soc_i^2 + 1409.309503\, soc_i \\ & - 85.31153081 - 0.0003\, exp(7.657\, (soc_i^{115}) \end{aligned} \qquad 6.19$$

The current in solid and electrolyte phase is conserved according to equation 6.20

$$\nabla i_{elec} + \nabla i_{AM} = 0 \qquad 6.20$$

The concentration and potential gradient in the separator region of electrolyte phase were determined using equation 6.21, 6.22 with boundary condition for lithium ion dissociation at anode/separator interface represented by equation 6.23, respectively.

$$\frac{\partial c_{2,s}}{\partial t} = -D_{Li,s}^{eff} \nabla^2 c_{2,s} \qquad 6.21$$

$$\frac{\partial \varphi_{2,s}}{\partial x} = -\frac{i_2}{\kappa_s^{eff}} + \frac{RT}{F}(1 - t_+)\frac{\partial ln c_{2,s}}{\partial x} \qquad 6.22$$

$$\frac{\partial c_{2,s}}{\partial x} = \frac{I(1 - t_+)}{F D_{Li,s}} \qquad 6.23$$

The electrolyte phase potential drop at the interface of anode/separator was determined using Butler Volmer expression at Li foil anode region using equation 6.24.

$$\nabla i_{elec} = i_{foil}^0 \left(exp\left(\frac{(1 - \alpha_a)F}{RT} (\varphi_{L_i} - \varphi_{2,s}) \right) - exp\left(\frac{-\alpha_a F}{RT} (\varphi_{L_i} - \varphi_{2,s}) \right) \right) \qquad 6.24$$

The overall cell potential was defined as the difference of potential at anode and cathode current collector. This study only focuses on three-phase pore network model of cathode region in half cell sandwich. Therefore, separator and lithium foil regions are solved using 1D modelling equations to simulate boundary conditions at separator/cathode boundary region and ultimately estimate cell potential during the galvanostatic discharge process. The solution workflow is described in section 6.4.4.

6.4.3.1. Boundary Conditions

The boundary conditions implemented in electrolyte, active material and carbon binder phase in half cell are as follows:

1. In *cathode region*, no flux boundary conditions for current and lithium ion transport were set in electrolyte phase at $x = L_s + L_c$. Similarly, no flux boundary conditions of lithium in active material phase were set at active material/separator interface and active material/ cathode current collector interface. For electronic flux in solid phase a no flux boundary was set at the interface of separator/solid phase (CBD + AM) at $x = L_s$. Lastly, continuity of mass, mass flux, charge and charge flux were enforced at separator/electrolyte phase interface at $x = L_s$.
2. In *separator region*, a no flux current boundary condition was set at anode/separator interface at $x = 0$. Also, the potential of lithium solid phase (φ_{Li}) was arbitrarily set to zero at this interface. Lastly, the flux of lithium ions was calculated by specifying the boundary condition using equation 6.23.

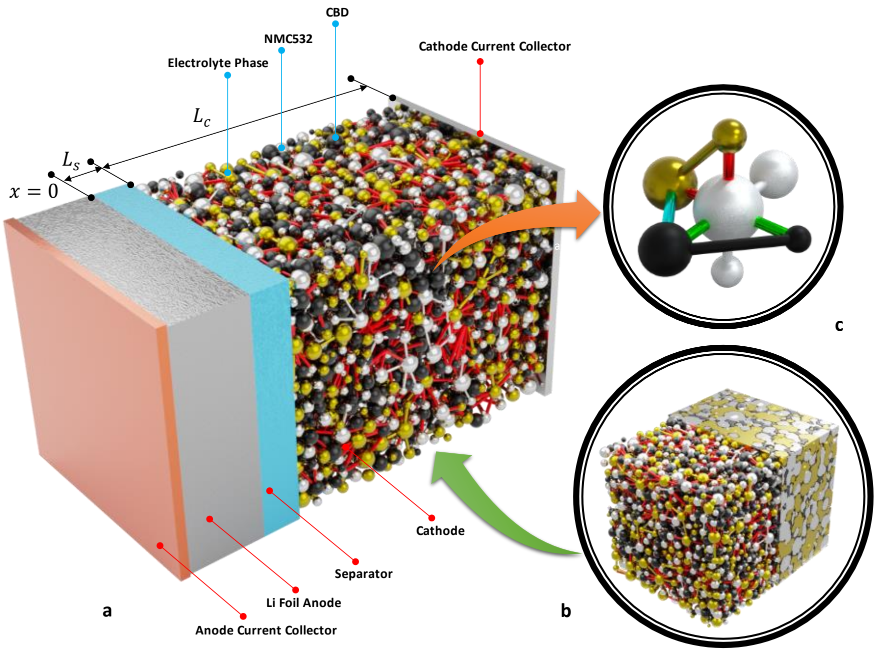

Figure 6.2 a) Lithium Ion battery Half cell pore network modelling schematic, b) Overlayed extracted network from XCT image of cathode, c) Unit cell showing different phases connection with each other. Golden, silver and black colour represent electrolyte, NMC532 and carbon black nodes and single-phase interconnection while the red, green and cyan colour represents interconnection between two different phases.

6.4.4. Workflow and Validation

The pore network modelling workflow is shown in Figure 6.3. To simulate the half-cell all the parameters, material transport properties, boundary and initial values were specified in the first step. The values of all parameters are reported in Table 6.2.

Table 6.2 Lithium-Ion battery half cell PNM model parameters

Parameter	Symbol	*Units*	Value
Separator Thickness	L_s	μm	25
Separator Porosity	$\varepsilon_{\mathrm{sep}}$	%	39
Electronic conductivity of NMC532[177]	σ_{AM}	S/m	0.01
Electronic conductivity of CBD[186]	σ_{CBD}	S/m	760
Ionic conductivity of the electrolyte in the separator[187]	K_s	S/m	(1)
Initial Li$^+$ concentration in the electrolyte[10]	$c_{2,0}$	mol/m^3	1200
Maximal Li concentration in NMC532[10]	$c_{1,max}$	mol/m^3	48900
Diffusion coefficient of Li$^+$ in the electrolyte[187]	D_{Li^+}	m^2/s	$10^{-4.43-\frac{54.0}{T-229-5c_2}-0.22}$
Li diffusion coefficient in AM[10]	D_{Li}	m^2/s	(2)
Faraday constant	F	C/mol	96485
Cathode rate constant	k	$mol/m^2.s$	1e-10
Bruggeman exponent coefficient for the separator	p_{sep}	-	1.5
Ideal gas constant	R	$J/mol.K$	8.314
Reference temperature	T	K	303
Li transference number in separator	t_+		0.363
Cut off Voltage	V	*volts*	3.0
Charge transfer coefficient of NMC	α_c		0.5
Charge transfer coefficient of Li foil	α_a		0.5
Exchange current density of Li foil [10]	i^0_{foil}	A/m^2	19

(1) $10^{-2319soc^{10}+6642soc^{9}-5269soc^{8}-3319soc^{7}+10038soc^{6}-9806soc^{5}+5817soc^{4}-2286soc^{3}+575.3soc^{2}-83.}$

(2) $c_2(-10.5+0.0740T-6.96e^{-5}T^2+0.668c_2-0.0178c_2T+2.80e^{-5}c_2T^2+0.494c_2^2-8.86e^{-4}c_2^2\,T)^2$

Based on the initial and boundary conditions at specific current density, the concentration profile in electrolyte phase of separator and cathode region is simulated. For this purpose, 1D model of diffusion equation in separator is coupled with pore network model of the porous cathode at separator/cathode interface by applying continuity and constant flux boundary conditions of mass and charge transfer respectively. The 1D model in the separator region is necessary as concentration of $Li^{+}ion$ changes at separator/cathode interface, therefore, a fixed concentration boundary condition at this interface is not possible for transient simulations as it will change concentration distribution in cathode region [188,189]. Following this approach 1D model of potential distribution was solved in separator to calculate boundary value of potential at separator/cathode interface after calculating concentration distribution. This allowed estimating potential distribution in the electrolyte phase of cathode regions. This was achieved by applying equation 6.22 and equation 6.7 in the separator and cathode respectively with boundary conditions defined in section 6.4.3.1. The distribution of concentration and potential in electrolyte phase pores allowed simulating Li-Ion insertion reaction at electrolyte/active material interface according to Butler Volmer expression defined in equation 6.16, 6.17, 6.18. The net rate of insertion of Li^{+} was set equal to net rate of formation of Lithium inside active material phase. Also, the solution of Butler Volmer expression requires active material (NMC532) concentration of lithium and potential distribution in the solid phase of the cathode region. The concentration and potential distribution in solid-phase are also affected by carbon and binder domain that is spatially distributed to enhance electronic conductivity of cathode material. Therefore, to achieve the desired current density at cathode current collector, an iterative process is adopted. For this purpose, potential at cathode current collector is guessed and potential distribution in NMC532 and carbon binder phase is calculated using equation 6.13 and 6.14 respectively. If the calculated current and cell applied current density is less than specified tolerance of $1e^{-3}$ than solution is assumed converged otherwise a new value of potential is guessed at cathode current collector to meet convergence criteria. Once the solution is converged the simulation was run for the next time step after updating all field variables, until the cell voltage was greater than cut off voltage of 3 volts.

The pore network model was validated against experimental data for 1CAL and 3CAL electrodes reported in [10]. The cell potential vs capacity curves for 0.2, 0.5 and 1C rates of pore network model was compared with experimentally generated curves and found to agree well as shown in Figure 6.4. Based on good data fit of pore network model the cell potential for 3C was also plotted for both calendared electrodes. Also, the comparison between two electrodes cell potential is shown in Figure 6.4c. It can be seen that 3CAL electrode effective capacity fades lesser than 1CAL electrode, especially at higher discharge rates. This could be due to smaller cathode thickness and pore sizes in electrolyte phase and is discussed in detail in section 6.5.2.

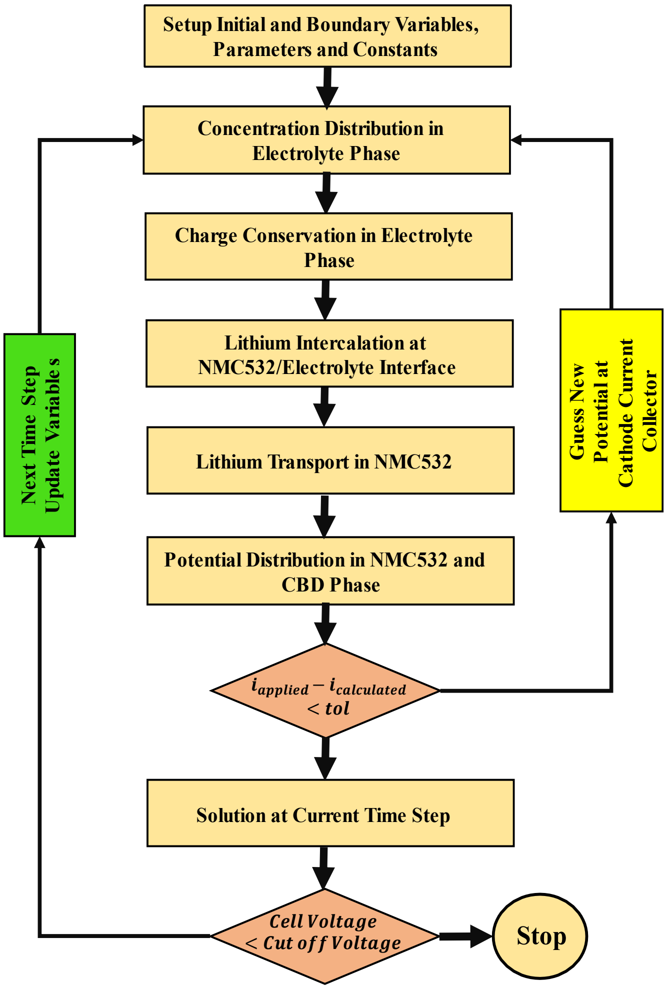

Figure 6.3 Pore network modelling workflow for galvanostatic discharge

6.5. Results and Discussions

6.5.1. Structural Analysis of Cathodes

One of the advantages of pore network modelling is that it can be used effectively to analyze the conditions in each individual solid particle and electrolyte-filled pores. Figure 6.1(e, m) shows pore size distribution as a function of distance from the separator of 1CAL and 3CAL cathodes, respectively. The size of pores is indicated by its marker size and colour. Due to the additional calendaring applied to 3CAL electrodes, the overall size of the pores is smaller than 1CAL cathode. The relatively small size can be attributed to the impaction of some solid particle into the void space, decreasing the diameter of affected pores. The bigger pores have the advantage to store more $Li^{+}ion$ for reaction inside elecotrolyte phase. They also offer less electrolyte concentration gradient than small size pores. Bigger size pore near sperator/cathode interface can increase the mass transport of $Li^{+}ion$ in the cathode region which could ultimately increase the discharge capacity as reported in other studies [2,190] and hence increased intercalation/deintercalation of lithium-ion from electrolyte to active material phase.

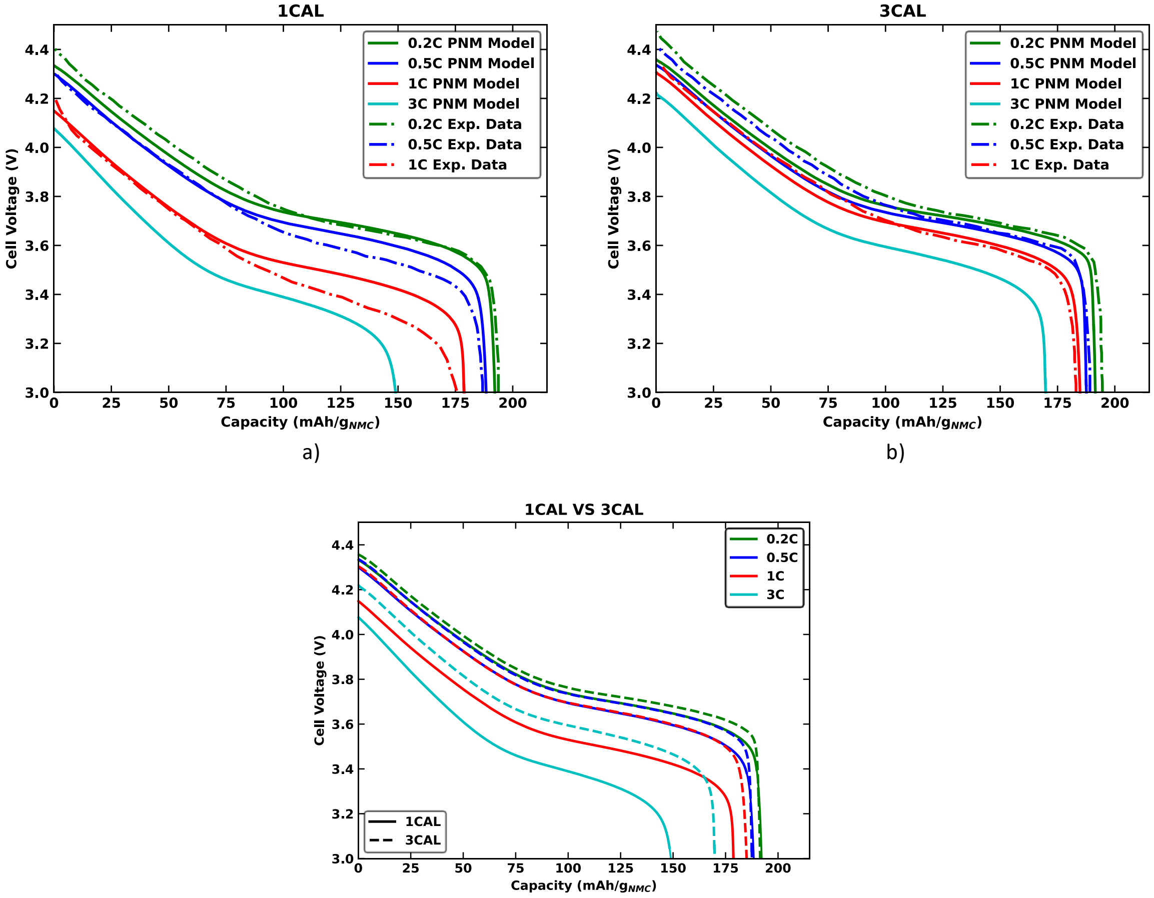

a)

b)

c)

Figure 6.4 a, b) PNM and experimental voltage vs capacity curve for 1CAL and 3CAL respectively, c) Comparison of voltage vs capacity curves at different rates for 1CAL and 3CAL

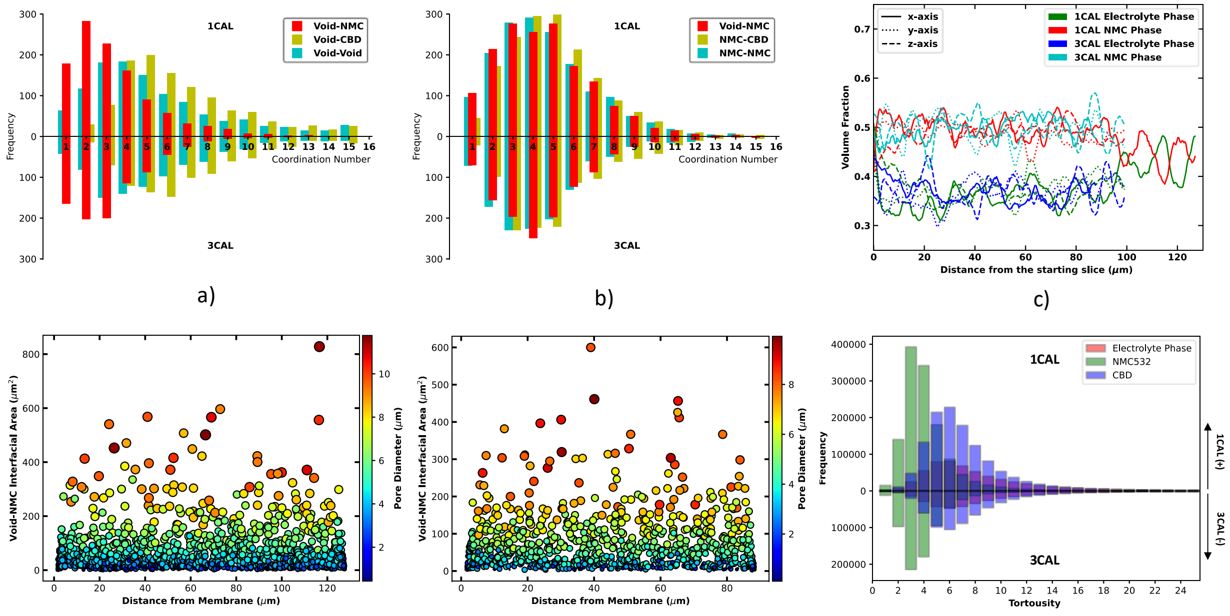

Figure 6.5 a) Coordination number of pores with neighbouring pores, active material and CBD, b) Coordination number of particles from neighbouring active material particles, pores and CBD, c) Slice by slice variation of volume fraction of electrolyte and active material phase in different axis. The flow direction is along x-axis, d, e) shows interfacial area of active material accessible to each pore for 1CAL and 3CAL cathodes. This area is used to in electrochemical reaction, f) Local tortuosity of each pore, particle or CBD region, connected with every other possible pore, particle or CBD region respectively for both 1CAL and 3CAL cathode

Figure 6.1(f, n) shows distribution of particle sizes in the active material phase of 1CAL and 3CAL cathode respectively. The sizes of active material particles are similar for both electrodes with only some differences in the spatial distribution of bigger particles as a function of separator distance. This is expected, given that calendaring is not expected to crack particles unless a large force is applied Figure 6.1(g, h) shows the sphericity of pores and particles in both electrodes. Sphericity is defined as the ratio of surface area of a sphere having the same volume as the object to the actual surface area of the object [191]. It can be seen that the sphericity of moderate to large sized particles is scattered in a narrow range as compared to the pores which are defined by the walls of the particles, so are concave and bound to be less spherical. This trend is same for both cathodes and is aligned with the structure of NMC532 in which particles are generally spherical. Figure 6.1(h, p) shows size distribution histogram of all three phases in 1CAL and

3CAL cathodes. It can be seen that CBD region sizes are smaller than the average pore and particle size. Also, the size of pores in 3CAL is smaller than 1CAL, which is also observed in Figure 6.1(e, m).

Besides size and shape distribution of cathodes, additional structural information can be obtained from the pore network extraction that is relevant to the transport processes. Figure 6.5a shows coordination number of each pore with neighbouring pores, active material particles and CBD regions in both cathodes samples. Higher connectivity generally means more transport paths, and therefore shorter transport lengths between points. It is thus desirable to maximize connectivity of the pore phase to improve Li^{+} diffusion and migration in the electrolyte. Also, higher interconnectivity of pores-to-CBD can assist lithium-ion transport in CBD nanopores to reach the surface of active material particle. On the other hand, Figure 6.5b shows coordination number of active material particles with neighbouring particles, pores and CBD regions. The overall interconnectivity of active material particles is approximately the same in all phases indicating active material particles could structurally support both transport and reaction during intercalation/deintercalation process. Figure 6.5c shows slice by slice volume fraction of different phases in tomography image of cathode. It can be seen that volume fraction in each case is subject to variation which is due to the discrete nature of particles and pores. Figure 6.5d,e shows surface area of active material available to each pore in the electrolyte phase for 1CAL and 3CAL cathode samples respectively. The surface area of most of the particles is under $200\ \mu m^{2}$ while a few pores with a relatively large size have more interfacial area available for reaction. Lastly, Figure 6.5f shows the network tortuosity, which was calculated by finding the shorted path between each node in a given phase to every other node in the same phase (found using the Dijkstra algorithm weighted by node-to-node distance), divided by the total Euclidean distance between them. This network tortuosity was measured for all three phases and gives insights of interconnectivity of structure in each phase. Higher values mean the path between nodes is tortuous and it will offer high resistance to transport. The properties graph mentioned in Figure 6.5 give important information regarding microstructural heterogeneities inside porous cathode and they should be considered to optimize electrode design during the manufacturing process or battery modelling.

6.5.2. Performance Analysis of Cathodes

One of the benefits of pore-scale modeling is the ability to inspect the conditions in each pore and particle. Figure 6.6 shows discharge fields of 1CAL cathode at 1C and 3C-rate at 75% state of lithiation (SoL), highlighting the spatial heterogeneities of four transport variables in different phases of cathode. To observe the effect of different variables like electrolyte and active material concentration and potential distribution during galvanostatic discharge, the diameter of pores and particles have been classified into three size zones.

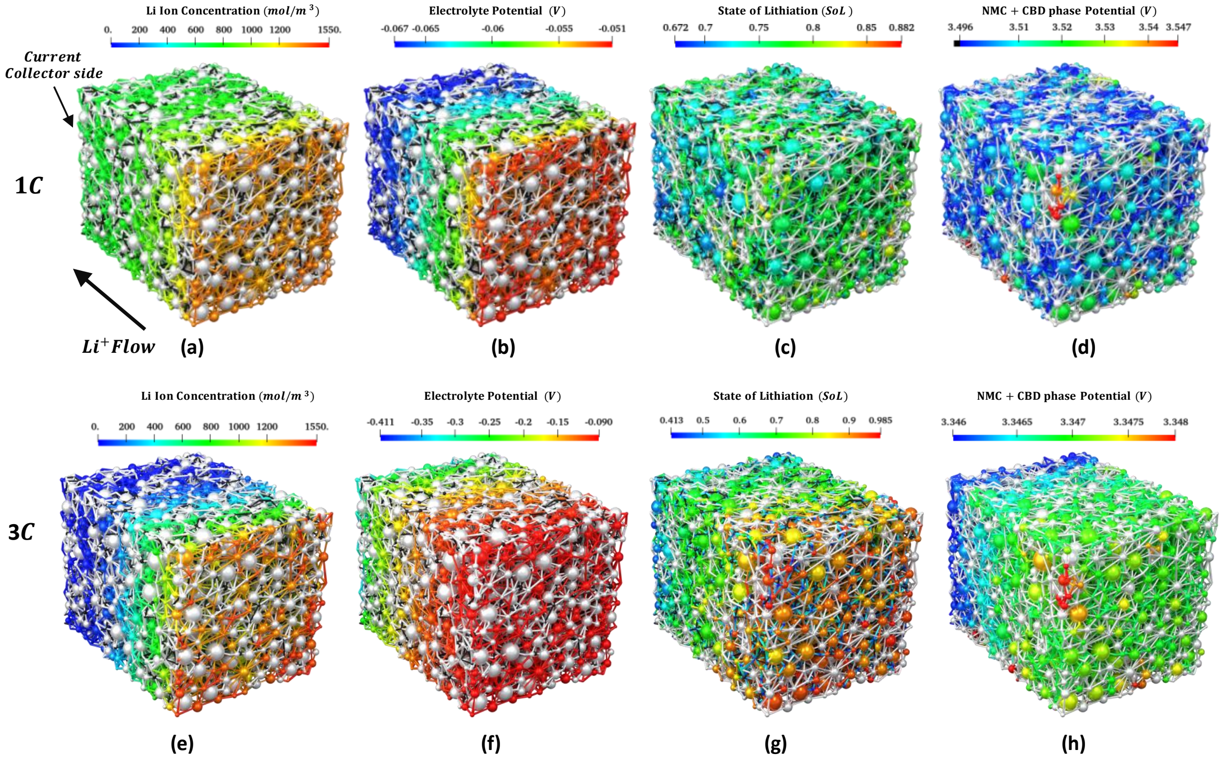

Figure 6.6 a, e) Li^+ concentration profile in electrolyte phase for 1C and 3C-rate for 1CAL cathode, b, f) Potential distribution in electrolyte phase for 1C and 3C rate, c, g) State of lithiation (SoL) spatial distribution in active material phase for 1C and 3C rate respectively, d, h) Local variation of potential drop in NMC + CBD phase for 1C and 3C rate.

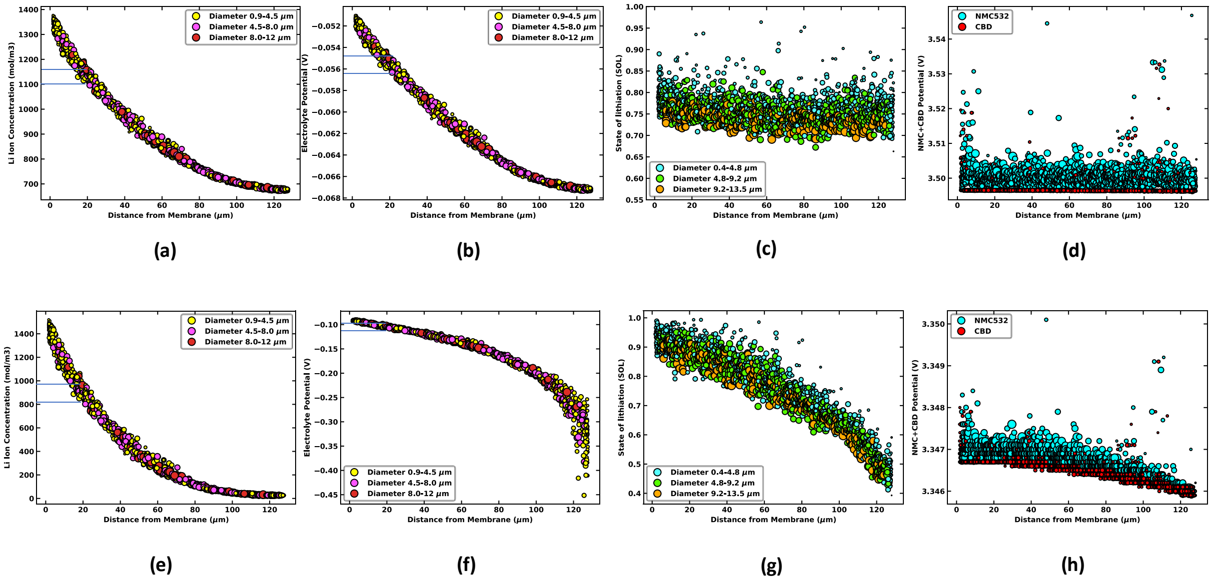

Figure 6.7 a, e) Li$^+$ concentration profile as a function of separator distance for three different size zones in 1C and 3C-rate of 1CAL cathode, b, f) Spatial distribution of potential drop in electrolyte phase as a function of separator distance for 1C and 3C rate, c, g) State of lithiation (SoL) for three different particle size zones in active material phase for 1C and 3C rate respectively, d, h) Potential drop in NMC + CBD particles as a function of separator distance.

In Figure 6.1(d, l) the distribution of these zones in electrolyte and active material can be seen for both electrodes. The diameter range of each zone is assigned with a unique colour and will be used to study the effect of local heterogeneities on the discharge behaviour. Figure 6.7(a, e) shows profiles of each variable for three different particle size ranges mentioned in Figure 6.1d. The concentration decreases away from the separator as expected due to consumption of Li ions in the cathode. This behavior can of course be predicted by normal P2D models, but the distribution of concentrations at a given position can only be obtained with a pore-scale approach. It can be seen that spatial distribution of concentration till 80 μm distance from separator is almost 75 mol/m^3 for 1C-rate while variation in concentration for 3C rate has almost doubled to 150 mol/m^3. This local distribution is highlighted at 20μm from separator by bracketing the thickness of concentration profile for both C rates. This overall variation is due to local size distribution of pores as well as their interconnectivity or accessibility. Beyond 80 μm the overall concentration is more consistent for both C-rates. This could be due to smaller concentration gradients leading to . Also, as seen in Figure 6.5c the high porosity of electrode in this zone could result in relatively bigger size pores hand hence dampening any abrupt spatial variation in concentration.

Figure 6.6 (b, f) and Figure 6.7 (b, f) shows electrolyte phase potential distribution of the 1CAL cathode for 1C and 3C discharge rates. The potential drop in electrolyte phase for 3C rate is much higher than 1C rate, as expected due to higher current and concentration gradient during discharge at 3C rate. Also, similar to concentration profile, the spatial variation in potential distribution for 1C rate is low (approximately $1\ mV$), while on the other hand at 3C the potential has a broad distribution (approximately $200\ mV$ at the current collector). This effect can be attributed to very low concentration of Li Ions near current collector as seen in Figure 6.6e. Due to fast electrochemical reaction, most of the Li Ions are consumed before reaching the current collector leading to deficiency of positive ions and hence increasing potential drop. Also, it can be seen that small pores respond to Li-Ion deficiency faster than big pores because of relatively small ability to accumulate Li-ion inside as compared to bigger pores. So, in order to achieve more SoL and to avoid exhaustion of Li Ions, bigger pores near current collector are recommended. It is worth noting that this spread of potential is only possible, because pore network modelling is capturing potential distribution locally in each pore unlike continuum model which simulates only average potential.

Figure 6.6(c, g) and Figure 6.7(c, g) shows the state of lithiation (SoL) of lithium in NMC active material phase. For 1C rate the spatial distribution of SoL varies widely at a particular distance from the separator but on an average SoL remains at same level throughout the length of the cathode. Moreover, it can be observed that SoL in smaller size NMC particles are at higher values of SoL compared to large particles. On the other hand, at higher C-rate the lithiation distribution varies widely both spatially and thorough out length of the cathode. As seen in Figure 6.6g the lithiation is almost completed near separator/cathode interface while it gradually decreases as we move away from the separator. The low value of SoL can be attributed to less availability of Li-Ion near current collector in the electrolyte phase. Also, similar to 1C rate, smaller NMC particle show higher SoL as compared to bigger size particles indicating the importance of small size active material for fast charging of LIB’s because of availability of more interfacial area as compared to bigger size particles to carry out intercalation reaction.

Figure 6.6(d, h) and Figure 6.7(d, h) shows potential distribution in NMC active material and CBD phase for 1C and 3C rates. For low discharge rate active material particles are slightly at higher potential than CBD phase. This is due to higher conductivity of electrons in CBD phase than NMC particles. Besides some local variation of potential in NMC particles, the potential drop is more prominent near separator/cathode interface. This could be due to long tortuous path electrons need to travel from current collector towards separator/cathode interface. Contrary to NMC particles, CBD phase shows narrow distribution of potential with only a few local deviations of particles. One the other hand, at 3C rate a potential drop of approximately 1 mV is observed from separator/cathode interface to current collector in both NMC and CBD phase. This drop can be explained by the fast reaction near separator causing deficiency of electrons in this region. Moreover, the spatial distribution of potential is for NMC and CBD phase is narrow near current collector as compared to separator interface. This effect could be due to the low concentration of Li-Ion in electrolyte phase making reaction kinetics slower in this region.

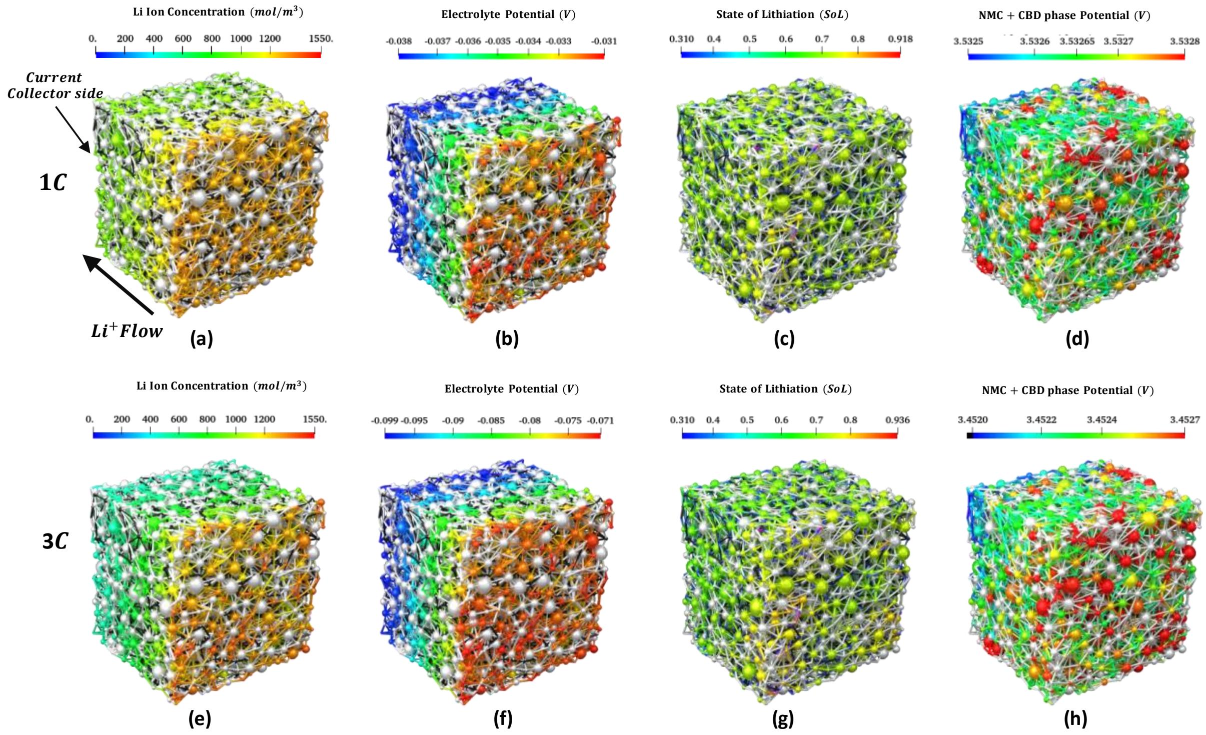

Figure 6.8 a, e) Li$^+$ concentration profile in electrolyte phase for 1C and 3C-rate for 3CAL cathode, b, f) Potential distribution in electrolyte phase for 1C and 3C rate, c, g) State of lithiation (SoL) spatial distribution in active material phase for 1C and 3C rate respectively, d, h) Local variation of potential drop in NMC + CBD phase for 1C and 3C rate

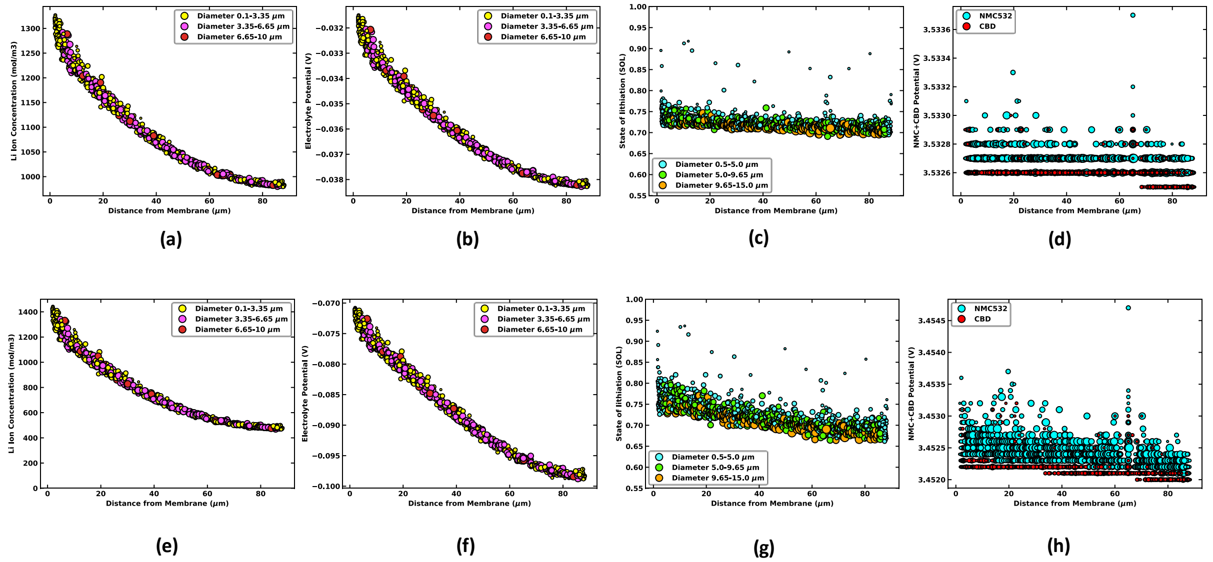

Figure 6.9 a, e) Li$^+$ concentration profile as a function of separator distance for three different size zones in 1C and 3C-rate of 3CAL cathode, b, f) Spatial distribution of potential drop in electrolyte phase as a function of separator distance for 1C and 3C rate, c, g) State of lithiation (SoL) for three different particle size zones in active material phase for 1C and 3C rate respectively, d, h) Potential drop in NMC + CBD particles as a function of separator distance.

Like 1CAL cathode the variable distribution fields and profiles were also developed for 3CAL cathode by carrying out simulations of NMC half cell and replacing 1CAL with 3CAL under same conditions. The results are shown in Figure 6.8 and Figure 6.9. The concentration and potential in electrolyte phase were observed to drop less as compared to 1CAL electrode due to the small thickness of 3CAL cathode. Similarly, SoL and solid-phase potential distribution were observed to less very spatially than 1CAL. The overall SoL trend due to particle size distribution is same as 1CAL cathode indicating the importance of particles sizes for performance optimization of LIB's. The pore-to-pore and particle-to-particle analysis described above using pore network modelling approach can be used as a modelling framework to study structural performance relationship of other electrode microstructures as well. The developed PNM approach can be used to predict structure for next-generation battery electrodes which is beyond the scope of this work and is left for future work.

6.5.3. Computational Performance

Pore network modelling has the key advantage of performing simulation at vastly lower computational cost than the normal DNS approach. A steady-state performance comparison between the two approaches can be seen in our previous work [116]. For the simulation of galvanostatic discharge at different C-rate mentioned above two iterations we performed for each time step. The inner iteration to solve Nernst Plank equation in electrolyte phase took about 1.25 seconds for 1C rate of 1CAL cathode consisting of 4637 Nodes and 24799 bonds. While the outer iteration to converge applied current density with calculated current density took 11.62 seconds for 1 time step. The tolerance values for inner and outer iteration were 1e-8 and 1e-3 respectively. For all simulations, a fixed time step of 2 seconds was used. Implementation of an adaptive time step scheme would offer addition performance improvements, but this is left of a future study. The solution was carried using Lenovo ThinkStation P720 workstation having 8-core Intel(R) Xeon(R) Silver 4110 CPU @ 2.10GHz and 256 GB RAM. For simulation 4 cores were used to get solution of inner iteration.

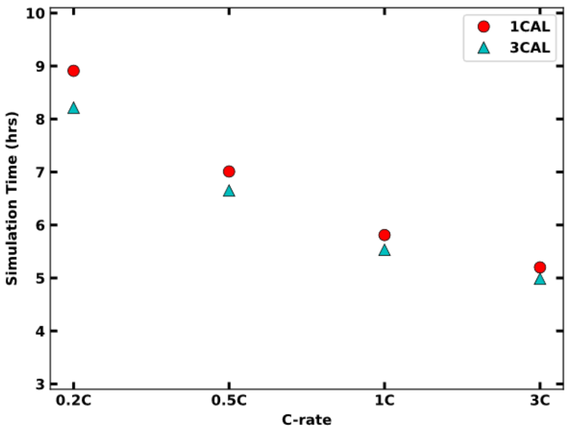

Figure 6.10 Simulation time of pore network model of LIB half cell at different C-rate

The overall computational performance time is shown in Figure 6.10 for 1CAL and 3CAL electrodes. The total number of nodes and bonds in 3CAL electrode were 3510 and 23126 respectively. It can be seen that 3CAL electrode takes less time than 1CAL because of its smaller domain size and few nodes. The overall time increases as the C rate decreases because the total time steps are higher. It should be noted that computational time reported for various DNS simulation is on the order of 1 month; Hutzenlaub et al [80] reported requiring 27 days to perform a simulation on the cluster using four nodes, where each node contained two Intel Xeon E5-2680 CPUs and 32 GB RAM. Similarly, Rucci et al [192] also reported simulation time up to 3 days depending on mesh size on a relatively small domain. Not only is this significantly more computing power than used in the present work, but the domain size used here is also 1.51 times bigger in terms of voxels. This computational performance gain of approximately 115x highlights the importance of pore network modelling approach to simulate complex multiphysics processes.

6.6. Conclusions

In this study, a pore network modelling framework has been developed to analyze structure-performance relationship of two Li($Ni_{0.5}Mn_{0.3}Co_{0.2}$)O_2 cathodes of different thickness achieved by differing calendaring pressure. A three-phase network was extracted from X-ray tomography images consisting of active material, carbon and binder domain and electrolyte phase along with interconnections of these phases with each other. The pore network modelling approach was used to obtain structural information about these two electrodes. It was found that due to more calendaring the size of pores in 3CAL electrode were relatively smaller than 1CAL electrode. Also, sphericity data revealed that active material particles for both electrodes are similarly spherical, indicating that calendaring did not damage the particles, and that the particles were more spherical than electrolyte phase pores. Moreover, structural properties like coordination number, porosity, interfacial area and tortuosity of extracted network revealed important information to analyze local heterogeneities in porous electrodes.

The networks were used to perform galvanostatic discharge of lithium-ion battery half-cell to analyze the effect of local structural heterogeneities on four different transport variables in the cathode region. The pore network model was validated against experimental voltage-capacity curve data and found to agree well at different C-rates. Also, pore-to-pore and particle-to-particle analysis in the electrolyte and solid-phase revealed important insights of structural performance relationship of LIB's. Ultimately, it was demonstrated that PNMs can efficiently predict the rate-dependent capacity of an electrode using only a 3-phase tomogram as input, which is a highly promising result. This suggests that in-silico structures that vary arbitrary properties of the electrode, could be produced and screened for performance using PNMs, avoiding the need to perform expensive and time-consuming cell fabrication and testing in the lab. Of course, this screening could also be performed using DNS, but the massively improved computational performance of pore network modelling approach, at least 115x faster compared to direct numerical simulation, is essential. The developed pore numerical modelling framework provides a great platform to optimize structural features of cathodes and hence can predict next-generation electrode material to allow fast charging of LIB's.

Chapter 7 Conclusions and Future Work

7.1. Summary

This thesis aimed to relate structural heterogeneities of porous electrodes with cell performance of lithium-ion batteries. For this purpose, an image-based pore network modelling framework was developed to understand the structural performance relationship of porous electrodes at various sets of conditions. The following efforts were made to achieve these objectives:

In Chapter 3 a dual network extraction algorithm was developed to simultaneously extract void and solid networks from tomographic images of porous domains using simple image processing techniques. The algorithm extracted structural features of void and solid phases such as connectivity and geometrical properties, along with interconnection between void-solid phases. The validation of the dual network was performed on simple cubic and random sphere packings from low to high porosities. Pore network modelling simulations were performed to estimate effective diffusivity and thermal conductivity in void and solid-phase respectively and found to agree well with experimental and direct numerical simulation data. The study also incorporated a novel technique to estimate the interfacial area at void-solid phase interface which is crucial for interphase transport and reaction process. The solid phase network and its interaction with the void phase were addressed for the first time in pore network modelling, opening up a new avenue to study multiphase mass transport processes.

In Chapter 4, dual network algorithm extraction capabilities were extended to an arbitrary number of phases. This enabled the extraction of electrolyte, active material and carbon binder domain from lithium-ion porous cathode images. The algorithm was tested on a tomography image of NMC811 cathode to extract all three phases along with interconnections between any two phases. The novel three-phase pore network model was used to simulate steady-state reaction-diffusion and reaction-conduction process in the electrolyte and active material phase respectively. The results were compared with direct numerical simulation and found to agree well at various set of conditions but at a significantly less computational cost.

The developed model was used to analyze the impact of carbon binder domain on current density. It was found that current density decreases by 24.4 % when carbon binder was not assumed lumped with active material phase. The effect of nano porosity in carbon and binder domain revealed 16.8% increase in reaction rate as compared to solid binder without any porosity.

Although pore network modelling is a computationally efficient approach, extracting a network a tomography image is a computationally expensive process requiring large amount of computational resources. The solution for this bottleneck was addressed in Chapter 5, where an efficient network extraction algorithm was developed that divides massive tomograms into small subdomains using geometric domain decomposition. The algorithm was used to extract pore networks from various types of digital rock images. The developed algorithm saved up to 7 times computational time and 50 % RAM usage. Finally taking advantage of computational efficiency, the algorithm was used to perform a resolution study of tomography image that could lead to incorrect results of transport properties simulation.

Lastly, in Chapter 6, a pore network modelling framework to study the galvanostatic discharge behaviour of lithium-ion battery cathode was developed. The voltage vs capacity data for three-phase networks of NMC 532 cathodes was simulated and compared with experimental data at different C rate. The results were found to agree well with experimental data. The model was then used to compare structural properties of two cathodes having different thickness due to varying calendaring pressure. The connectivity and size distribution in the electrolyte and solid phase gave important insights about the structure of cathode. The structural-performance relationship of four different transport variables was analyzed. The spatial distribution of concentration and potential in pores of electrolyte phase revealed the effect of local heterogeneities of pores on these transport variables. Similarly, local variations of lithium and potential distribution in active material and carbon binder phase gave important insights about structural-performance relationship of porous cathodes. Lastly, computational performance of the pore network model was analyzed at four different C -rates. The results revealed massive improvement in computational time than previously reported work using DNS. This computational performance gain highlights the importance of pore network modelling approach to simulate complex multiphysics processes.

7.2. Future Work

7.2.1. Multiphase network extraction algorithm

In Chapter 3 dual-phase network extraction algorithm was developed, which was extended to any number of phases in Chapter 4 to simulate multiphase transport in electrolyte, active material and carbon binder domain of lithium-Ion battery cathode. These extraction algorithm needs further refinement to capture multi-scale effects from tomography images. For examples, carbon binder domain in lithium-ion battery has macro and nano-size pores which effects overall Li^+ion transport in electrolyte phase and hence overall cell performance of battery. So, a two-stage extraction algorithm is needed which extracts nanopore network in the first stage and then stitch it with macro phase network. This will greatly improve the accuracy of transport processes in porous material that are sensitive to multiscale effects. Of course, this requires a sufficiently resolved image, which introduces problems with limited field of view.

So far pore network extraction algorithm developed in the literature deals with fixed size of pores and throats in the network. Some porous material especially in lithium-ion battery is subject to deformation or swelling during charge and discharge cycle of operation. This change in shape of material results in degradation and hence breakdown of battery. A novel network model is required that can dynamically change the size of pores and throats as a function of its swelling or deformation rate. This will greatly help to perform a stress analysis on lithium-ion battery porous electrode materials.

7.2.2. Efficient Extraction of Massive Size Pore Networks

One of the main challenges in dealing with the tomographic image is that resolution can strong effect the accuracy of results obtained from extracted pore networks. This is because structural properties extracted from a low-resolution image become invisible to watershed segmentation algorithm. In Chapter 5, the developed domain decomposition algorithm has the potential to address this issue by performing network extraction after increasing the resolution of the image, but a more comprehensive criterion is required that can determine a suitable resolution before network extraction. One approach could be to identify the smallest pore size in the porous domain and scale up the image based on this information so that watershed segmentation can partition smallest pore size region in the image without any over-segmentation.

7.2.3. Multiphysics Pore Network Modelling of Lithium-Ion Battery Cathodes

In Chapter 6 the pore network modelling framework for three-phase lithium-ion battery cathodes were developed to study galvanostatic discharge behaviour of half-cell. The model gave important insights into the microstructural effects in different phases of porous cathode. However, the developed pore network model can be extended to simulate to full cell including anode pore network of lithium-ion battery. Also, this framework can be extended to study the thermal effects in the active material particles that decreases the cell energy capacity. Finally, the transient algorithms should implement adaptive time stepping which will significantly improve the computational performance. The comparisons to DNS simulations show PNMs reduced time by 100x or more, but this could be even better if larger time steps were taken when possible.

References

[1] D. Seok, Y. Jeong, K. Han, D.Y. Yoon, H. Sohn, Recent progress of electrochemical energy devices: Metal oxide-carbon nanocomposites as materials for next-generation chemical storage for renewable energy, Sustain. 11 (2019). doi:10.3390/su11133694.

[2] X. Lu, A. Bertei, D.P. Finegan, C. Tan, S.R. Daemi, J.S. Weaving, K.B. O'Regan, T.M.M. Heenan, G. Hinds, E. Kendrick, D.J.L. Brett, P.R. Shearing, 3D microstructure design of lithium-ion battery electrodes assisted by X-ray nano-computed tomography and modelling, Nat. Commun. 11 (2020) 1–13. doi:10.1038/s41467-020-15811-x.

[3] A. Torayev, A. Rucci, P.C.M.M. Magusin, A. Demortière, V. De Andrade, C.P. Grey, C. Merlet, A.A. Franco, Stochasticity of Pores Interconnectivity in Li-O2 Batteries and its Impact on the Variations in Electrochemical Performance, J. Phys. Chem. Lett. 9 (2018) 791–797. doi:10.1021/acs.jpclett.7b03315.

[4] M.S. Talukdar, O. Torsaeter, M.A. Ioannidis, J.J. Howard, Stochastic reconstruction of chalk from 2D images, Transp. Porous Media. 48 (2002) 101–123. doi:10.1023/A:1015650705205.

[5] R. Xu, J. Xiang, J. Feng, X. Lu, Z. Hao, L. Kang, M. Li, Y. Wu, C. Tan, Y. Liu, G. He, D.J.L. Brett, P.R. Shearing, L. Yuan, Y. Huang, F.R. Wang, In situ visualization by X-Ray computed tomography on sulfur stabilization and lithium polysulfides immobilization in S@HCS/MnOx cathode, Energy Storage Mater. 31 (2020) 164–171. doi:10.1016/j.ensm.2020.06.011.

[6] X. Lu, T. Li, A. Bertei, J.I.S. Cho, T.M.M. Heenan, M.F. Rabuni, K. Li, D.J.L. Brett, P.R. Shearing, The application of hierarchical structures in energy devices: New insights into the design of solid oxide fuel cells with enhanced mass transport, Energy Environ. Sci. 11 (2018) 2390–2403. doi:10.1039/c8ee01064a.

[7] S.R. Daemi, C. Tan, T. Volkenandt, S.J. Cooper, A. Palacios-Padros, J. Cookson, D.J.L. Brett,

P.R. Shearing, Visualizing the Carbon Binder Phase of Battery Electrodes in Three Dimensions, ACS Appl. Energy Mater. 1 (2018) 3702–3710. doi:10.1021/acsaem.8b00501.

[8] A. Rabbani, P. Mostaghimi, R.T. Armstrong, Pore network extraction using geometrical domain decomposition, Adv. Water Resour. 123 (2019) 70–83. doi:10.1016/j.advwatres.2018.11.003.

[9] Z.A. Khan, A. Elkamel, J.T. Gostick, Efficient extraction of pore networks from massive tomograms via geometric domain decomposition, Adv. Water Resour. 145 (2020). doi:10.1016/j.advwatres.2020.103734.

[10] F.L.E. Usseglio-Viretta, A. Colclasure, A.N. Mistry, K.P.Y. Claver, F. Pouraghajan, D.P. Finegan, T.M.M. Heenan, D. Abraham, P.P. Mukherjee, D. Wheeler, P. Shearing, S.J. Cooper, K. Smith, Resolving the Discrepancy in Tortuosity Factor Estimation for Li-Ion Battery Electrodes through Micro-Macro Modeling and Experiment, J. Electrochem. Soc. 165 (2018) A3403–A3426. doi:10.1149/2.0731814jes.

[11] L. Zielke, T. Hutzenlaub, D.R. Wheeler, C.W. Chao, I. Manke, A. Hilger, N. Paust, R. Zengerle, S. Thiele, Three-phase multiscale modeling of a LiCoO2 cathode: Combining the advantages of FIB-SEM imaging and X-ray tomography, Adv. Energy Mater. 5 (2015) 1–8. doi:10.1002/aenm.201401612.

[12] J. Newman, W. Tiedemann, Porous-electrode theory with battery applications, AIChE J. 21 (1975) 25–41. doi:10.1002/aic.690210103.

[13] J.S. Newman, C.W. Tobias, Theoretical Analysis of Current Distribution in Porous Electrodes, J. Electrochem. Soc. 109 (1962) 1183. doi:10.1149/1.2425269.

[14] K.E. Thomas, J. Newman, Thermal Modeling of Porous Insertion Electrodes, J. Electrochem. Soc. 150 (2003) A176. doi:10.1149/1.1531194.

[15] S. Renganathan, G. Sikha, S. Santhanagopalan, R.E. White, Theoretical Analysis of Stresses in a Lithium Ion Cell, J. Electrochem. Soc. 157 (2010) A155. doi:10.1149/1.3261809.

[16] J. Christensen, Modeling Diffusion-Induced Stress in Li-Ion Cells with Porous Electrodes, J. Electrochem. Soc. 157 (2010) A366. doi:10.1149/1.3269995.

[17] A. Gayon Lombardo, B.A. Simon, O. Taiwo, S.J. Neethling, N.P. Brandon, A pore network model of porous electrodes in electrochemical devices, J. Energy Storage. 24 (2019) 100736. doi:10.1016/j.est.2019.04.010.

[18] R. Banerjee, N. Bevilacqua, L. Eifert, R. Zeis, Characterization of carbon felt electrodes for vanadium redox flow batteries – A pore network modeling approach, J. Energy Storage. 21 (2019) 163–171. doi:10.1016/j.est.2018.11.014.

[19] M.A. Sadeghi, M. Aganou, M. Kok, M. Aghighi, G. Merle, J. Barralet, J. Gostick, Exploring the Impact of Electrode Microstructure on Redox Flow Battery Performance Using a Multiphysics Pore Network Model, J. Electrochem. Soc. 166 (2019) A2121–A2130. doi:10.1149/2.0721910jes.

[20] M.F. Lagadec, R. Zahn, S. Müller, V. Wood, Topological and network analysis of lithium ion battery components: the importance of pore space connectivity for cell operation, Energy Environ. Sci. 11 (2018) 3194–3200. doi:10.1039/C8EE00875B.

[21] M. Doyle, T.F. Fuller, J. Newman, Modeling of Galvanostatic Charge and Discharge, J. Electrochem. Soc. 140 (1993) 1526–1533.

[22] B. Tjaden, S.J. Cooper, D.J. Brett, D. Kramer, P.R. Shearing, On the origin and application of the Bruggeman correlation for analysing transport phenomena in electrochemical systems, Curr. Opin. Chem. Eng. 12 (2016) 44–51. doi:10.1016/j.coche.2016.02.006.

[23] I. Baccouche, S. Jemmali, B. Manai, N. Omar, N. Essoukri Ben Amara, Improved OCV model of a Li-ion NMC battery for online SOC estimation using the extended Kalman filter, Energies. 10 (2017) 1–22. doi:10.3390/en10060764.

[24] W.B. Lindquist, S.-M. Lee, D.A. Coker, K.W. Jones, P. Spanne, Medial axis analysis of void structure in three-dimensional tomographic images of porous media, J. Geophys. Res. Solid Earth.

101 (1996) 8297–8310. doi:10.1029/95JB03039.

[25] C.A. Baldwin, A.J. Sederman, M.D. Mantle, P. Alexander, L.F. Gladden, Determination and Characterization of the Structure of a Pore Space from 3D Volume Images, J. Colloid Interface Sci. 181 (1996) 79–92. doi:10.1006/JCIS.1996.0358.

[26] Z. Jiang, K. Wu, G. Couples, M.I.J. van Dijke, K.S. Sorbie, J. Ma, Efficient extraction of networks from three-dimensional porous media, Water Resour. Res. 43 (2007). doi:10.1029/2006WR005780.

[27] D. Silin, T. Patzek, Pore space morphology analysis using maximal inscribed spheres, Phys. A Stat. Mech. Its Appl. 371 (2006) 336–360. doi:10.1016/j.physa.2006.04.048.

[28] J.T. Gostick, Versatile and efficient pore network extraction method usingmarker-based watershed segmentation, 1 Phys. Rev. E. 003300 (2017) 1–11. doi:10.1103/PhysRevE.00.003300.

[29] K.E. Thompson, C.S. Willson, C.D. White, S. Nyman, J. Bhattacharya, A.H. Reed, Application of a New Grain-Based Reconstruction Algorithm to Microtomography Images for Quantitative Characterization and Flow Modeling, SPE Annu. Tech. Conf. Exhib. 298 (2005). doi:10.2118/95887-MS.

[30] A.P. Sheppard, R.M. Sok, H. Averdunk, V.B. Robins, A. Ghous, Analysis of Rock Microstructure Using High- Resolution X-Ray Tomography, Proc. Int. Symp. Soc. Core Anal. (2006) 1–12.

[31] A. Rabbani, S. Jamshidi, S. Salehi, Journal of Petroleum Science and Engineering An automated simple algorithm for realistic pore network extraction from micro-tomography images, J. Pet. Sci. Eng. 123 (2014) 164–171. doi:10.1016/j.petrol.2014.08.020.

[32] J. Gostick, M. Aghighi, J. Hinebaugh, T. Tranter, M.A. Hoeh, H. Day, B. Spellacy, M.H. Sharqawy, A. Bazylak, A. Burns, W. Lehnert, A. Putz, OpenPNM: A Pore Network Modeling Package, Comput. Sci. Eng. 18 (2016) 60–74. doi:10.1109/MCSE.2016.49.

[33] R.R. Rashapov, J.T. Gostick, In-Plane Effective Diffusivity in PEMFC Gas Diffusion Layers, Transp. Porous Media. 115 (2016) 1–23. doi:10.1007/s11242-016-0648-4.

[34] R. Wu, Q. Liao, X. Zhu, H. Wang, Pore network modeling of cathode catalyst layer of proton exchange membrane fuel cell, Int. J. Hydrogen Energy. 37 (2012) 11255–11267. doi:10.1016/j.ijhydene.2012.04.036.

[35] M. Aghighi, J. Gostick, Pore network modeling of phase change in PEM fuel cell fibrous cathode, J. Appl. Electrochem. 47 (2017) 1323–1338. doi:10.1007/s10800-017-1126-6.

[36] M.A. Sadeghi, M. Agnaou, J. Barralet, J. Gostick, Dispersion modeling in pore networks: A comparison of common pore-scale models and alternative approaches, J. Contam. Hydrol. 228 (2020) 103578. doi:10.1016/J.JCONHYD.2019.103578.

[37] J.H. Nam, M. Kaviany, Effective diffusivity and water-saturation distribution in single- and two-layer PEMFC diffusion medium, Int. J. Heat Mass Transf. 46 (2003) 4595–4611. doi:10.1016/S0017-9310(03)00305-3.

[38] J.T. Gostick, M.A. Ioannidis, M.W. Fowler, M.D. Pritzker, Pore network modeling of fibrous gas diffusion layers for polymer electrolyte membrane fuel cells, J. Power Sources. 173 (2007) 277–290. doi:10.1016/j.jpowsour.2007.04.059.

[39] G. Luo, Y. Ji, C.Y. Wang, P.K. Sinha, Modeling liquid water transport in gas diffusion layers by topologically equivalent pore network, Electrochim. Acta. 55 (2010) 5332–5341. doi:10.1016/j.electacta.2010.04.078.

[40] J.T. Gostick, Random Pore Network Modeling of Fibrous PEMFC Gas Diffusion Media Using Voronoi and Delaunay Tessellations, J. Electrochem. Soc. 160 (2013) F731–F743. doi:10.1149/2.009308jes.

[41] M. Aghighi, M.A. Hoeh, W. Lehnert, G. Merle, J. Gostick, Simulation of a Full Fuel Cell Membrane Electrode Assembly Using Pore Network Modeling, J. Electrochem. Soc. 163 (2016)

F384–F392. doi:10.1149/2.0701605jes.

[42] M.F. Lagadec, S. Müller, R. Zahn, V. Wood, Topological and Network Analysis of Lithium Ion Battery Components: The Importance of Separator Pore Space Connectivity for Battery Operation, Submitted. (2018).

[43] M. Sahimi, Flow phenomena in rocks: from continuum models to fractals, percolation, cellular automata, and simulated annealing, Rev. Mod. Phys. 65 (1993) 1393–1534. doi:10.1103/RevModPhys.65.1393.

[44] C. Zhang, J. Wang, A. Olah, E. Baer, Composite nanofibrous microfiltration water filter, J. Appl. Polym. Sci. 134 (2017) 1–12. doi:10.1002/app.45557.

[45] R. Krishna, Methodologies for screening and selection of crystalline microporous materials in mixture separations, Sep. Purif. Technol. 194 (2018) 281–300. doi:10.1016/j.seppur.2017.11.056.

[46] M.A. Sadeghi, M. Aghighi, J. Barralet, J.T. Gostick, Pore network modeling of reaction-diffusion in hierarchical porous particles: The effects of microstructure, Chem. Eng. J. 330 (2017) 1002–1011. doi:10.1016/j.cej.2017.07.139.

[47] Liang, Ioannidis, I. Chatzis, Geometric and Topological Analysis of Three-Dimensional Porous Media: Pore Space Partitioning Based on Morphological Skeletonization., J. Colloid Interface Sci. 221 (2000) 13–24. doi:10.1006/jcis.1999.6559.

[48] O.D. Velev, A.M. Lenhoff, Colloidal crystals as templates for porous materials, Curr. Opin. Colloid Interface Sci. 5 (2000) 56–63. doi:10.1016/S1359-0294(00)00039-X.

[49] S. Schlüter, A. Sheppard, K. Brown, D. Wildenschild, Image processing of multiphase images obtained via X-ray microtomography: A review, Water Resour. Res. 50 (2014) 3615–3639. doi:10.1002/2014WR015256.

[50] M. Sabharwal, L.M. Pant, A. Putz, D. Susac, J. Jankovic, M. Secanell, Analysis of Catalyst Layer

Microstructures: From Imaging to Performance, Fuel Cells. 16 (2016) 734–753. doi:10.1002/fuce.201600008.

[51] M.A. Ioannidis, I. Chatzis, On the geometry and topology of 3D stochastic porous media, J. Colloid Interface Sci. 229 (2000) 323–334. doi:10.1006/jcis.2000.7055.

[52] S. Torquato, B. Lu, Chord-length distribution function for two-phase random media, Phys. Rev. E. 47 (1993) 2950–2953. doi:10.1103/PhysRevE.47.2950.

[53] A.S. Al-Kharusi, M.J. Blunt, Network extraction from sandstone and carbonate pore space images, J. Pet. Sci. Eng. 56 (2007) 219–231.

[54] H. Dong, M.J. Blunt, Pore-network extraction from micro-computerized-tomography images., Phys. Rev. E. Stat. Nonlin. Soft Matter Phys. 80 (2009) 36307. doi:10.1103/PhysRevE.80.036307.

[55] W.B. Lindquist, S.-M. Lee, D.A. Coker, K.W. Jones, P. Spanne, Medial axis analysis of void structure in three-dimensional tomographic images of porous media, J. Geophys. Res. Solid Earth. 101 (1996) 8297–8310. doi:10.1029/95JB03039.

[56] H.J. Vogel, K. Roth, Quantitative morphology and network representation of soil pore structure, Adv. Water Resour. 24 (2001) 233–242. doi:10.1016/S0309-1708(00)00055-5.

[57] T. Agaesse, A. Lamibrac, F.N. Büchi, J. Pauchet, M. Prat, Validation of pore network simulations of ex-situ water distributions in a gas diffusion layer of proton exchange membrane fuel cells with X-ray tomographic images, J. Power Sources. 331 (2016) 462–474. doi:10.1016/j.jpowsour.2016.09.076.

[58] D. Wildenschild, A.P. Sheppard, X-ray imaging and analysis techniques for quantifying pore-scale structure and processes in subsurface porous medium systems, Adv. Water Resour. 51 (2013) 217–246. doi:10.1016/j.advwatres.2012.07.018.

[59] A.K. Datta, Porous media approaches to studying simultaneous heat and mass transfer in food

processes. I: Problem formulations, J. Food Eng. 80 (2007) 80–95. doi:10.1016/j.jfoodeng.2006.05.013.

[60] M.J. Blunt, Multiphase Flow in Permeable Media, Cambridge University Press, Cambridge, 2017. doi:10.1017/9781316145098.

[61] E. Jones, T. Oliphant, P. Peterson, Others, SciPy: Open source scientific tools for Python: available at https://www.scipy.org/, (2001). https://www.scipy.org/.

[62] J.. Gostick, PoreSpy: A set of tools for characterizing and analying 3D images of porous materials. https://github.com/PMEAL/porespy, (2018). https://github.com/PMEAL/porespy.

[63] S. van der Walt, J.L. Schönberger, J. Nunez-Iglesias, F. Boulogne, J.D. Warner, N. Yager, E. Gouillart, T. Yu, the scikit-image contributors, scikit-image: image processing in {P}ython, PeerJ. 2 (2014) e453. doi:10.7717/peerj.453.

[64] K.A. Culligan, D. Wildenschild, B.S.B. Christensen, W.G. Gray, M.L. Rivers, A.F.B. Tompson, Interfacial area measurements for unsaturated flow through a porous medium, Water Resour. Res. 40 (2004) 1–12. doi:10.1029/2004WR003278.

[65] T. Lewiner, H. Lopes, A.W. Vieira, G. Tavares, Efficient Implementation of Marching Cubes' Cases with Topological Guarantees, J. Graph. Tools. 8 (2003) 1–15. doi:10.1080/10867651.2003.10487582.

[66] V. Šmilauer, B. Chareyre, DEM formulation, in: Yade Doc. 2nd Ed, The {Y}ade Project, 2015. doi:10.5281/zenodo.34044.

[67] A. Bertei, B. Nucci, C. Nicolella, Effective transport properties in random packings of spheres and agglomerates, Chem. Eng. Trans. 32 (2013) 1531–1536. doi:10.33032/CET1332256.

[68] S. Chandrasekhar, Stochastic Problems in Physics and Astronomy, Rev. Mod. Phys. 15 (1943) 1–89. doi:10.1103/RevModPhys.15.1.

[69] T.G. Tranter, M.D.R. Kok, Lam., J.T. Gostick, pytrax: a simple and efficient random walk implementation for calculating the tortuosity tensor of images. https://github.com/PMEAL/pytrax, (2018).

[70] E.A. Codling, M.J. Plank, S. Benhamou, Random walk models in biology, J. R. Soc. Interface. 5 (2008) 813–834. doi:10.1098/rsif.2008.0014.

[71] C.N. Davies, Gas transport in porous media: The dusty-gas model, J. Aerosol Sci. 15 (1984) 81. doi:10.1016/0021-8502(84)90058-2.

[72] J.S. Agapiou, M.F. DeVries, An Experimental Determination of the Thermal Conductivity of a 304L Stainless Steel Powder Metallurgy Material, J. Heat Transfer. 111 (1989) 281–286. doi:10.1115/1.3250675.

[73] J.C.Y. Koh, A. Fortini, Thermal conductivity and electrical resistivity of porous material, (1971) 41. https://ntrs.nasa.gov/search.jsp?R=19720011984.

[74] J.A. Currie, Gaseous diffusion in porous media. Part 2. - Dry granular materials, Br. J. Appl. Phys. 11 (1960) 318. http://stacks.iop.org/0508-3443/11/i=8/a=303.

[75] S. Schlüter, A. Sheppard, K. Brown, D. Wildenschild, Image processing of multiphase images obtained via X-ray microtomography: A review, Water Resour. Res. 50 (2014) 3615–3639. doi:10.1002/2014WR015256.

[76] A. Kornilov, I. Safonov, An Overview of Watershed Algorithm Implementations in Open Source Libraries, J. Imaging. 4 (2018) 123. doi:10.3390/jimaging4100123.

[77] M. Li, J. Lu, Z. Chen, K. Amine, 30 Years of Lithium-Ion Batteries, Adv. Mater. 30 (2018) 1800561. doi:10.1002/adma.201800561.

[78] Y. Chan, J.J. Wylie, A continuum model of lithium ion transport inside graphene, EPL (Europhysics Lett. 123 (2018) 14002. doi:10.1209/0295-5075/123/14002.

[79] K. Yoo, S. Banerjee, J. Kim, P. Dutta, A Review of Lithium-Air Battery Modeling Studies, Energies. 10 (2017) 1748. doi:10.3390/en10111748.

[80] T. Hutzenlaub, S. Thiele, N. Paust, R. Spotnitz, R. Zengerle, C. Walchshofer, Three-dimensional electrochemical Li-ion battery modelling featuring a focused ion-beam/scanning electron microscopy based three-phase reconstruction of a LiCoO2 cathode, Electrochim. Acta. 115 (2014) 131–139. doi:10.1016/j.electacta.2013.10.103.

[81] D.E. Stephenson, B.C. Walker, C.B. Skelton, E.P. Gorzkowski, D.J. Rowenhorst, D.R. Wheeler, Modeling 3D Microstructure and Ion Transport in Porous Li-Ion Battery Electrodes, J. Electrochem. Soc. 158 (2011) A781. doi:10.1149/1.3579996.

[82] A.G. Kashkooli, A. Amirfazli, S. Farhad, D.U. Lee, S. Felicelli, H.W. Park, K. Feng, V. De Andrade, Z. Chen, Representative volume element model of lithium-ion battery electrodes based on X-ray nano-tomography, J. Appl. Electrochem. 47 (2017) 281–293. doi:10.1007/s10800-016-1037-y.

[83] C. Tan, T.M.M. Heenan, R.F. Ziesche, S.R. Daemi, J. Hack, M. Maier, S. Marathe, C. Rau, D.J.L. Brett, P.R. Shearing, Four-Dimensional Studies of Morphology Evolution in Lithium–Sulfur Batteries, ACS Appl. Energy Mater. 1 (2018) 5090–5100. doi:10.1021/acsaem.8b01148.

[84] Q. Meyer, N. Mansor, F. Iacoviello, P.L. Cullen, R. Jervis, D. Finegan, C. Tan, J. Bailey, P.R. Shearing, D.J.L. Brett, Investigation of Hot Pressed Polymer Electrolyte Fuel Cell Assemblies via X-ray Computed Tomography, Electrochim. Acta. 242 (2017) 125–136. doi:10.1016/j.electacta.2017.05.028.

[85] M. El Hannach, M. Prat, J. Pauchet, Pore network model of the cathode catalyst layer of proton exchange membrane fuel cells: Analysis of water management and electrical performance, Int. J. Hydrogen Energy. 37 (2012) 18996–19006. doi:10.1016/j.ijhydene.2012.09.139.

[86] M.A. Sadeghi, M. Aganou, M. Kok, M. Aghighi, G. Merle, J. Barralet, J. Gostick, Exploring the

Impact of Electrode Microstructure on Redox Flow Battery Performance Using a Multiphysics Pore Network Model, J. Electrochem. Soc. 166 (2019) A2121–A2130. doi:10.1149/2.0721910jes.

[87] A. Gayon Lombardo, B.A. Simon, O. Taiwo, S.J. Neethling, N.P. Brandon, A pore network model of porous electrodes in electrochemical devices, J. Energy Storage. 24 (2019) 100736. doi:10.1016/j.est.2019.04.010.

[88] P.A. García-Salaberri, I. V. Zenyuk, A.D. Shum, G. Hwang, M. Vera, A.Z. Weber, J.T. Gostick, Analysis of representative elementary volume and through-plane regional characteristics of carbon-fiber papers: diffusivity, permeability and electrical/thermal conductivity, Int. J. Heat Mass Transf. 127 (2018) 687–703. doi:10.1016/j.ijheatmasstransfer.2018.07.030.

[89] P.A. García-Salaberri, I. V. Zenyuk, G. Hwang, M. Vera, A.Z. Weber, J.T. Gostick, Implications of inherent inhomogeneities in thin carbon fiber-based gas diffusion layers: A comparative modeling study, Electrochim. Acta. 295 (2019) 861–874. doi:10.1016/j.electacta.2018.09.089.

[90] M.F. Lagadec, R. Zahn, S. Müller, V. Wood, Topological and network analysis of lithium ion battery components: the importance of pore space connectivity for cell operation, Energy Environ. Sci. 11 (2018) 3194–3200. doi:10.1039/C8EE00875B.

[91] A. Torayev, A. Rucci, P.C.M.M. Magusin, A. Demortière, V. De Andrade, C.P. Grey, C. Merlet, A.A. Franco, Stochasticity of Pores Interconnectivity in Li–O 2 Batteries and its Impact on the Variations in Electrochemical Performance, J. Phys. Chem. Lett. 9 (2018) 791–797. doi:10.1021/acs.jpclett.7b03315.

[92] A. Torayev, P.C.M.M. Magusin, C.P. Grey, C. Merlet, A.A. Franco, Importance of Incorporating Explicit 3D-Resolved Electrode Mesostructures in Li–O 2 Battery Models, ACS Appl. Energy Mater. 1 (2018) 6433–6441. doi:10.1021/acsaem.8b01392.

[93] S.R. Daemi, C. Tan, T. Volkenandt, S.J. Cooper, A. Palacios-Padros, J. Cookson, D.J.L. Brett, P.R. Shearing, Visualizing the Carbon Binder Phase of Battery Electrodes in Three Dimensions,

ACS Appl. Energy Mater. 1 (2018) 3702–3710. doi:10.1021/acsaem.8b00501.

[94] Z.A. Khan, T. Tranter, M. Agnaou, A. Elkamel, J. Gostick, Dual network extraction algorithm to investigate multiple transport processes in porous materials: Image-based modeling of pore and grain scale processes, Comput. Chem. Eng. 123 (2019) 64–77. doi:10.1016/j.compchemeng.2018.12.025.

[95] J. Gostick, Z. Khan, T. Tranter, M. Kok, M. Agnaou, M. Sadeghi, R. Jervis, PoreSpy: A Python Toolkit for Quantitative Analysis of Porous Media Images, J. Open Source Softw. 4 (2019) 1296. doi:10.21105/joss.01296.

[96] P. Soille, Morphological Image Analysis, Springer Berlin Heidelberg, Berlin, Heidelberg, 2004. doi:10.1007/978-3-662-05088-0.

[97] J.T. Gostick, Versatile and efficient pore network extraction method using marker-based watershed segmentation, Phys. Rev. E. 96 (2017) 023307. doi:10.1103/PhysRevE.96.023307.

[98] J. Gostick, M. Aghighi, J. Hinebaugh, T. Tranter, M.A. Hoeh, H. Day, B. Spellacy, M.H. Sharqawy, A. Bazylak, A. Burns, W. Lehnert, A. Putz, OpenPNM: A Pore Network Modeling Package, Comput. Sci. Eng. 18 (2016) 60–74. doi:10.1109/MCSE.2016.49.

[99] J. Landesfeind, H.A. Gasteiger, Temperature and Concentration Dependence of the Ionic Transport Properties of Lithium-Ion Battery Electrolytes, J. Electrochem. Soc. 166 (2019) A3079–A3097. doi:10.1149/2.0571912jes.

[100] A. Ehrl, J. Landesfeind, W.A. Wall, H.A. Gasteiger, Determination of transport parameters in liquid binary lithium ion battery electrolytes - I. Diffusion coefficient, J. Electrochem. Soc. 164 (2017) A826–A836. doi:10.1149/2.1131704jes.

[101] Y.-H. Chen, C.-W. Wang, G. Liu, X.-Y. Song, V.S. Battaglia, A.M. Sastry, Selection of Conductive Additives in Li-Ion Battery Cathodes, J. Electrochem. Soc. 154 (2007) A978. doi:10.1149/1.2767839.

[102] H.-J. Noh, S. Youn, C.S. Yoon, Y.-K. Sun, Comparison of the structural and electrochemical properties of layered Li[NixCoyMnz]O2 (x = 1/3, 0.5, 0.6, 0.7, 0.8 and 0.85) cathode material for lithium-ion batteries, J. Power Sources. 233 (2013) 121–130. doi:10.1016/j.jpowsour.2013.01.063.

[103] F.L.E. Usseglio-Viretta, A. Colclasure, A.N. Mistry, K.P.Y. Claver, F. Pouraghajan, D.P. Finegan, T.M.M. Heenan, D. Abraham, P.P. Mukherjee, D. Wheeler, P. Shearing, S.J. Cooper, K. Smith, Resolving the Discrepancy in Tortuosity Factor Estimation for Li-Ion Battery Electrodes through Micro-Macro Modeling and Experiment, J. Electrochem. Soc. 165 (2018) A3403–A3426. doi:10.1149/2.0731814jes.

[104] B.L. Trembacki, A.N. Mistry, D.R. Noble, M.E. Ferraro, P.P. Mukherjee, S.A. Roberts, Editors' Choice—Mesoscale Analysis of Conductive Binder Domain Morphology in Lithium-Ion Battery Electrodes, J. Electrochem. Soc. 165 (2018) E725–E736. doi:10.1149/2.0981813jes.

[105] L. Zielke, T. Hutzenlaub, D.R. Wheeler, C.-W. Chao, I. Manke, A. Hilger, N. Paust, R. Zengerle, S. Thiele, Three-Phase Multiscale Modeling of a LiCoO 2 Cathode: Combining the Advantages of FIB-SEM Imaging and X-Ray Tomography, Adv. Energy Mater. 5 (2015) 1401612. doi:10.1002/aenm.201401612.

[106] B. Tjaden, S.J. Cooper, D.J. Brett, D. Kramer, P.R. Shearing, On the origin and application of the Bruggeman correlation for analysing transport phenomena in electrochemical systems, Curr. Opin. Chem. Eng. 12 (2016) 44–51. doi:10.1016/j.coche.2016.02.006.

[107] A. Mistry, P.P. Mukherjee, Deconstructing electrode pore network to learn transport distortion, Phys. Fluids. 31 (2019) 122005. doi:10.1063/1.5124099.

[108] J.E. Santos, D. Xu, H. Jo, C.J. Landry, M. Prodanović, M.J. Pyrcz, PoreFlow-Net: A 3D convolutional neural network to predict fluid flow through porous media, Adv. Water Resour. 138 (2020) 103539. doi:10.1016/j.advwatres.2020.103539.

[109] A. Parvan, S. Jafari, M. Rahnama, S. Norouzi apourvari, A. Raoof, Insight into particle retention

and clogging in porous media; a pore scale study using lattice Boltzmann method, Adv. Water Resour. 138 (2020) 103530. doi:https://doi.org/10.1016/j.advwatres.2020.103530.

[110] Q. Sheng, K. Thompson, A unified pore-network algorithm for dynamic two-phase flow, Adv. Water Resour. 95 (2016) 92–108. doi:10.1016/j.advwatres.2015.12.010.

[111] K.M. Gerke, T.O. Sizonenko, M. V Karsanina, E. V Lavrukhin, V. V Abashkin, D. V Korost, Improving watershed-based pore-network extraction method using maximum inscribed ball pore-body positioning, Adv. Water Resour. (2020) 103576. doi:10.1016/j.advwatres.2020.103576.

[112] S.J. Jackson, Q. Lin, S. Krevor, Representative elementary volumes, hysteresis and heterogeneity in multiphase flow from the pore to continuum scale, Water Resour. Res. (2020) e2019WR026396. doi:10.1029/2019WR026396.

[113] Y. Da Wang, T. Chung, R.T. Armstrong, J.E. McClure, P. Mostaghimi, Computations of permeability of large rock images by dual grid domain decomposition, Adv. Water Resour. 126 (2019) 1–14. doi:10.1016/j.advwatres.2019.02.002.

[114] C. Soulaine, F. Gjetvaj, C. Garing, S. Roman, A. Russian, P. Gouze, H.A. Tchelepi, The Impact of Sub-Resolution Porosity of X-ray Microtomography Images on the Permeability, Transp. Porous Media. 113 (2016) 227–243. doi:10.1007/s11242-016-0690-2.

[115] R. Song, Y. Wang, J. Liu, M. Cui, Y. Lei, Comparative analysis on pore-scale permeability prediction on micro-CT images of rock using numerical and empirical approaches, Energy Sci. Eng. 7 (2019) 2842–2854. doi:10.1002/ese3.465.

[116] Z.A. Khan, P.A.G. Salaberri, T.M.M. Heenan, R. Jervis, P.R. Shearing, D. Brett, A. Elkamel, J.T. Gostick, Probing the Structure-Performance Relationship of Lithium-Ion Battery Cathodes Using Pore-Networks Extracted from Three-Phase Tomograms, J. Electrochem. Soc. 167 (2020) 040528. doi:10.1149/1945-7111/ab7bd8.

[117] P.-R. Thomson, A. Aituar-Zhakupova, S. Hier-Majumder, Image Segmentation and Analysis of

Pore Network Geometry in Two Natural Sandstones , Front. Earth Sci. . 6 (2018) 58. https://www.frontiersin.org/article/10.3389/feart.2018.00058.

[118] A. Torayev, A. Rucci, P.C.M.M. Magusin, A. Demortière, V. De Andrade, C.P. Grey, C. Merlet, A.A. Franco, Stochasticity of Pores Interconnectivity in Li–O 2 Batteries and its Impact on the Variations in Electrochemical Performance, J. Phys. Chem. Lett. 9 (2018) 791–797. doi:10.1021/acs.jpclett.7b03315.

[119] H. Dong, S. Fjeldstad, S. Roth, S. Bakke, P. Øren, Pore Network Modelling on Carbonate: A comparative Study of Different Micro-CT Network Extraction Methods, in: Proc. Int. Symp. Soc. Core Anal., 2008: pp. 2008–2031.

[120] F. Arand, J. Hesser, Accurate and efficient maximal ball algorithm for pore network extraction, Comput. Geosci. 101 (2017) 28–37. doi:10.1016/j.cageo.2017.01.004.

[121] R.I. Al-Raoush, C.S. Willson, Extraction of physically realistic pore network properties from three-dimensional synchrotron X-ray microtomography images of unconsolidated porous media systems, J. Hydrol. 300 (2005) 44–64. doi:10.1016/J.JHYDROL.2004.05.005.

[122] S. Bakke, P.-E. Øren, 3-D Pore-Scale Modelling of Sandstones and Flow Simulations in the Pore Networks, SPE J. 2 (1997) 136–149. doi:10.2118/35479-PA.

[123] A. Sheppard, R. Sok, H. Averdunk, Improved Pore Network Extraction Methods, Int. Symp. Soc. Core Anal. (2005).

[124] K.M. Gerke, T.O. Sizonenko, M. V. Karsanina, E. V. Lavrukhin, V. V. Abashkin, D. V. Korost, Improving watershed-based pore-network extraction method using maximum inscribed ball pore-body positioning, Adv. Water Resour. 140 (2020) 103576. doi:10.1016/j.advwatres.2020.103576.

[125] X. Miao, K.M. Gerke, T.O. Sizonenko, A new way to parameterize hydraulic conductances of pore elements: A step towards creating pore-networks without pore shape simplifications, Adv. Water Resour. 105 (2017) 162–172. doi:10.1016/j.advwatres.2017.04.021.

[126] A. Rabbani, P. Mostaghimi, R.T. Armstrong, Pore network extraction using geometrical domain decomposition, Adv. Water Resour. 123 (2019) 70–83. doi:10.1016/j.advwatres.2018.11.003.

[127] A.H. Kohanpur, A.J. Valocchi, Pore-network stitching method: A pore-to-core upscaling approach for multiphase flow, ArXiv:2004.01523. (2020). http://arxiv.org/abs/2004.01523 (accessed May 17, 2020).

[128] A.N. Moga, M. Gabbouj, Parallel Marker-Based Image Segmentation with Watershed Transformation, J. Parallel Distrib. Comput. 51 (1998) 27–45. doi:10.1006/jpdc.1998.1448.

[129] A. N. Moga, B. Cramariuc, M. Gabbouj, Parallel watershed transformation algorithms for image segmentation, Parallel Comput. 24 (1998) 1981–2001. doi:10.1016/S0167-8191(98)00085-4.

[130] R. Romero-Zaliz, J.. Reinoso-Gordo, Soft Computing for Sustainability Science, Springer International Publishing, Cham, 2018. doi:10.1007/978-3-319-62359-7.

[131] J.B.T.M. Roerdink, A. Meijster, The Watershed Transform: Definitions, Algorithms and Parallelization Strategies, Fundam. Informaticae. 41 (2000) 187–228. doi:10.3233/FI-2000-411207.

[132] A.N. Moga, M. Gabbouj, Parallel Marker-Based Image Segmentation with Watershed Transformation, J. Parallel Distrib. Comput. 51 (1998) 27–45. doi:10.1006/jpdc.1998.1448.

[133] B. Wagner, A. Dinges, P. Müller, G. Haase, Parallel Volume Image Segmentation with Watershed Transformation BT - Image Analysis, in: A.-B. Salberg, J.Y. Hardeberg, R. Jenssen (Eds.), Springer Berlin Heidelberg, Berlin, Heidelberg, 2009: pp. 420–429.

[134] C. Nicolescu, B. Albers, P. Jonker, Parallel watershed algorithm on images from cranial CT-scans using PVM and MPI on a distributed memory system, in: Lect. Notes Comput. Sci. (Including Subser. Lect. Notes Artif. Intell. Lect. Notes Bioinformatics), 1999: pp. 418–425. doi:10.1007/3-540-48158-3_52.

[135] L. Vincent, P. Soille, Watersheds in digital spaces: an efficient algorithm based on immersion simulations, IEEE Trans. Pattern Anal. Mach. Intell. 13 (1991) 583–598. doi:10.1109/34.87344.

[136] F. Meyer, S. Beucher, Morphological segmentation, J. Vis. Commun. Image Represent. 1 (1990) 21–46. doi:10.1016/1047-3203(90)90014-M.

[137] S. Beucher, Watershed, Hierarchical Segmentation and Waterfall Algorithm, in: J. Serra, P. Soille (Eds.), Math. Morphol. Its Appl. to Image Process., Springer Netherlands, Dordrecht, 1994: pp. 69–76. doi:10.1007/978-94-011-1040-2_10.

[138] P. Virtanen, R. Gommers, T.E. Oliphant, M. Haberland, T. Reddy, D. Cournapeau, E. Burovski, P. Peterson, W. Weckesser, J. Bright, S.J. van der Walt, M. Brett, J. Wilson, K.J. Millman, N. Mayorov, A.R.J. Nelson, E. Jones, R. Kern, E. Larson, C.J. Carey, İ. Polat, Y. Feng, E.W. Moore, J. VanderPlas, D. Laxalde, J. Perktold, R. Cimrman, I. Henriksen, E.A. Quintero, C.R. Harris, A.M. Archibald, A.H. Ribeiro, F. Pedregosa, P. van Mulbregt, SciPy 1.0: fundamental algorithms for scientific computing in Python, Nat. Methods. 17 (2020) 261–272. doi:10.1038/s41592-019-0686-2.

[139] M. Rocklin, Dask: Parallel Computation with Blocked algorithms and Task Scheduling, in: Proc. 14th Python Sci. Conf., 2015: pp. 126–132. doi:10.25080/Majora-7b98e3ed-013.

[140] S.K. Lam, A. Pitrou, S. Seibert, Numba, in: Proc. Second Work. LLVM Compil. Infrastruct. HPC - LLVM ’15, ACM Press, New York, New York, USA, 2015: pp. 1–6. doi:10.1145/2833157.2833162.

[141] H. Dong, M.J. Blunt, Pore-network extraction from micro-computerized-tomography images, Phys. Rev. E. 80 (2009) 36307. https://link.aps.org/doi/10.1103/PhysRevE.80.036307.

[142] H. Dong, Micro-Ct Imaging and Pore Network Extraction, PhD thesis, 2007.

[143] R. Hilfer, T. Zauner, High-precision synthetic computed tomography of reconstructed porous media, Phys. Rev. E. 84 (2011) 062301. doi:10.1103/PhysRevE.84.062301.

[144] J. Samuel, L. Qingyang, K. Samuel, A large scale X-Ray micro-tomography dataset of steady-state multiphase flow, Digit. Rocks Portal. (2019). doi:10.17612/KT0B-SZ28.

[145] Z.A. Khan, T. Tranter, M. Agnaou, A. Elkamel, J. Gostick, Dual network extraction algorithm to investigate multiple transport processes in porous materials: Image-based modeling of pore and grain scale processes, Comput. Chem. Eng. 123 (2019) 64–77. doi:10.1016/J.COMPCHEMENG.2018.12.025.

[146] C. Pan, J.F. Prins, C.T. Miller, A high-performance lattice Boltzmann implementation to model flow in porous media, Comput. Phys. Commun. 158 (2004) 89–105. doi:10.1016/j.cpc.2003.12.003.

[147] H. Liu, Q. Kang, C.R. Leonardi, S. Schmieschek, A. Narváez, B.D. Jones, J.R. Williams, A.J. Valocchi, J. Harting, Multiphase lattice Boltzmann simulations for porous media applications, Comput. Geosci. 20 (2016) 777–805. doi:10.1007/s10596-015-9542-3.

[148] T.G. Tranter, M.D.R. Kok, M. Lam, J.T. Gostick, pytrax: A simple and efficient random walk implementation for calculating the directional tortuosity of images, SoftwareX. 10 (2019) 100277. doi:10.1016/J.SOFTX.2019.100277.

[149] E.A. Codling, M.J. Plank, S. Benhamou, Random walk models in biology, J. R. Soc. Interface. 5 (2008) 813–834. doi:10.1098/rsif.2008.0014.

[150] C.N. Davies, Gas transport in porous media: The dusty-gas model, J. Aerosol Sci. 15 (1984) 81. doi:10.1016/0021-8502(84)90058-2.

[151] Y. Kim, J.T. Gostick, Measuring effective diffusivity in porous media with a gasket-free, radial arrangement, Int. J. Heat Mass Transf. 129 (2019) 1023–1030. doi:10.1016/j.ijheatmasstransfer.2018.10.054.

[152] T.P. de Carvalho, H.P. Morvan, D.M. Hargreaves, H. Oun, A. Kennedy, Pore-Scale Numerical Investigation of Pressure Drop Behaviour Across Open-Cell Metal Foams, Transp. Porous Media.

117 (2017) 311–336. doi:10.1007/s11242-017-0835-y.

[153] G. Sundaramoorthi, M. Hadwiger, M. Ben-Romdhane, A.R. Behzad, P. Madhavan, S.P. Nunes, 3D Membrane Imaging and Porosity Visualization, Ind. Eng. Chem. Res. 55 (2016) 3689–3695. doi:10.1021/acs.iecr.6b00387.

[154] P.R. Thomson, A. Hazel, S. Hier-Majumder, The influence of microporous cements on the pore network geometry of natural sedimentary rocks, Front. Earth Sci. 7 (2019) 1–14. doi:10.3389/feart.2019.00048.

[155] B.P. Muljadi, M.J. Blunt, A.Q. Raeini, B. Bijeljic, The impact of porous media heterogeneity on non-Darcy flow behaviour from pore-scale simulation, Adv. Water Resour. 95 (2016) 329–340. doi:10.1016/j.advwatres.2015.05.019.

[156] J.T. Fredrich, K.H. Greaves, J.W. Martin, Pore geometry and transport properties of Fontainebleau sandstone, Int. J. Rock Mech. Min. Sci. Geomech. Abstr. 30 (1993) 691–697. doi:10.1016/0148-9062(93)90007-Z.

[157] M. V. Karsanina, K.M. Gerke, E.B. Skvortsova, A.L. Ivanov, D. Mallants, Enhancing image resolution of soils by stochastic multiscale image fusion, Geoderma. 314 (2018) 138–145. doi:10.1016/j.geoderma.2017.10.055.

[158] M. V. Karsanina, K.M. Gerke, Hierarchical Optimization: Fast and Robust Multiscale Stochastic Reconstructions with Rescaled Correlation Functions, Phys. Rev. Lett. 121 (2018) 265501. doi:10.1103/PhysRevLett.121.265501.

[159] S.M. Shah, F. Gray, J.P. Crawshaw, E.S. Boek, Micro-computed tomography pore-scale study of flow in porous media: Effect of voxel resolution, Adv. Water Resour. 95 (2016) 276–287. doi:10.1016/j.advwatres.2015.07.012.

[160] N. Nitta, F. Wu, J.T. Lee, G. Yushin, Li-ion battery materials: Present and future, Mater. Today. 18 (2015) 252–264. doi:10.1016/j.mattod.2014.10.040.

[161] A. Guler, H. Gungor, S. Ozcan, A. Coban, M.O. Guler, H. Akbulut, A high-performance composite positive electrode based on graphene and Li (Ni1/3Co1/3Mn1/3)O2, Int. J. Energy Res. 42 (2018) 4499–4511. doi:10.1002/er.4198.

[162] W.D. Toh, B. Xu, J. Jia, C.S. Chin, J. Chiew, Z. Gao, Lithium Iron Phosphate (LiFePO4) Battery Power System for Deepwater Emergency Operation, Energy Procedia. 143 (2017) 348–353. doi:10.1016/j.egypro.2017.12.695.

[163] S.J. Cooper, D.S. Eastwood, J. Gelb, G. Damblanc, D.J.L. Brett, R.S. Bradley, P.J. Withers, P.D. Lee, A.J. Marquis, N.P. Brandon, P.R. Shearing, Image based modelling of microstructural heterogeneity in LiFePO 4 electrodes for Li-ion batteries, J. Power Sources. 247 (2014) 1033–1039. doi:10.1016/j.jpowsour.2013.04.156.

[164] C.-F. Chen, A. Verma, P.P. Mukherjee, Probing the Role of Electrode Microstructure in the Lithium-Ion Battery Thermal Behavior, J. Electrochem. Soc. 164 (2017) E3146–E3158. doi:10.1149/2.0161711jes.

[165] Z.A. Khan, J.T. Gostick, On the Importance of Incorporating Structural Heterogeneity of Porous Electrodes in LI-ION Battery Models: Pore Network Modelling a Way to MOVE Forward, ECS Meet. Abstr. MA2020-01 (2020) 322. doi:10.1149/ma2020-012322mtgabs.

[166] M. Farkhondeh, M. Safari, M. Pritzker, M. Fowler, T. Han, J. Wang, C. Delacourt, Full-Range Simulation of a Commercial LiFePO 4 Electrode Accounting for Bulk and Surface Effects: A Comparative Analysis , J. Electrochem. Soc. 161 (2014) A201–A212. doi:10.1149/2.094401jes.

[167] M. Doyle, J. Newman, The use of mathematical modeling in the design of lithium/polymer battery systems, Electrochim. Acta. 40 (1995) 2191–2196. doi:10.1016/0013-4686(95)00162-8.

[168] T.S. Chadha, B. Suthar, D. Rife, V.R. Subramanian, P. Biswas, Model Based Analysis of One-Dimensional Oriented Lithium-Ion Battery Electrodes, J. Electrochem. Soc. 164 (2017) E3114–E3121. doi:10.1149/2.0141711jes.

[169] A.G. Kashkooli, S. Farhad, D.U. Lee, K. Feng, S. Litster, S.K. Babu, L. Zhu, Z. Chen, Multiscale modeling of lithium-ion battery electrodes based on nano-scale X-ray computed tomography, J. Power Sources. 307 (2016) 496–509. doi:10.1016/j.jpowsour.2015.12.134.

[170] T.F. Fuller, M. Doyle, J. Newman, Simulation and Optimization of the Dual Lithium Ion Insertion Cell, J. Electrochem. Soc. 141 (1994) 1–10. doi:10.1149/1.2054684.

[171] L. Xia, E. Najafi, Z. Li, H.J. Bergveld, M.C.F. Donkers, A computationally efficient implementation of a full and reduced-order electrochemistry-based model for Li-ion batteries, Appl. Energy. 208 (2017) 1285–1296. doi:10.1016/j.apenergy.2017.09.025.

[172] Z.A. Khan, A. Elkamel, J.T. Gostick, Efficient extraction of pore networks from massive tomograms via geometric domain decomposition, Adv. Water Resour. 145 (2020) 103734. doi:10.1016/j.advwatres.2020.103734.

[173] M. Aghighi, J. Gostick, Pore network modeling of phase change in PEM fuel cell fibrous cathode, J. Appl. Electrochem. 47 (2017) 1323–1338. doi:10.1007/s10800-017-1126-6.

[174] H. Dong, M.J. Blunt, Pore-network extraction from micro-computerized-tomography images, Phys. Rev. E. 80 (2009) 036307. doi:10.1103/PhysRevE.80.036307.

[175] Y. Liang, P. Hu, S. Wang, S. Song, S. Jiang, Medial axis extraction algorithm specializing in porous media, Powder Technol. 343 (2019) 512–520. doi:10.1016/j.powtec.2018.11.061.

[176] M.F. Lagadec, R. Zahn, S. Müller, V. Wood, Topological and network analysis of lithium ion battery components: The importance of pore space connectivity for cell operation, Energy Environ. Sci. 11 (2018) 3194–3200. doi:10.1039/c8ee00875b.

[177] M. Chouchane, A. Rucci, T. Lombardo, A.C. Ngandjong, A.A. Franco, Lithium ion battery electrodes predicted from manufacturing simulations: Assessing the impact of the carbon-binder spatial location on the electrochemical performance, J. Power Sources. 444 (2019) 227285. doi:10.1016/j.jpowsour.2019.227285.

[178] Z.A. Khan, T. Tranter, M. Agnaou, A. Elkamel, J. Gostick, Dual network extraction algorithm to investigate multiple transport processes in porous materials: Image-based modeling of pore and grain scale processes, Comput. Chem. Eng. 123 (2019) 64–77. doi:10.1016/j.compchemeng.2018.12.025.

[179] P. Soille, Morphological Image Analysis, Springer Berlin Heidelberg, Berlin, Heidelberg, 2004. doi:10.1007/978-3-662-05088-0.

[180] L. Zielke, T. Hutzenlaub, D.R. Wheeler, I. Manke, T. Arlt, N. Paust, R. Zengerle, S. Thiele, A combination of X-ray tomography and carbon binder modeling: Reconstructing the three phases of LiCoO2 Li-ion battery cathodes, Adv. Energy Mater. 4 (2014) 1–6. doi:10.1002/aenm.201301617.

[181] W. Bauer, D. Nötzel, V. Wenzel, H. Nirschl, Influence of dry mixing and distribution of conductive additives in cathodes for lithium ion batteries, J. Power Sources. 288 (2015) 359–367. doi:10.1016/j.jpowsour.2015.04.081.

[182] H. Bockholt, W. Haselrieder, A. Kwade, Intensive powder mixing for dry dispersing of carbon black and its relevance for lithium-ion battery cathodes, Powder Technol. 297 (2016) 266–274. doi:10.1016/j.powtec.2016.04.011.

[183] S. Hein, T. Danner, D. Westhoff, B. Prifling, R. Scurtu, L. Kremer, A. Hoffmann, A. Hilger, M. Osenberg, I. Manke, M. Wohlfahrt-Mehrens, V. Schmidt, A. Latz, Influence of Conductive Additives and Binder on the Impedance of Lithium-Ion Battery Electrodes: Effect of Morphology, J. Electrochem. Soc. 167 (2020) 013546. doi:10.1149/1945-7111/ab6b1d.

[184] F.L.E. Usseglio-Viretta, K. Smith, Quantitative Microstructure Characterization of a NMC Electrode, ECS Trans. 77 (2017) 1095–1118. doi:10.1149/07711.1095ecst.

[185] A. Verma, K. Smith, S. Santhanagopalan, D. Abraham, K.P. Yao, P.P. Mukherjee, Galvanostatic Intermittent Titration and Performance Based Analysis of LiNi 0.5 Co 0.2 Mn 0.3 O 2 Cathode , J. Electrochem. Soc. 164 (2017) A3380–A3392. doi:10.1149/2.1701713jes.

[186] A. Shodiev, E.N. Primo, M. Chouchane, T. Lombardo, A.C. Ngandjong, A. Rucci, A.A. Franco, 4D-resolved physical model for Electrochemical Impedance Spectroscopy of Li(Ni1-x-yMnxCoy)O2-based cathodes in symmetric cells: Consequences in tortuosity calculations, J. Power Sources. 454 (2020) 227871. doi:10.1016/j.jpowsour.2020.227871.

[187] L.O. Valo/en, J.N. Reimers, Transport Properties of LiPF[sub 6]-Based Li-Ion Battery Electrolytes, J. Electrochem. Soc. 152 (2005) A882. doi:10.1149/1.1872737.

[188] Y. Norzihani, S.A. Hashim Ali, A.K. Arof, Transportation in a lithium-ion half-cell, Ionics (Kiel). 17 (2011) 715–719. doi:10.1007/s11581-011-0567-x.

[189] S.A. Hashim Ali, A.K. Arof, Modeling of discharge behavior of a lithium ion cell, J. Alloys Compd. 449 (2008) 292–295. doi:10.1016/j.jallcom.2005.12.135.

[190] W. Mei, H. Chen, J. Sun, Q. Wang, The effect of electrode design parameters on battery performance and optimization of electrode thickness based on the electrochemical-thermal coupling model, Sustain. Energy Fuels. 3 (2019) 148–165. doi:10.1039/c8se00503f.

[191] I. Cruz-Matías, D. Ayala, D. Hiller, S. Gutsch, M. Zacharias, S. Estradé, F. Peiró, Sphericity and roundness computation for particles using the extreme vertices model, J. Comput. Sci. 30 (2019) 28–40. doi:10.1016/j.jocs.2018.11.005.

[192] A. Rucci, A.C. Ngandjong, E.N. Primo, M. Maiza, A.A. Franco, Tracking variabilities in the simulation of Lithium Ion Battery electrode fabrication and its impact on electrochemical performance, Electrochim. Acta. 312 (2019) 168–178. doi:10.1016/j.electacta.2019.04.110.

[193] A. Meijster, J.B.T.M. Roerdink, W.H. Hesselink, A General Algorithm for Computing Distance Transforms in Linear Time BT - Mathematical Morphology and its Applications to Image and Signal Processing, in: J. Goutsias, L. Vincent, D.S. Bloomberg (Eds.), Springer US, Boston, MA, 2000: pp. 331–340. doi:10.1007/0-306-47025-X_36.

[194] P.F. Felzenszwalb, D.P. Huttenlocher, Distance Transforms of Sampled Functions, Theory

Comput. 8 (2012) 415–428. doi:10.4086/toc.2012.v008a019.

Appendix A: Supplementary Information for Chapter 4

The following Table S4- 1 provides a list information on the material properties as quoted by the supplier.

Table S4- 1 Supplier's information on the printed and calendared NMC811 electrode on a sheet of aluminum.

Material Property	Supplier Information
Al foil thickness	20 µm
Al foil loading	5.36 mg cm^{-2}
Total electrode thickness	52 µm
Coating thickens	32 µm
Porosity	36.3%
Coating loading	8.34 mg cm^{-2}
Coating Density	2.61 g cm^{-3}

Figure S4- 1 displays a single tomogram ortho slice that was extracted in the x-z plane whereby, z and x are the vertical and in-beam planes, respectively. Also noted on the image are the three components of the sample preparation: the steel dowel, fast-set epoxy and the NMC811 sample, the region of air above the sample is also noted for reference.

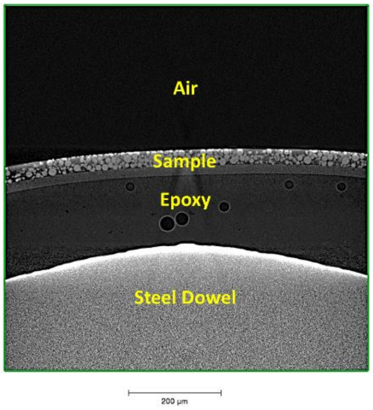

Figure S4- 1 Reconstructed tomogram slice taken from the x - z (in-beam - vertical) orientation. This image is presented before any image processing was conducted i.e. without post-reconstruction filtering or segmentation.

The following Figure S4- 2 displays the cross-section of the data before and after a non-locals means filter was applied. Two regions are outlined: one large area of the full field of view (FOV) and a magnified region for closer inspection. Throughout, imaged contoured by orange are filtered, and imaged that have not been filtered are contoured by green. The orange region in the large image also outlines the cropped region that was used for the segmentation and subsequent pore-network modeling.

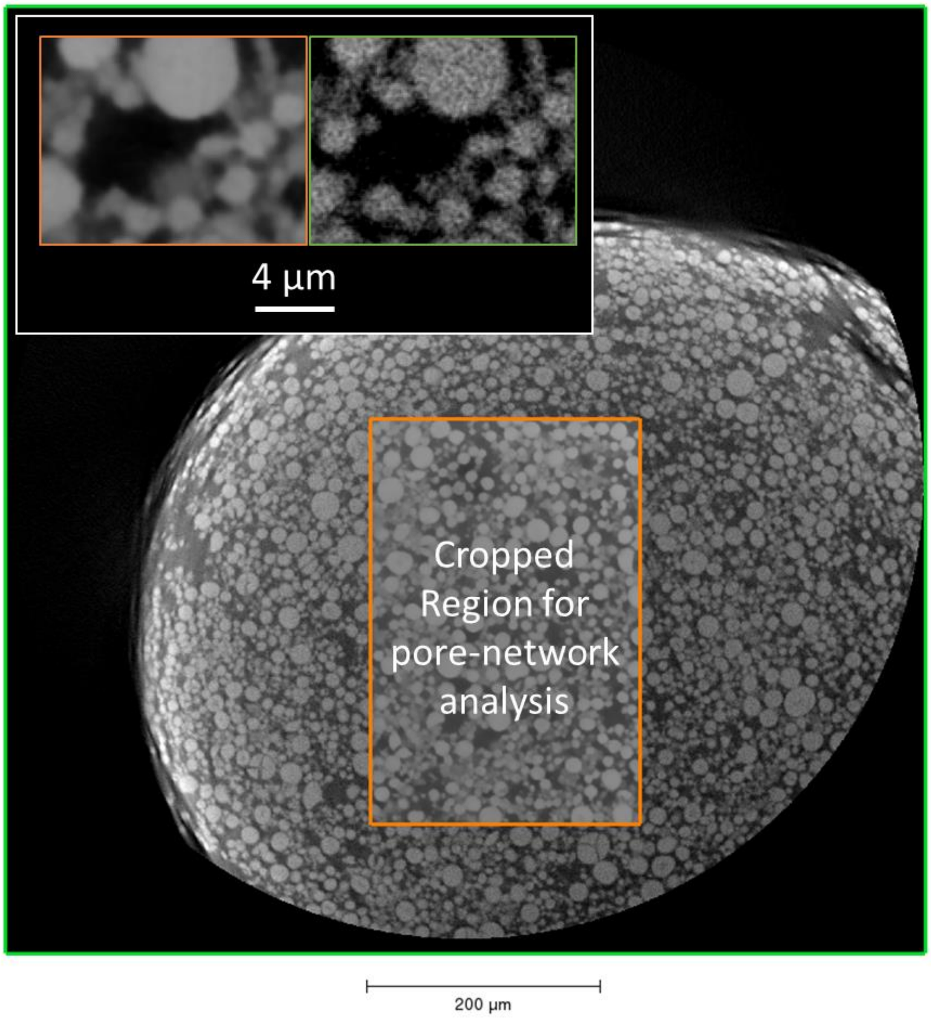

Figure S4- 2 Reconstructed tomogram slice before and after a non-local mean filter was applied to the raw, reconstructed data. Two regions are outlined: one large area of the full field of view (FOV) and a magnified region for closer inspection. Throughout, imaged contoured by orange are filtered, and imaged that have not been filtered are contoured by green. Also outlined is the cropped region for data analysis.

The following Figure S4- 3 displays a filtered region of the electrode for segmentation analysis. Accompanying the 2D greyscale images is the greyscale histogram with the greyscale values that correspond to each of the constituent phases outlined for clarity.

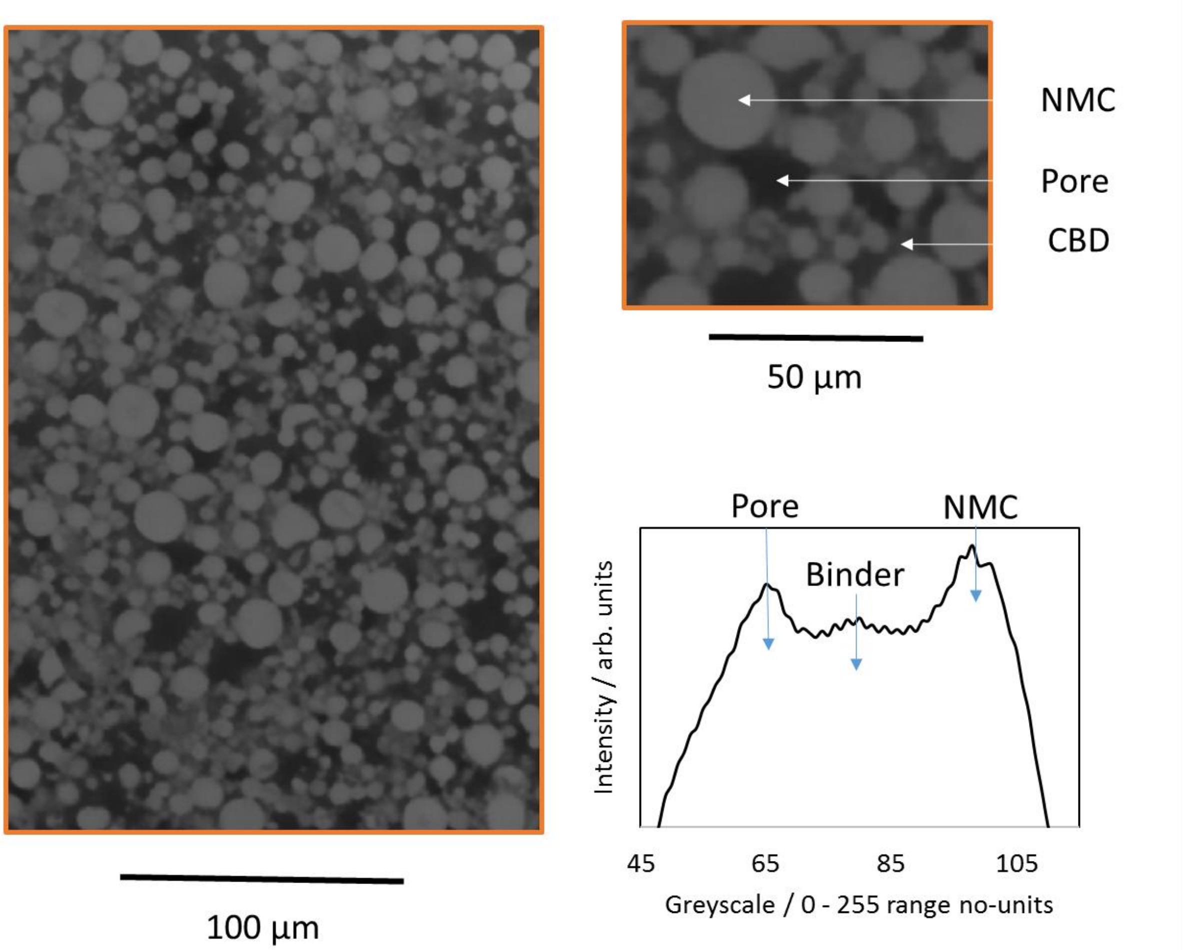

Figure S4- 3 Segmentation quality outlined through the indication of each constituent phase: NMC, binder, pore, visualized using 2D greyscale (filtered) ortho slices and the accompanying greyscale histogram.

The Table S4- 2 below lists the compositional values for the three segmented phases: NMC, binder and pore. The data was calculated from the segmented 3D dataset using the sum of all values corresponding to a particular phase within the volume, divided by the total volume and presented as a percentage; i.e. the composition was calculated from cubic voxels without accounting for surface smoothness.

Table S4- 2 Compositional data obtained from the 3D X-ray CT tomogram of the printed and calendared NMC811 electrode on a sheet of aluminum.

Phase	Calculated Composition / Vol. %
Pore	38.6%
CBD	21.9%
NMC	39.6%